Charmed baryon interaction from lattice QCD and its application to charmed hypernuclei

Takaya Miyamoto

Yukawa Institute for Theoretical Physics, Kyoto University

February 5, 2019

A Dissertation for the degree of Doctor of Philosophy

Abstract

In this thesis, we introduce our works on charmed baryon interactions from lattice QCD simulation. Additionally, we also present recent developments of numerical algorithms for the partial wave decomposition on the lattice.

In order to calculate the interaction on the lattice, we employ the HAL QCD method for the charmed baryon system. For the partial wave decomposition on the lattice, we employ Misner's method. By combining the HAL QCD method and Misner's method, we study the interaction in three charmed baryon systems: $\Lambda_c N$ system, $\Lambda_c N$-$\Sigma_c N$ coupled channel system and $\Lambda_c\Lambda_c$-$\Xi_{cc} N$ coupled channel system.

We first introduce results for the application of Misner's method to the HAL QCD method. We show some improvements of the numerical data for the potential on the lattice.

In the analysis of the $\Lambda_c N$ system, we find that the interaction is weakly attractive and spin-independent. While we observe no $\Lambda_c N$ bound state, our results indicate a possibility to form Λ_c hypernuclei. From the obtained $\Lambda_c N$ system, therefore, we construct effective potential between Λ_c and a nucleus, and find that Λ_c hypernuclei can exist for light or medium-heavy nuclei.

We then extend our consideration to the $\Lambda_c N$-$\Sigma_c N$ coupled channel. For the coupled channel potentials, we utilize the HAL QCD method expanded to the inelastic scattering. From the obtained potentials, we discuss the inelastic effects in the $\Lambda_c N$ system.

We also investigate the $\Lambda_c\Lambda_c$-$\Xi_{cc} N$ coupled channel system. We find that the attraction in the $\Xi_{cc} N$ is sufficiently strong to form a resonance state in the $\Lambda_c\Lambda_c$ scattering.

Contents

Chapter 1

Introduction

A study of baryon-baryon interactions is one of the most important subjects to investigate the properties of hadronic matters because the baryon-baryon interactions are utilized as a basic input in nuclear physics. For example, the low-energy nucleon-nucleon (NN) interaction, which has been severely constrained by the NN scattering data and the properties of finite nuclei [1], has been applied extensively to investigations of yet unknown hadronic matters such as neutron-rich nuclei. Together with the NN interaction, the hyperon-nucleon (YN) and the hyperon-hyperon (YY) interactions constructed phenomenologically to reproduce the properties of hypernuclei and hyperon-nucleon scattering data [2] have also been employed to investigate unknown hypernuclei and also the neutron star interiors.

As an extension, the charmed baryon interactions have been investigated to study possible charmed hypernuclei [3] just after the discovery of the Λ_c baryon. At that time, the one-boson-exchange potential (OBEP) model for the Y_cN ($Y_c = \Lambda_c, \Sigma_c$) was constructed [4], where the couplings are determined by assuming the flavor $SU(4)$ symmetry, which is an extension of the flavor $SU(3)$ symmetry for the YN interaction. The study was motivated by the fact that the kinetic energy is suppressed due to the heavy charmed baryon mass so that the charmed hypernuclei are likely to form bound states. In fact, based on flavor $SU(4)$ symmetry, Refs. [5, 6, 7] show the number of bound states in Λ_c hypernuclei is larger than that in Λ hypernuclei due to heavy Λ_c mass although the depth of the effective potential for Λ_c in the G-matrix calculation is about 2/3 of that for Λ.

However, the charm quark is much heavier than other three quarks (up, down, strange), so that the flavor $SU(4)$ symmetry may not give a good description of the Y_cN interaction.

In recent works, the charmed baryon interaction has been investigated more widely by relatively new models, such as the OBEP model based on the heavy quark effective theory [8], the constituent quark model [9, 10, 11] and the quark-meson coupling model [12, 13]. One can find that, however, some of the results shown in these works are contradictory although they are consistent in the NN interactions. In particular, as discussed in Ref. [14], it is suggested that the $\Lambda_c N$ two-body system forms bound states in Refs. [8, 11] with relatively large binding energies, while there is no such a binding solution in Ref. [14]. Since there are no experimental data in any charmed baryon scattering and charmed hypernuclei so far, the charmed baryon interaction is still inconclusive.

Under these circumstances, in order to shed new light on the problem, we investigate the charmed baryon interaction from first-principle lattice QCD simulations. The lattice QCD simulation is a powerful tool to calculate low-energy quantities in QCD non-perturbatively, which has been successfully applied to the single-hadron masses [15, 16, 17]. The most advantageous point in the lattice QCD simulation is that it requires no phenomenological parameters so that the applications to the charmed systems are straightforward. In fact, several charmed baryon masses have been investigated from lattice QCD simulation in Ref. [18], in which the results are consistent with experimental values. Furthermore, the authors have predicted masses of doubly charmed baryons which have not been measured experimentally in those days. A remarkable point here is that a doubly charmed baryon Ξ_{cc}^{++} has been actually found in recent experiment in LHCb [19] with the mass $m_{\Xi_{cc}^{++}} \simeq 3621$ MeV, which is consistent to the numerical results in Ref. [18].

There have been proposed two methods to analyze the hadron-hadron interactions on the lattice, Lüscher's finite volume method [20] and the HAL QCD method [21]. By Lüscher's finite volume method, we obtain phase shifts in the infinite space from effective energies for the hadron-hadron system in a cubic lattice with the periodic boundary condition through Lüscher's formula. On the other hands, in the HAL QCD method, we obtain the phase shifts through hadron-hadron "potentials" calculated from the Nambu-Bethe-Salpeter (NBS) wave functions on the cubic lattice. Although these two methods are equivalent theoretically, the HAL QCD method is more suitable for the purpose in this thesis because the resultant potentials can be applied directly to several calculations in nuclear physics to investigate the properties of few-body charmed baryon systems as well as charmed hypernuclei. It will help us not only to understand the charmed baryon interactions but also to give useful information to the experiments on forthcoming facilities

such as GSI-FAIR and J-PARC.

As a first step for studying the charmed baryon interaction, we have investigated 2-body interaction between the lightest charmed baryon, Λ_c, and a nucleon in Refs. [22, 23]. In Ref. [23], we also estimate binding energies for charmed nuclei by using obtained lattice QCD potentials. We have expanded our consideration to an inelastic scattering for $\Lambda_c N$ in Refs. [24, 25], in which we have also investigated $\Sigma_c N$ interaction. In recent work, we have calculated 2-body interaction between a doubly charmed baryon and a nucleon in spin-isospin $J(I) = 0(0)$ channel, which relates to charm version of the H-dibaryon. Furthermore, very recently we have employed algorithms for the partial wave decomposition on a cubic lattice to remove lattice artifacts on the potential data [26]. The aim of this thesis is to introduce our works on the charmed baryon interactions and to present recent developments of the algorithms for potential analysis.

This thesis is organized as follows. In chapter 2, we briefly review basic concepts in the lattice QCD theory and procedures of practical lattice QCD simulations. The methodology of the HAL QCD method is given in chapter 3. In chapter 4 we present recent developments of the partial wave decomposition on a cubic lattice. The numerical results for the charmed baryon interaction are shown on a section by section in chapter 5. We not only show the potentials calculated by the HAL QCD method, but also present physical observables such as the phase shift calculated from the obtained HAL QCD potentials to discuss the 2-body interaction on the charmed baryon systems. In Sec. 5.2, after we discuss the application of the new algorithm, namely Misner's method, for the partial wave decomposition of the wave function on the cubic lattice, we present and discuss the numerical results of interactions for $\Lambda_c N$ in the elastic scattering. All of the HAL QCD potentials shown in this thesis are calculated with Misner's method. The inelastic scattering for $\Lambda_c N$ system is given in Sec. 5.3, in which the $\Sigma_c N$ interactions are also discussed. In Sec. 5.4, we show the numerical results for the doubly charmed baryon interaction in $J(I) = 0(0)$ channel and discuss the fate of the charm version of the H-dibaryon in nature. We extend our consideration to the Λ_c hypernuclei in chapter 6, and we discuss the possible Λ_c hypernuclei from the HAL QCD potentials. Finally, summary and conclusion are presented in chapter 7.

Chapter 2

Lattice QCD

First of all, we briefly review the methodology of lattice quantum chromodynamics (lattice QCD), which is one of the regularizations of QCD proposed by K. Wilson [27]. The most important utility of the lattice QCD is that path integrals in QCD can be estimated non-perturbatively by Monte-Carlo simulations.

This chapter is organized as follows. In Sec. 2.1, we first introduce the naive discretization of the QCD action in Euclidian space-time, namely naive lattice QCD action. We next show a problem in the naive lattice QCD action in Sec. 2.2, and then we introduce an improved fermion action to overcome the problem. We also present several gauge and fermion actions which improve discretization errors in Sec. 2.3. Finally, we show the procedure of Monte-Carlo simulations to calculate correlation functions on the lattice in Sec. 2.4.

2.1 Lattice QCD action

We start from the QCD Lagrangian in Minkowski space-time [1]:

$$\mathcal{L} = \bar{\psi}_i^f \left[i\gamma_\mu D_{ij}^\mu - m^f \right] \psi_j^f - \frac{1}{4} F_{\mu\nu}^a F^{a,\mu\nu}, \tag{2.1}$$

where ψ_i^f is a quark field with a flavor $f = u, d, s, c, t, b$ and a color $i = 1, 2, 3$, m^f is the quark mass of flavor f, D_{ij}^μ denotes a gauge covariant derivative, and $F_{\mu\nu}^a$ stands for a gluon field strength tensor with a space-time index $\mu, \nu = 0, 1, 2, 3$. We use Einstein

[1] The metric of Minkowski space-time in our convention is $g_{\mu\nu} = \mathrm{diag}(+1, -1, -1, -1)$

summation convention for a set of indices in a single term. In our convention, the gamma matrices are defined as

$$\gamma_0 = \begin{pmatrix} 0 & 0 & 0 & 1 \\ 0 & 0 & 1 & 0 \\ 0 & 1 & 0 & 0 \\ 1 & 0 & 0 & 0 \end{pmatrix}, \tag{2.2}$$

$$\gamma_i = \begin{pmatrix} 0 & \tau^i \\ -\tau^i & 0 \end{pmatrix}, \qquad (i = 1, 2, 3) \tag{2.3}$$

where τ^i is a Pauli matrix. The covariant derivative D^μ_{ij} and the gluon field strength tensor $F^a_{\mu\nu}$ are defined by

$$D_{ij,\mu} = \partial_\mu - ig_s T^a_{ij} G^a_\mu, \tag{2.4}$$

$$F^a_{\mu\nu} = \partial_\mu G^a_\nu - \partial_\nu G^a_\mu + g_s f^{abc} G^b_\mu G^c_\nu, \tag{2.5}$$

where G^a_μ denotes a gluon field with its coupling constant g_s. T^a_{ij} and f^{abc} stand for the generator and the structure constant of $SU(3)$, respectively.

We next show the naive lattice QCD action $S_{\rm lat}$ by discretizing the QCD action in Euclidian space-time. To this end, we first consider the Wick rotations:

$$\begin{aligned} t \equiv x_0 &\to -ix_4^{(E)}, \\ x_i &\to x_i^{(E)} \qquad (i = 1, 2, 3), \\ \partial_0 &\to i\partial_4^{(E)}, \\ \partial_i &\to \partial_i^{(E)}, \\ \gamma_0 &\to \gamma_4^{(E)}, \\ \gamma_i &\to i\gamma_i^{(E)}, \\ G_0 &\to -iG_4^{(E)}, \\ G_i &\to G_i^{(E)}, \end{aligned} \tag{2.6}$$

where (E) denotes for variables in Euclidian space-time. The QCD Lagrangian (Eq. (2.1))

is then rewritten as

$$\begin{aligned} \mathcal{L} &\rightarrow -\mathcal{L}^{(E)}, \\ \mathcal{L}^{(E)} &= \bar{\psi}_i^f \left[\gamma_\mu^{(E)} D_{ij,\mu}^{(E)} + m^f \right] \psi_j^f + \frac{1}{4} F_{\mu\nu}^{(E)a} F_{\mu\nu}^{(E)a}, \end{aligned} \tag{2.7}$$

where $D_\mu^{(E)}$ and $F_{\mu\nu}^{(E)a}$ are defined by

$$D_{ij,\mu}^{(E)} = \partial_\mu^{(E)} + i g_s T_{ij}^a G_\mu^{(E)a}, \tag{2.8}$$

$$F_{\mu\nu}^{(E)a} = \partial_\mu G_\nu^{(E)a} - \partial_\nu G_\mu^{(E)a} - g_s f^{abc} G_\mu^{(E)b} G_\nu^{(E)c}. \tag{2.9}$$

In this time, the QCD action in Euclidian space-time $S^{(E)}$ is defined as

$$\begin{aligned} d^4x &\rightarrow -i d^4x^{(E)}, \\ iS &\rightarrow -S^{(E)}, \\ S^{(E)} &= \int d^4x^{(E)} \mathcal{L}^{(E)}. \end{aligned} \tag{2.10}$$

We omit the superscript (E) in following discussions for simplicity.

Let us next consider the discretization of the space-time as

$$x_\mu \rightarrow a n_\mu \qquad (n_\mu = (n_1, n_2, n_3, n_4), n_\mu \in \mathbf{Z}), \tag{2.11}$$

where a is a lattice spacing. In order to retain the gauge invariance in the Lagrangian, we introduce following link variables

$$\begin{aligned} U(x,y) &= P \exp\left[i g_s \int_x^y G_\mu(z) dz^\mu \right] \\ &\equiv \lim_{N\to\infty} \prod_{n=0}^{N-1} \left[1 + i g_s G_\mu(x + n\Delta x) \Delta x^\mu \right], \end{aligned} \tag{2.12}$$

where $|\Delta x| = \frac{|y-x|}{N}$. Under the gauge transformation $G_\mu(x) \rightarrow \frac{1}{ig_s}\Omega(x)\partial_\mu\Omega^\dagger(x) + \Omega(x)G_\mu(x)\Omega^\dagger(x)$, while the link variables defined in Eq. (2.12) transform as gauge covariant

$$U(x,y) \rightarrow \Omega(x) U(x,y) \Omega(y)^\dagger, \tag{2.13}$$

and thus $\bar{\psi}(x)U(x,y)\psi(y)$ is gauge invariant. Therefore, it is useful to define the quark

field $\psi(x)$ on a site, and the link variable between the two quark fields, as shown in Fig. 2.1. When the lattice spacing is sufficiently small ($a \ll 1$), the link variable can be

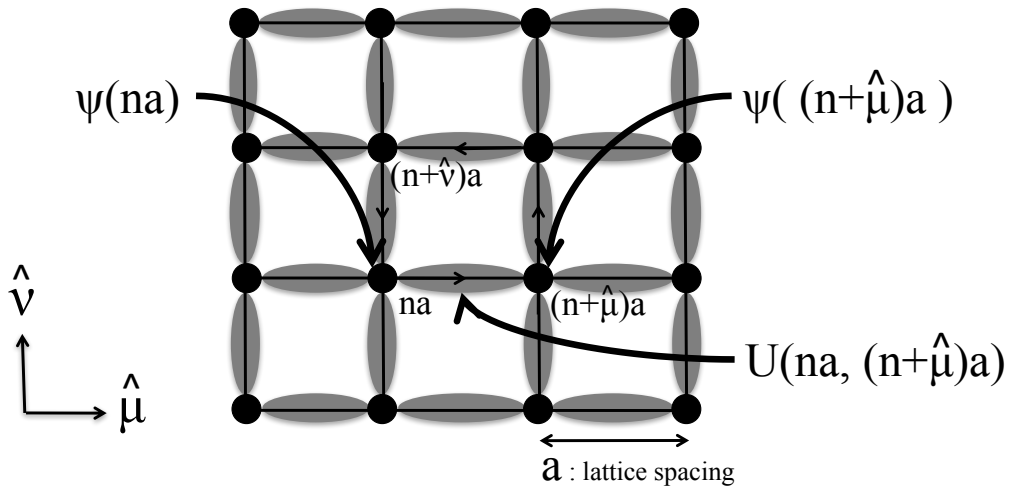

Figure 2.1: A schematics of the definitions of quark fields and link variables in two dimensional lattice.

expressed as

$$\begin{aligned} U(na,(n+\hat{\mu})a) &= P\exp\left[ig_s\int_{na}^{(n+\hat{\mu})a} G_\nu(z)dz^\nu\right] \\ &\approx \exp\left[ig_s a\delta^\nu_\mu G_\nu((n+\frac{\hat{\mu}}{2})a)\right] \\ &= \exp\left[ig_s a G_\mu((n+\frac{\hat{\mu}}{2})a)\right] \\ &\equiv U_{n,\mu}, \end{aligned} \tag{2.14}$$

where $\hat{\mu}$ denotes a unit vector in the μ direction. Note that the link variable for inverse direction is defined by

$$U_{n+\hat{\mu},-\mu} \equiv U^\dagger_{n,\mu}. \tag{2.15}$$

Using the link variables (Eq. (2.14)) and quark fields $\psi(na) \equiv \psi_n$, the most simple gauge invariant QCD action in discrete Euclidean space-time $S_{\rm lat}$ can be defined as

$$\begin{aligned} S_{\rm lat} &= S_G^{(\rm plaq)} + S_F^{(\rm naive)}, \\ S_G^{(\rm plaq)} &= -\sum_{n,\mu\neq\nu} \beta \ {\rm tr}\left[U_{n,\mu}U_{n+\hat{\mu},\nu}U^\dagger_{n+\hat{\nu},\mu}U^\dagger_{n,\nu}\right], \qquad (2.16) \\ S_F^{(\rm naive)} &= a^4 \sum_n \bar{\psi}_n \left[\sum_\mu \gamma_\mu \frac{U_{n,\mu}\psi_{n+\hat{\mu}} - U^\dagger_{n-\hat{\mu},\mu}\psi_{n-\hat{\mu}}}{2a} + m\psi_n\right], \qquad (2.17) \end{aligned}$$

where $S_G^{(\rm plaq)}$ is so-called plaquette gauge action with $\beta = 1/g_s^2$, and $S_F^{(\rm naive)}$ is naive fermion action. These actions reproduce the QCD action (Eqs. (2.7) and (2.10)) for $a \to 0$. In the practical calculation, we employ dimensionless variables for convenience:

$$\begin{aligned} \psi'_n &= a^{\frac{3}{2}}\psi_n, \\ M &= ma, \qquad (2.18) \end{aligned}$$

where the fermion action $S_F^{(\rm naive)}$ is rewritten as

$$S_F^{(\rm naive)} = \frac{1}{2}\sum_{n\mu}\left[\bar{\psi}_n\gamma_\mu U_{n,\mu}\psi_{n+\hat{\mu}} - \bar{\psi}_{n+\hat{\mu}}\gamma_\mu U^\dagger_{n,\mu}\psi_n\right] + M\sum_n \bar{\psi}_n\psi_n, \qquad (2.19)$$

where we rewrite the quark field ψ'_n as ψ_n for simplicity.

2.2 Doubling problem and Wilson fermion action

We have defined the naive lattice QCD action in the previous section. The action, however, has a well-known problem, namely doubling problem. In order to see the problem, we carry out the Fourier transformation of the fermion action (Eq. (2.19)) for $^\forall U = 1$.

$$\begin{aligned} S_F^{(\rm naive)} &= \frac{1}{2}\sum_{n\mu}\left[\bar{\psi}_n\gamma_\mu\psi_{n+\hat{\mu}} - \bar{\psi}_{n+\hat{\mu}}\gamma_\mu\psi_n\right] + M\sum_n\bar{\psi}_n\psi_n \\ &= \frac{1}{2}\sum_{n\mu}\int\frac{d^4p}{(2\pi)^4}\frac{d^4q}{(2\pi)^4}\left[\bar{\psi}(p)\gamma_\mu\psi(q){\rm e}^{-i(p+q)\cdot na}{\rm e}^{-iq_\mu a}\right. \\ &\quad \left. -\bar{\psi}(p){\rm e}^{-ip_\mu a}\gamma_\mu\psi(q){\rm e}^{-i(p+q)\cdot na}\right] + M\sum_n\int\frac{d^4p}{(2\pi)^4}\frac{d^4q}{(2\pi)^4}\bar{\psi}(p)\psi(q){\rm e}^{-i(p+q)\cdot na} \end{aligned}$$

$$
\begin{aligned}
&= \int \frac{d^4p}{(2\pi)^4}\bar{\psi}(p)\left[\frac{1}{2}\sum_\mu \gamma_\mu(\mathrm{e}^{ip_\mu a}-\mathrm{e}^{-ip_\mu a})+M\right]\psi(-p) \\
&= \int \frac{d^4p}{(2\pi)^4}\bar{\psi}(p)\left[\sum_\mu i\gamma_\mu \sin(p_\mu a)+M\right]\psi(-p). \qquad (2.20)
\end{aligned}
$$

From the action, the free quark propagator is obtained as

$$
G_F^{(\mathrm{naive})}(p) = \frac{1}{\sum_\mu i\gamma_\mu \sin(p_\mu a)+M} = \frac{-\sum_\mu i\gamma_\mu \sin(p_\mu a)+M}{\sum_\mu \sin^2(p_\mu a)+M^2}, \qquad (2.21)
$$

and the dispersion relation of the quark is given by

$$
\sum_\mu \sin^2(p_\mu a)+M^2 = 0. \qquad (2.22)
$$

In the continuum limit ($a \to 0$), one obtains a "physical" pole so that it satisfies the correct dispersion relation. Due to the properties of the sine function, however, one can also have "unphysical" poles for ${}^{\exists}p_\mu \sim \pi/a$. These extra degrees of freedom are called fermion doubler, and this problem is the so-called doubling problem. Nielsen and Ninomiya [28] show that the fermion doubler appears when the lattice theory has the following properties:

- Hermiticity
- Translational invariance
- Chiral symmetry
- Locality

This fact implies that the one cannot avoid the doubling problem unless the chiral symmetry is broken.

In order to avoid the doubling problem, several improved fermion actions have been proposed and employed extensively in practical calculations. We introduce here the Wilson fermion action, which is probably the most basic improved action proposed by Wilson [27]. The Wilson fermion action is defined by adding the following second derivative term (so-called Wilson term) to the naive lattice QCD action (Eq. (2.10)).

$$
-ar\int d^4x\ \bar{\psi}(x)D^2\psi(x), \qquad (2.23)
$$

where r is an arbitrary constant. Since the Wilson term clearly depends on lattice spacing a, the Wilson fermion action is identical with the original QCD action in the continuum limit. Discretizing the Wilson term, we have

$$-\frac{r}{2}\sum_{n,\mu}\left[\bar{\psi}_n U_{n,\mu}\psi_{n+\hat{\mu}} - \bar{\psi}_{n+\hat{\mu}}U^{\dagger}_{n,\mu}\psi_n - 2\bar{\psi}_n\psi_n\right], \tag{2.24}$$

and the Wilson fermion action in the momentum space for ${}^{\forall}U = 1$ is written as

$$S_F^{(\mathrm{Wilson})} = \int \frac{d^4p}{(2\pi)^4}\bar{\psi}(p)\left[\sum_\mu i\gamma_\mu \mathrm{sin}(p_\mu a) + M + r\sum_\mu(1-\cos(p_\mu a))\right]\psi(-p). \tag{2.25}$$

The free quark propagator is then obtained as

$$\begin{aligned} G_F^{(\mathrm{Wilson})}(p) &= \frac{1}{\sum_\mu i\gamma_\mu \mathrm{sin}(p_\mu a) + M(p)} = \frac{-\sum_\mu i\gamma_\mu \mathrm{sin}(p_\mu a) + M(p)}{\sum_\mu \mathrm{sin}^2(p_\mu a) + M(p)^2}, \\ M(p) &= M + r\sum_\mu(1-\cos(p_\mu a)). \end{aligned} \tag{2.26}$$

In the continuum limit, the momentum-dependent mass $M(p)$ becomes the original mass M for a "physical pole", while $M(p)$ becomes $M + 2rc$ $(c = 1, 2, 3, 4)$ for a doubler $({}^{\exists}p_\mu \sim \pi/a)$. Since dimensionful doubler mass $m + 2rc/a$ diverges in the continuum limit, the doubler does not contribute to the low energy physics.

2.3 Improved actions for discretization errors

The discretized lattice action with a lattice spacing a is identical to the continuum action when the a goes to zero. For a finite a, however, the two actions are different and the discretized lattice action has systematic errors with the lattice spacing a. The Wilson fermion action defined in the previous section, for instance, has $\mathcal{O}(a)$ discretization errors. The discretization errors can be improved by considering well-known procedure, Symanzik's improvement programme [29, 30]. According to Symanzik's improvement programme, the discretization errors are reduced order by order by the introduction of higher dimensional terms into the action. The general form of the improved action is written as

$$S_{\mathrm{imp}} = S_0 + \sum_{k>0} a^k \int d^4x \sum_i c_{4+k,i}(x)\mathcal{O}_{4+k,i}(x), \tag{2.27}$$

where S_0 is the standard (continuum) QCD action, $c_{d,i}(x)$ stands for an arbitrary constant, and $\mathcal{O}_{d,i}(x)$ represents a local operator with dimension d which consists of quark masses, quark and gauge fields. The operator $\mathcal{O}_{d,i}(x)$ is determined to satisfy symmetries in QCD, that is invariance under gauge, rotations, parity and charge-conjugation transformations. The on-shell $\mathcal{O}(a)$ improved fermion action was first proposed by Sheikholeslami and Wohlert in Ref. [31] using up to dimension five terms in Eq. (2.27). They found that there are two terms in the action with dimension five:

$$\mathcal{O}_{5,a}(x) = \bar{\psi}(x)D^2\psi(x) \tag{2.28}$$

$$\mathcal{O}_{5,b}(x) = i\sum_{\mu\nu}\bar{\psi}(x)\sigma_{\mu\nu}F_{\mu\nu}(x)\psi(x), \tag{2.29}$$

where $\sigma_{\mu\nu} \equiv [\gamma_\mu, \gamma_\nu]/2$. On the lattice, the field strength $F_{\mu\nu}(x)$ is expressed with link variables as

$$F_{\mu\nu}(x) = \frac{1}{4}\sum_{i=1}^{4}\frac{1}{2i}\left(U_i(x) - U_i^\dagger(x)\right) \tag{2.30}$$

$$U_1(x) = U_{x,\mu}U_{x+\hat{\mu},\nu}U^\dagger_{x+\hat{\nu},\mu}U^\dagger_{x,\nu} \tag{2.31}$$

$$U_2(x) = U_{x,\nu}U^\dagger_{x-\hat{\mu}+\hat{\nu},\mu}U^\dagger_{x-\hat{\mu},\nu}U_{x-\hat{\mu},\mu} \tag{2.32}$$

$$U_3(x) = U^\dagger_{x-\hat{\mu},\mu}U^\dagger_{x-\hat{\mu}-\hat{\nu},\nu}U_{x-\hat{\mu}-\hat{\nu},\mu}U_{x-\hat{\nu},\nu} \tag{2.33}$$

$$U_4(x) = U^\dagger_{x-\hat{\nu},\nu}U_{x-\hat{\nu},\mu}U_{x+\hat{\mu}-\hat{\nu},\nu}U^\dagger_{x,\mu}, \tag{2.34}$$

Obviously, the first term of the action with dimension five $\mathcal{O}_{5,a}(x)$ is the Wilson term shown in Eq. (2.23). The second term, $\mathcal{O}_{5,b}(x)$, is a new term introduced to eliminate the $\mathcal{O}(a)$ discretization errors, which is called Sheikholeslami-Wohlert (SW) term or Clover term. Discretizing these terms, the $\mathcal{O}(a)$ improved fermion action, which is called SW action or Wilson-clover action, is obtained as

$$\begin{aligned} S_F^{(\mathrm{Clover})} &= \sum_{nm}\bar{\psi}_n D^{(\mathrm{Clover})}_{nm}\psi_m, \\ D^{(\mathrm{Clover})}_{nm} &= \delta_{nm} - \kappa_q\sum_\mu\left[(r-\gamma_\mu)U_{n,\mu}\delta_{n+\hat{\mu},m} + (r+\gamma_\mu)U^\dagger_{n,\mu}\delta_{n,m+\hat{\mu}}\right] \\ &\quad -\kappa_q\left[c_{SW}\sum_{\mu,\nu}i\sigma_{\mu\nu}F_{\mu\nu}\right]\delta_{n,m}, \end{aligned} \tag{2.35}$$

where the coefficient c_{SW} can be determined non-perturbatively by imposing suitable so-called improvement conditions [32].

We next show the improved gauge action, namely renormalization-group (RG) improved Iwasaki gluon action [33], which is proposed to improve a cutoff scaling. This gauge action is defined by

$$S_G^{(\mathrm{Iwasaki})} = \beta \left(c_0 \sum_{n,\mu,\nu} \mathrm{tr}\left[W_{\mu\nu}^{1\times 1}(n)\right] + c_1 \sum_{n,\mu,\nu} \mathrm{tr}\left[W_{\mu\nu}^{1\times 2}(n)\right] \right), \tag{2.36}$$

where $W_{\mu\nu}^{1\times 1}(n)$ denotes a 1×1 Wilson loop (plaquette) on the $\mu-\nu$ plane starting and ending at n, and $W_{\mu\nu}^{1\times 2}(n)$ is a 1×2 rectangular Wilson loop with the side of length 2 in the ν direction on the $\mu-\nu$ plane. The coefficients are defined as $c_0 = 1-8c_1$ and $c_1 = -0.331$. Note that the action is identical to the plaquette gauge action if $c_1 = 0$. Another motivation to employ the gauge action is shown in Refs. [34, 35]. The authors had done three-flavor QCD simulation with the Wilson-clover fermion action, and then they found an unphysical first-order phase transition at zero-temperature for the plaquette gauge action, which was not found if the Iwasaki gauge action is employed.

As an application of the Wilson-clover fermion action, we next present an improved fermion action for heavy quarks. If we employ the Wilson-clover fermion action for the heavy quarks, the discretization errors are expected to be $\mathcal{O}((am_Q)^n)$ with the heavy quark mass m_Q. Under this circumstance, the systematic errors coming from the cutoff effects are sizable for a massive quark. In order to overcome the problem, Tsukuba group has proposed an improved fermion action, namely Relativistic Heavy Quark (RHQ) action [36]. The RHQ action is given by

$$\begin{aligned}
S_F^{(\mathrm{RHQ})} &= \sum_{nm} \bar{\psi}_n D_{nm}^{(\mathrm{RHQ})} \psi_m, \\
D_{nm}^{(\mathrm{RHQ})} &= \delta_{nm} - \kappa_Q \sum_{i=1}^{3} \left[(r_s - \nu\gamma_i) U_{n,i} \delta_{n+\hat{i},m} + (r_s + \nu\gamma_i) U_{n,i}^\dagger \delta_{n,m+\hat{i}} \right] \\
&\quad -\kappa_Q \left[(r_t - \gamma_4) U_{n,4} \delta_{n+\hat{4},m} + (r_t + \gamma_4) U_{n,4}^\dagger \delta_{n,m+\hat{4}} \right] \\
&\quad -\kappa_Q \left[c_B \sum_{i,j} \sigma_{ij} F_{ij} + c_E \sum_i \sigma_{i4} F_{i4} \right] \delta_{nm},
\end{aligned} \tag{2.37}$$

where κ_Q is a hopping parameter for the heavy fermion, r_s, r_t, ν, c_B and c_E are parameters

to improve the discretization errors. This formulation corresponds to dividing the time component and the spatial components in the Wilson-clover term with different coefficients. The leading $\mathcal{O}((am_Q)^n)$ discretization errors in the RHQ action can be removed by adjusting the parameter ν and quark field renormalization factor. Furthermore, the next-leading discretization errors of $\mathcal{O}((am_Q)^n a\Lambda_{\rm QCD})$ can also be removed by adjusting parameters r_s, c_E, c_B [37]. Finally, the remaining discretization errors are improved to $\mathcal{O}((a\Lambda_{\rm QCD})^2)$, which are comparative order with the light quarks. Note that the r_t is a redundant parameter so that we take $r_t = 1$.

The three actions shown in this subsection will be employed in the numerical calculations in this thesis.

2.4 Correlation function on the lattice

In this section, we show the procedure to calculate correlation functions on the lattice. Let us start from the path integral formalism for the expectation value of an observable $\mathcal{O}$:

$$\langle \mathcal{O}(\psi, \bar{\psi}, U)\rangle = \frac{\int \mathcal{D}U\mathcal{D}\bar{\psi}\mathcal{D}\psi\ \mathcal{O}(\psi,\bar{\psi},U)\ \mathrm{e}^{-S_{\rm lat}}}{\int \mathcal{D}U\mathcal{D}\bar{\psi}\mathcal{D}\psi\ \mathrm{e}^{-S_{\rm lat}}}, \tag{2.38}$$

where $S_{\rm lat}$ is the lattice QCD action defined in Eq. (2.16). An important point here is that the factor $\mathrm{e}^{-S_{\rm lat}}$ can be regarded as a probability distribution function and we can calculate the path integral numerically by Monte-Carlo method. To this end, we integrate out the fermion fields by introducing source fields $\eta, \bar{\eta}$.

$$\begin{aligned}
\langle \mathcal{O}(\psi, \bar{\psi}, U)\rangle &= \frac{\int \mathcal{D}U\mathcal{D}\bar{\psi}\mathcal{D}\psi\ \mathcal{O}(\psi,\bar{\psi},U)\ \mathrm{e}^{-S_{\rm lat}}}{\int \mathcal{D}U\mathcal{D}\bar{\psi}\mathcal{D}\psi\ \mathrm{e}^{-S_{\rm lat}}} \\
&= \left.\frac{\int \mathcal{D}U\ \mathrm{e}^{-S_G(U)}\mathcal{O}(\frac{\partial}{\partial\bar{\eta}}, -\frac{\partial}{\partial\eta}, U)\int \mathcal{D}\bar{\psi}\mathcal{D}\psi\ \mathrm{e}^{-\bar{\psi}D(U)\psi+\bar{\psi}\eta+\bar{\eta}\psi}}{\int \mathcal{D}U\ \mathrm{e}^{-S_G(U)}\int \mathcal{D}\bar{\psi}\mathcal{D}\psi\ \mathrm{e}^{-\bar{\psi}D(U)\psi}}\right|_{\eta=\bar{\eta}=0} \\
&= \left.\frac{\int \mathcal{D}U\ \mathrm{det}D(U)\mathrm{e}^{-S_G(U)}\mathcal{O}(\frac{\partial}{\partial\bar{\eta}}, -\frac{\partial}{\partial\eta}, U)\mathrm{e}^{\bar{\eta}D(U)^{-1}\eta}}{\int \mathcal{D}U\ \mathrm{det}D(U)\mathrm{e}^{-S_G(U)}}\right|_{\eta=\bar{\eta}=0} \\
&\equiv \frac{\int \mathcal{D}U\ \mathrm{det}D(U)\mathrm{e}^{-S_G(U)}Z_{\mathcal{O}}(U)}{\int \mathcal{D}U\ \mathrm{det}D(U)\mathrm{e}^{-S_G(U)}},
\end{aligned} \tag{2.39}$$

where we write the fermion action as $S_F(\psi, \bar{\psi}, U) = \bar{\psi}D(U)\psi$. In the last line of Eq. (2.39), we define $Z_{\mathcal{O}}(U)$ as $\left.\mathcal{O}(\frac{\partial}{\partial\bar{\eta}}, -\frac{\partial}{\partial\eta}, U)\mathrm{e}^{\bar{\eta}D(U)^{-1}\eta}\right|_{\eta=\bar{\eta}=0}$ which is constructed from some quark

propagators. In the case of pion two-point correlation, for instance, we obtain

$$\begin{aligned}
\mathcal{O}^{ab}(\psi,\bar{\psi}) &\equiv \pi^a(x)\pi^b(y) \qquad (\pi^a(x)=\bar{\psi}\gamma_5\tau^a\psi), \\
Z^{ab}_{\pi\pi}(U) &= \pi^a(x)\pi^b(y)\ \mathrm{e}^{\bar{\eta}D(U)^{-1}\eta}\Big|_{\eta=\bar{\eta}=0} \\
&= \left(-\frac{\partial}{\partial\eta(x)}\gamma_5\tau^a\frac{\partial}{\partial\bar{\eta}(y)}\right)\left(-\frac{\partial}{\partial\eta(y)}\gamma_5\tau^b\frac{\partial}{\partial\bar{\eta}(y)}\right)\mathrm{e}^{\bar{\eta}D(U)^{-1}\eta}\Big|_{\eta=\bar{\eta}=0} \\
&= -\mathrm{tr}\left(\gamma_5 D(U)^{-1}_{xy}\gamma_5 D(U)^{-1}_{yx}\right)\delta^{ab} + \mathrm{tr}\left(\gamma_5 D(U)^{-1}_{xx}\right)\mathrm{tr}\left(\gamma_5 D(U)^{-1}_{yy}\right)\delta^{a0}.
\end{aligned} \tag{2.40}$$

We next consider the integrals for link variables in Eq. (2.39). In a finite lattice, one can carry out the integrals numerically in principle. In practice, however, it is difficult to calculate all of the variables in a realistic time due to a limited computational resource. Therefore, we utilize the Monte-Carlo method with the importance sampling to obtain the approximate solution of the integrals. The procedure is briefly summarized as follow:

(1) Create some gauge fields with the probability

$$P(U) \propto \mathrm{det}D(U)\mathrm{e}^{-S_G(U)}, \tag{2.41}$$

by the Markov-chain Monte-Carlo method. The gauge fields obtained here are called gauge configuration.

(2) Calculate quark propagators using the created gauge configurations. The quark propagator $D(U)^{-1}_{yx_0} \equiv \phi_{x_0}(y)$ can be obtained by solving the following linear equation.

$$D(U)_{xy}\phi_{x_0}(y) = \delta_{xx_0}. \tag{2.42}$$

(3) Construct the observable $Z_{\mathcal{O}}(U)$ from the quark propagators like Eq. (2.40).

(4) Take an average for the set of observables $\{Z_{\mathcal{O}}(U)\}$. When the number of configurations is sufficiently large, one obtains

$$\lim_{N\to\infty}\frac{1}{N}\sum_{i=1}^{N} Z_{\mathcal{O}}(U_i) \ \rightarrow\ \frac{\int \mathcal{D}U\mathrm{det}D(U)\mathrm{e}^{-S_G(U)}Z_{\mathcal{O}}(U)}{\int \mathcal{D}U\mathrm{det}D(U)\mathrm{e}^{-S_G(U)}}$$

$$= \langle \mathcal{O}(\psi, \bar{\psi}, U) \rangle. \tag{2.43}$$

In the practical calculations, the uncertainty of the expectation value is estimated as the statistical errors for $\{Z_{\mathcal{O}}(U)\}$, as we discuss in Appendix A.

2.4.1 Effective mass

In this subsection, we discuss the relation between a hadron two-point correlation function and a mass of the hadron, which is extensively applied to the practical lattice QCD simulation. In order to simplify the discussion, we focus on the following pion two-point correlation function $F_{\pi\pi}$:

$$F_{\pi\pi}(t) = \sum_{\vec{x}} \langle 0|\pi(\vec{x}, t)\pi(\vec{0}, 0)|0\rangle, \tag{2.44}$$

where $\pi(x)$ is a pion field defined in Eq. (2.40). Inserting the complete set between two pion fields in Eq. (2.44), one obtains

$$F_{\pi\pi}(t) = \sum_{n} \frac{Z_\pi}{2m_n} \, e^{-m_n t} + \cdots, \tag{2.45}$$

where m_n is a mass of n-th excited state, Z_π denotes a renormalization factor of the pion field, and an ellipsis represents the contributions from states with more than two particles. From Eq. (2.45), it is clear that the contribution of the ground state becomes dominant for sufficiently large t where contributions from excited states can be negligible. In the limit $t \to \infty$, therefore, the pion two-point correlation function can be expressed as

$$F_{\pi\pi}(t) = \frac{Z_\pi}{2m_\pi} \, e^{-m_\pi t}. \tag{2.46}$$

In the practical calculation, it is useful to define an "effective mass" $m(t)$:

$$am_\pi(t) = -\log \frac{F_{\pi\pi}(t+a)}{F_{\pi\pi}(t)}, \tag{2.47}$$

where, obviously, $m_\pi(t) \to m_\pi$ for $t \to \infty$. The effective mass is useful because one can estimate the mass by plotting the $m(t)$ against the t. One can also know from the effective mass the information about the value of t where contributions from excited states can be

negligible.

Chapter 3

HAL QCD method

In this chapter, we review the basic idea of the HAL QCD method, which has been proposed by HAL QCD Collaboration [21, 38, 39, 40].

The key quantity in the HAL QCD method is the equal-time Nambu-Bethe-Salpeter (NBS) wave function. The NBS wave function (also referred to as Bethe-Salpeter amplitude) satisfies the Bethe-Salpeter equation [41] which describes the two particle scattering in field theory. In the center-of-mass frame, the NBS wave function for two particle system with spin 1/2 baryons at Euclidean time t is defined as

$$\psi_{\alpha\beta}^{(W)}(\vec{r})e^{-Wt} = \frac{1}{\sqrt{Z_{B^{(1)}}}\sqrt{Z_{B^{(2)}}}}\sum_{\vec{x}}\langle 0|B_{\alpha}^{(1)}(\vec{r}+\vec{x},t)B_{\beta}^{(2)}(\vec{x},t)|B=2;W\rangle, \tag{3.1}$$

where α and β are the spin indices, and $B_{\alpha}^{(i)}(\vec{x},t)$ $(i=1,2)$ is the local interpolating operator for a baryon $B^{(i)}$ with its renormalization factor $\sqrt{Z_{B^{(i)}}}$. The state $|B=2;W\rangle$ stands for a QCD asymptotic in-state for two baryon system at the total energy of W which is defined by $W=\sqrt{|\vec{k}|^2+m_{B^{(1)}}^2}+\sqrt{|\vec{k}|^2+m_{B^{(2)}}^2}$ with baryon masses $m_{B^{(i)}}$ and a relative momentum $\vec{k}$. The NBS wave function has two important properties: (1) it satisfies the Helmholtz equation $(k^2+\Delta)\,\psi_{\alpha\beta}^{(W)}(\vec{r})=0$ with the relative momentum $k=|\vec{k}|$ at $r=|\vec{r}|\to\infty$, and (2) it carries the information of the scattering amplitude in QCD and its asymptotic behavior at large r is identical to that of the scattering wave in quantum mechanics. These properties have been discussed and confirmed in several different systems [39, 42, 43, 44, 45, 46]. In Refs. [42, 43], two body systems for complex scalar fields in the elastic scattering have been discussed by using the LSZ reduction formula. By the same way, the discussion has been extended to the two body

systems with spin 1/2 in the elastic scattering [39], and in the inelastic scattering [44]. N-body non-relativistic systems for complex scalar fields have been considered using the Lippmann-Schwinger equation in Ref. [45]. Recently, the asymptotic behavior in complex scalar systems with one bound state has been discussed [46].

These two properties of the NBS wave function motivate us to define a "potential" from NBS wave functions through the Schrödinger equation, which is faithful to the QCD S-matrix. From the next section, we show the detail of the HAL QCD method and the derivation of the potential in the lattice QCD. In particular, we focus the interaction in a two-particle system with spin 1/2 baryons.

We divide this chapter into two sections. In Sec. 3.1, we present the HAL QCD method in the case of elastic scattering. Next, we show the extension to an inelastic scattering process in Sec 3.2, which is used to extract coupled channel potentials.

3.1 Elastic scattering case

In this section, we present the extraction of interactions in the elastic scattering on the lattice. Throughout this section, we assume the total energy W lies below the inelastic threshold. In Sec. 3.1.1, we define a "potential" from the NBS wave functions. In general, the defined potential is energy-independent and non-local. We then present how to handle the non-locality of the potential in Sec. 3.1.2. Next, we discuss the extraction of the NBS wave functions on the lattice in Sec. 3.1.3. We then also present difficulties to extract the ground state NBS wave function in lattice QCD simulation, and show the improved method for potential extraction in Sec. 3.1.4.

3.1.1 Energy-independent non-local potential

Let us show how to define the "potential" in the infinite volume. We first define a function $K_{\alpha\beta}(\vec{r},\vec{k})$ by multiplying the NBS wave function by $(|\vec{k}|^2+\vec{\nabla}^2)$:

$$\left(|\vec{k}|^2+\vec{\nabla}^2\right)\psi^{(W)}_{\alpha\beta}(\vec{r}) \equiv K_{\alpha\beta}(\vec{r},\vec{k}), \tag{3.2}$$

which corresponds to the projecting out the plane-wave component in the NBS wave function so that the function $K_{\alpha\beta}(\vec{r},\vec{k})$ is localized in r-space below the inelastic threshold [39]. When we assume that the interaction for two body system is exponentially suppressed at

large $|\vec{r}|$ and it is zero in $|\vec{r}| > R$, the NBS wave function satisfies the Helmholtz equation

$$\left(|\vec{k}|^2 + \vec{\nabla}^2\right) \psi^{(W)}_{\alpha\beta}(\vec{r}) = 0, \tag{3.3}$$

in $|\vec{r}| > R$. Note that "asymptotic momentum" $\vec{k}$ in Eq. (3.3) is determined from the relativistic total energy W. Let us next consider the spacial region in $|\vec{r}| < R$, where the interaction of two baryon system is present. In this region, we define the energy-independent non-local potential from NBS wave functions, which reproduces the correct scattering phase shift in QCD due to the asymptotic property of the NBS wave function. First, we introduce the dual basis for NBS wave functions:

$$\tilde{\psi}^{(W_k)}_{\alpha\beta}(\vec{r}) = \sum_{\alpha'\beta'} \int d^3q \; \eta^{-1}_{\alpha\beta;\alpha'\beta'}(\vec{k},\vec{q}) \; \psi^{\dagger\,(W_q)}_{\alpha'\beta'}(\vec{r}), \tag{3.4}$$

where we write $W_p = \sqrt{|\vec{p}|^2 + m^2_{B^{(1)}}} + \sqrt{|\vec{p}|^2 + m^2_{B^{(2)}}}$ for $p = k, q$. The function $\eta_{\alpha\beta;\alpha'\beta'}(\vec{k},\vec{q})$ is defined as

$$\eta_{\alpha\beta;\alpha'\beta'}(\vec{k},\vec{q}) = \int d^3r \; \psi^{\dagger\,(W_k)}_{\alpha\beta}(\vec{r}) \psi^{(W_q)}_{\alpha'\beta'}(\vec{r}). \tag{3.5}$$

From Eqs. (3.4) and (3.5), we can see that the dual basis satisfies

$$\int d^3r \; \tilde{\psi}^{(W_k)}_{\alpha\beta}(\vec{r}) \psi^{(W_q)}_{\alpha'\beta'}(\vec{r}) \;\; = \;\; \delta_{\alpha\alpha'}\delta_{\beta\beta'}\delta^{(3)}(\vec{k}-\vec{q}). \tag{3.6}$$

We then define the non-local potential by using the dual basis and Eq. (3.2) as

$$U_{\alpha\beta;\alpha'\beta'}(\vec{r},\vec{r'}) \equiv \int d^3k \; K_{\alpha\beta}(\vec{r},\vec{k}) \tilde{\psi}^{(W_k)}_{\alpha'\beta'}(\vec{r'}), \tag{3.7}$$

where the non-local potential $U_{\alpha\beta;\alpha'\beta'}(\vec{r},\vec{r'})$ is energy-independent due to the integral of k in the right-hand side of Eq. (3.7). By using Eqs. (3.6) and (3.7), we finally obtain the following equation.

$$K_{\alpha\beta}(\vec{r},\vec{k}) = \left(|\vec{k}|^2 + \vec{\nabla}^2\right) \psi^{(W)}_{\alpha\beta}(\vec{r}) = \sum_{\alpha'\beta'} \int d^3r' U_{\alpha\beta;\alpha'\beta'}(\vec{r},\vec{r'}) \psi^{(W)}_{\alpha'\beta'}(\vec{r'}). \tag{3.8}$$

When we rescale the potential as $U = 2\mu\tilde{U}$ and rewrite $\tilde{U} \to U$, the Eq. (3.8) can be written as the Schrödinger equation for non-local potential:

$$(E_k - H_0)\,\psi^{(W)}_{\alpha\beta}(\vec{r}) = \sum_{\alpha'\beta'} \int d^3r' U_{\alpha\beta;\alpha'\beta'}(\vec{r},\vec{r'})\psi^{(W)}_{\alpha'\beta'}(\vec{r'}), \tag{3.9}$$

where $E_k = k^2/2\mu$ and $H_0 = -\nabla^2/2\mu$. The important point here is that we don't need any non-relativistic approximations for the derivation of Eq. (3.9).

3.1.2 Derivative expansion of non-local potential

In principle, the energy-independent non-local potential can be extracted from the NBS wave functions through Eq. (3.7). In practice, however, it is difficult to have all energy states of the NBS wave function in the lattice QCD simulation. We therefore introduce the derivative expansion (also referred to as velocity expansion) of the non-local potential as

$$U(\vec{r},\vec{r'}) = V(\vec{r},\vec{\nabla})\delta^{(3)}(\vec{r}-\vec{r'}), \tag{3.10}$$

where $V(\vec{r},\vec{\nabla})$ is then expanded in terms of $\vec{\nabla}$. The structure of $V(\vec{r},\vec{\nabla})$ can be determined by imposing several conditions that the potential should satisfy. In the case of a two-baryon system with spin 1/2, we have [47]

$$V(\vec{r},\vec{\nabla}) = V_0(r) + V_\sigma(r)(\vec{\sigma}_1\cdot\vec{\sigma}_2) + V_{\rm T}(r)S_{12} + V_{\rm LS}(r)\vec{L}\cdot\vec{S} + {\rm O}(\vec{\nabla}^2), \tag{3.11}$$

where $r = |\vec{r}|$, $\vec{\sigma}_i$ is the Pauli matrix acting on the spin index of i-th baryon, $\vec{S} = (\sigma_1+\sigma_2)/2$ is the total spin operator, $\vec{L} = \vec{r}\times i\vec{\nabla}$ is the angular momentum operator, and S_{12} stands for the tensor operator defined as

$$S_{12} = 3\frac{(\vec{r}\cdot\vec{\sigma}_1)(\vec{r}\cdot\vec{\sigma}_2)}{r^2} - \vec{\sigma}_1\cdot\vec{\sigma}_2. \tag{3.12}$$

If the baryons in the system have non-zero isospin, each local potential is further decomposed into isospin-independent and isospin-dependent potential, as $V_X(\vec{r}) = V_X^\tau(r) + V_X^\tau(r)(\vec{\tau}_1\cdot\vec{\tau}_2)$ with the Pauli matrix $\vec{\tau}_i$ acting on the isospin index if i-th baryon. The first three terms in Eq. (3.11) are the 0-th order of the derivative and we call these terms as the leading order (LO) of the derivative expansion, while the fourth term is the next-

to-leading order (NLO) which is the first order of the derivative. The local potentials in LO term such as $V_0, V_\sigma, V_{\rm T}$ which give the spin-independent force, the spin-spin force and the tensor force are commonly used in nuclear physics. We can obtain the LO potential $V_{\rm LO}(r) = V_0(r) + V_\sigma(r)(\vec{\sigma}_1 \cdot \vec{\sigma}_2) + V_{\rm T}(r)S_{12}$ from the NBS wave function at one value of W as long as the contributions from higher order term are negligible. In the case of S-wave spin-singlet state of the NBS wave function $\psi^W_{^1S_0}(\vec{r})$, for instance, we have

$$V_{\rm LO}^{^1S_0}(r) = \frac{(E_k - H_0)\,\psi^{(W)}_{^1S_0}(\vec{r})}{\psi^{(W)}_{^1S_0}(\vec{r})}, \tag{3.13}$$

where $V_{\rm LO}^{^1S_0}(r) = V_0(r) - 3V_\sigma(r)$ since $S_{12}\psi^{(W)}_{^1S_0} = 0$ and $(\vec{\sigma}_1 \cdot \vec{\sigma}_2)\psi^{(W)}_{^1S_0} = -3\psi^{(W)}_{^1S_0}$. In general, a truncation of the derivative expansion of the non-local potential up to the LO may generate the energy dependence in the LO potential. The convergence of the derivative expansion can be checked by examining the W dependence of the LO potential. [48]. If we confirm that the derivative expansion of the non-local potential is a reasonably good approximation, we can use the local potentials to investigate the several scattering problems.

3.1.3 Extraction of NBS wave functions on the lattice

In this section, we present how to extract the NBS wave functions on the lattice. As discussed in Sec. 2.4, quantities that we can calculate on the lattice are correlation functions for quarks. The best quantities to obtain the NBS wave functions are baryon four-point correlation function given by

$$G_{\alpha\beta}(\vec{r}, t - t_0) = \sum_{\vec{x}} \langle 0 | B^{(1)}_\alpha(\vec{r} + \vec{x}, t) B^{(2)}_\beta(\vec{x}, t) \mathcal{J}^{(J^P)}(t_0) | 0 \rangle, \tag{3.14}$$

where the baryon operator $B^{(i)}_\alpha(\vec{x}, t)$ $(i = 1, 2)$ is a composite operator constructed from three quark operators, which is the same definition with one in Eq. (3.1). The source operator $\mathcal{J}^{(J^P)}(t_0)$ is defined so that it creates two baryon states with the total angular momentum J and the parity P at $t = t_0$. Explicitly, the source operator is defined as

$$\mathcal{J}^{(J^P)}(t_0) = P^{(J^P)}_{\alpha\beta} \overline{B^{(2)}_\beta}(t_0) \overline{B^{(1)}_\alpha}(t_0), \tag{3.15}$$

where $P^{(J^P)}_{\alpha\beta}$ stands for the projection operator to the total angular momentum J and the parity P. Here $B^{(i)}_\alpha(t_0)$ $(i = 1, 2)$ is obtained by replacing the quark operator $q(\vec{x}, t)$ in the $B^{(i)}_\alpha(\vec{x}, t)$ with a smearing quark operator given by

$$q(t_0) = \sum_{\vec{x}} f_{\rm smear}(\vec{x}) q(\vec{x}, t_0), \tag{3.16}$$

where $f_{\rm smear}(\vec{x})$ is a smearing function. In this thesis, we exclusively employ the wall-source for the source operator, given by $f_{\rm wall}(\vec{x}) = 1/V$ with the lattice volume V. Note that since the gauge covariance is broken by quark smearing, we need a gauge fixing at $t = t_0$.

The baryon four-point correlation function can be expanded in term of the NBS wave functions as follows. We first consider the complete set of the QCD eigenstates for two baryon system in a finite box

$$1 = \sum_n |B = 2; W_n\rangle\langle B = 2; W_n| + \cdots, \tag{3.17}$$

where $|B = 2; W_n\rangle$ stands for the n-th energy eigenstate in the elastic scattering with the energy W_n, and the ellipses represent contributions from inelastic states. Inserting the complete set between the two baryon operators and the source operator in the Eq. (3.14), we obtain

$$\begin{aligned} G_{\alpha\beta}(\vec{r}, t - t_0) &= \sum_n \sum_{\vec{x}} \langle 0|B^{(1)}_\alpha(\vec{r} + \vec{x}, t) B^{(2)}_\beta(\vec{x}, t)|W_n\rangle\langle W_n|\mathcal{J}^{(J^P)}(t_0)|0\rangle + \cdots \\ &= \sqrt{Z_{B^{(1)}}}\sqrt{Z_{B^{(2)}}} \sum_n \psi^{(W_n)}_{\alpha\beta}(\vec{r}) e^{-W_n(t-t_0)} A_n + \cdots, \end{aligned} \tag{3.18}$$

with a constant $A_n = \langle W_n|\mathcal{J}^{(J^P)}(0)|0\rangle$, where we use $|W_n\rangle$ to represent $|B = 2; W_n\rangle$ for simplicity. Here $\psi^{(W_n)}_{\alpha\beta}(\vec{r})$ is indeed the NBS wave function with the energy W_n defined in Eq. (3.1). When the time separation $t - t_0$ is sufficiently large, the baryon four-point function is dominated by the NBS wave function of the ground state:

$$G_{\alpha\beta}(\vec{r}, t - t_0) \to \sqrt{Z_{B^{(1)}}}\sqrt{Z_{B^{(2)}}} \psi^{(W_0)}_{\alpha\beta}(\vec{r}) e^{-W_0(t-t_0)} A_0 + \mathcal{O}(e^{-W_1(t-t_0)}). \tag{3.19}$$

Therefore, the LO potential can be extracted by using the baryon four-point correlation

function at large $t - t_0$. For example, in the case of S-wave spin-singlet state, we obtain

$$V_{\rm LO}^{^1S_0}(r) = \frac{(E_k - H_0)\, G_{^1S_0}(\vec{r}, t - t_0)}{G_{^1S_0}(\vec{r}, t - t_0)} \to \frac{(E_k - H_0)\, \psi_{^1S_0}^{(W_0)}(\vec{r})}{\psi_{^1S_0}^{(W_0)}(\vec{r})}, \tag{3.20}$$

at $t - t_0 \to \infty$.

We can observe from Eqs. (3.18) and (3.20) that a choice of source operator does not change the potential obtained from the baryon four-point correlation function at $t - t_0 \to \infty$. In practice, however, the time separation $t - t_0$ is finite and the choice of source operator is related to the domination of the ground state NBS wave function in the baryon four-point correlation function: the domination of $\psi^{(W_0)}$ is reasonably good in large $t - t_0$ if $A_0 \gg A_1$, while the non-negligibly contamination from the higher energy states $\psi^{(W_1)}$ may remain even in very large $t - t_0$ if $A_0 \ll A_1$. In other words, the good choice of the source operator generates better signals for the ground state NBS wave function (also for the potential).

We next consider a rough estimation of $t - t_0$ that the ground state domination is achieved. In the case of a two-nucleon system, the signal to noise ratio of the four-point correlation function is estimated by

$$\mathcal{S}/\mathcal{N} \sim \sqrt{N_{\rm stat}}\ \exp\left[-2(m_N - \frac{3}{2}m_\pi)(t - t_0)\right], \tag{3.21}$$

where $N_{\rm stat}$ is the number of statistics for the four-point correlation function. The energy separation of each energy eigenstate is calculated as

$$\delta W = W_{n+1} - W_n \sim \frac{\delta k^2}{m_N}, \tag{3.22}$$

$$\delta k^2 = \left(\frac{2\pi}{L}\right)^2. \tag{3.23}$$

When a lattice size is $L \sim 8$ fm and the nucleon mass is $m_N \sim 1000$ MeV, the energy separation is calculated as $\delta W \sim 20$ MeV. Under the assumption that $A_0 \sim A_i$ $(i > 0)$ and $\sqrt{Z_N} \sim 1$, the four-point correlation function is written as

$$G_{\alpha\beta}(\vec{r}, t - t_0) \sim \psi_{\alpha\beta}^{(W_0)}(\vec{r}) + \mathcal{O}(e^{-\delta W(t - t_0)}). \tag{3.24}$$

We then obtain the ground state NBS wave function $\psi_{\alpha\beta}^{(W_0)}(\vec{r})$ with the contamination from

higher energy states at $\mathcal{O}(e^{-1})$ at $t-t_0 = 10$ fm, where $\mathcal{S}/\mathcal{N} \sim \sqrt{N_{\rm stat}} \times 10^{-32}$. Therefore, we need $N_{\rm stat} > 10^{64}$ even though the signal to noise ratio is equal to one. Although these are rough estimations, one may see the difficulty of the ground state domination in the NBS wave function with a reasonable $\mathcal{S}/\mathcal{N}$. Especially, it is more difficult to achieve the ground state domination in the larger volume since the energy separation of each energy eigenstate becomes smaller. In fact, large statical noises of the baryon four-point correlation function in the large $t - t_0$ are common problems in the lattice QCD [49, 50].

3.1.4 Time-dependent HAL QCD method

In the previous section, we present the extraction of the potential from baryon four-point correlation function calculated on the lattice and show that the ground state domination of the NBS wave function is needed to extract the potential but it is difficult in the practical simulation due to large statistical noises. In this section, we introduce the improved method proposed in Ref. [51] to extract the potential without assuming the ground state domination.

We first define the normalized baryon four-point correlation function, so-called R-correlator, as

$$\begin{aligned} R_{\alpha\beta}(\vec{r}, t-t_0) &\equiv \frac{G_{\alpha\beta}(\vec{r}, t-t_0)}{e^{-m_{B^{(1)}}(t-t_0)} e^{-m_{B^{(2)}}(t-t_0)}} \\ &= \sum_n \psi^{(W_n)}_{\alpha\beta}(\vec{r}) e^{-\Delta W_n (t-t_0)} A_n + \cdots , \end{aligned} \tag{3.25}$$

where $\Delta W_n = W_n - (m_{B^{(1)}} + m_{B^{(2)}}) = \sqrt{k_n^2 + m_{B^{(1)}}^2} + \sqrt{k_n^2 + m_{B^{(2)}}^2} - (m_{B^{(1)}} + m_{B^{(2)}})$. We omit the Z-factors here for simplicity. In the case of $m_{B^{(1)}} = m_{B^{(2)}} \equiv m$, we can find the following relation about the ΔW_n.

$$\begin{aligned} (\Delta W_n)^2 &= \left(2\sqrt{k_n^2 + m^2} - 2m\right)^2 \\ &= 4k_n^2 + 4m^2 - 8m\sqrt{k_n^2 + m^2} + 4m^2 \\ &= 4k_n^2 - 4m\left(2\sqrt{k_n^2 + m^2} - 2m\right) \\ &= 4k_n^2 - 4m\Delta W_n. \\ \Rightarrow \quad \frac{k_n^2}{m} &= \Delta W_n + \frac{1}{4m}(\Delta W_n)^2. \end{aligned} \tag{3.26}$$

Since

$$\begin{aligned}\frac{\partial}{\partial t}R_{\alpha\beta}(\vec{r},t-t_0) &= \sum_n \psi^{(W_n)}_{\alpha\beta}(\vec{r})\frac{\partial}{\partial t}e^{-\Delta W_n(t-t_0)}A_n+\cdots \\ &= \sum_n \psi^{(W_n)}_{\alpha\beta}(\vec{r})\left(-\Delta W_n\right)e^{-\Delta W_n(t-t_0)}A_n+\cdots, \end{aligned} \tag{3.27}$$

we can extract the potential from the R-correlator as follows.

$$\begin{aligned}&\left[-\frac{\partial}{\partial t}+\frac{1}{4m}\frac{\partial^2}{\partial t^2}-H_0\right]R_{\alpha\beta}(\vec{r},t-t_0) \\ =&\sum_n\left[-\frac{\partial}{\partial t}+\frac{1}{4m}\frac{\partial^2}{\partial t^2}-H_0\right]\psi^{(W_n)}_{\alpha\beta}(\vec{r})e^{-\Delta W_n(t-t_0)}A_n+\cdots \\ =&\sum_n\left[\Delta W_n+\frac{1}{4m}(\Delta W_n)^2-H_0\right]\psi^{(W_n)}_{\alpha\beta}(\vec{r})e^{-\Delta W_n(t-t_0)}A_n+\cdots \\ =&\sum_n\left[E_n-H_0\right]\psi^{(W_n)}_{\alpha\beta}(\vec{r})e^{-\Delta W_n(t-t_0)}A_n+\cdots \\ =&\sum_n\int d^3r' U_{\alpha\beta;\alpha'\beta'}(\vec{r},\vec{r'})\psi^{(W_n)}_{\alpha'\beta'}(\vec{r'})e^{-\Delta W_n(t-t_0)}A_n+\cdots \\ =&\int d^3r' U_{\alpha\beta;\alpha'\beta'}(\vec{r},\vec{r'})R_{\alpha'\beta'}(\vec{r'},t-t_0)+\cdots \end{aligned} \tag{3.28}$$

where we use Eqs. (3.26) and (3.9). One of the most important points here is that the energy-independent potential is defined not only from the ground state NBS wave function but also from all of the momentum excited (elastic) states. That is, the excited states are no longer "contaminations" but we can use them as "signals" of the potential. Therefore, we don't need the ground state domination of the NBS wave function and we can obtain the potential at moderately large $t-t_0$ where contributions from the inelastic states can be neglected. Since we use the time-derivative for the R-correlator, this method is called by time-dependent HAL QCD method.

In order to see how much the signal to noise ratio is improved, let us again estimate $t-t_0$ that contributions from the inelastic states can be neglected. We assume that the contributions from inelastic states for the potential are regarded as $\mathcal{O}(e^{-\delta W_{\rm th}(t-t_0)})$, where $\delta W_{\rm th}$ is an energy separation between the ground state and the first inelastic threshold. In the case of a two-nucleon system, the first inelastic contribution may be coming from $NN\pi$. When the pion mass is $m_\pi = 200$ MeV, we obtain the potential at $t-t_0 = 2$ fm with the contaminations from inelastic states at $\mathcal{O}(e^{-1})$. At this time, the signal to noise

ratio (Eq. (3.21)) is estimated as $\mathcal{S}/\mathcal{N} \simeq \sqrt{N_{\rm stat}} \times 10^{-2}$. Therefore, we need $N_{\rm stat} > 10^4$ for $\mathcal{S}/\mathcal{N} \simeq 1$, which is an enormous improvement compared to the case of the ground state domination.

We next consider the meaning of the time derivatives in Eq. (3.28). In the non-relativistic approximation ($k_n^2 \ll m^2$), ΔW_n is estimated by

$$\begin{aligned} \Delta W_n &= 2\sqrt{k_n^2 + m^2} - 2m \\ &= 2m\sqrt{1 + \frac{k_n^2}{m^2}} - 2m \\ &\simeq 2m\left(1 + \frac{k_n^2}{2m^2}\right) - 2m \\ &= \frac{k_n^2}{m}. \end{aligned} \tag{3.29}$$

Comparing with Eq. (3.26), we find that the ΔW_n corresponds to the non-relativistic energy and $\frac{1}{4m}(\Delta W_n)^2$ is a relativistic correction term. In other words, the second time derivative term $\frac{1}{4m}\frac{\partial^2}{\partial t^2}$ in Eq. (3.28) corresponds to the relativistic correction for the potential.

In the case of $m_{B^{(1)}} \neq m_{B^{(2)}}$, Eq. (3.26) becomes complicated as (see Appendix B for detailed derivations)

$$\frac{k_n^2}{2\mu} = \Delta W_n + \frac{1+3\delta^2}{8\mu}\left(\Delta W_n\right)^2 + \mathcal{O}\left(\left(\Delta W_n\right)^3\right), \tag{3.30}$$

where $\delta = (m_{B^{(1)}} - m_{B^{(2)}})/(m_{B^{(1)}} + m_{B^{(2)}})$. Up to $\mathcal{O}\left((\Delta W_n)^2\right)$, we obtain the following equation for R-correlators by the same procedure as Eq. (3.28),

$$\left[\left(\frac{1+3\delta^2}{8\mu}\right)\frac{\partial^2}{\partial t^2} - \frac{\partial}{\partial t} - H_0\right] R_{\alpha\beta}(\vec{r}, t - t_0) = \int d^3r' U_{\alpha\beta;\alpha'\beta'}(\vec{r}, \vec{r'}) R_{\alpha'\beta'}(\vec{r'}, t - t_0), \tag{3.31}$$

for moderately large $t - t_0$ (where contributions from the inelastic states can be neglected). The higher order terms in Eq. (3.30) can be calculated by corresponding time derivative. They are, however, expected to be small at low energies and the effects of higher-derivative terms, as well as the contribution from inelastic states, are regarded as the systematic errors and estimated by the time-dependence of potentials. Note that Eq. (3.31) becomes identical to Eq. (3.28) for $m_{B^{(1)}} = m_{B^{(2)}}$.

3.1.5 Effective central potential and Operator basis potential

We present here how to calculate the central and tensor potentials in the case of two baryon system with spin 1/2, which are practically used for analysis in this thesis. Since we use only the time-dependent HAL QCD method in the analysis, we define the potential in this section by the time-dependent HAL QCD method. As we shown in Sec. 3.1.2 (for the infinite volume) and in Sec. 3.1.3 (for a finite volume), the leading order potential in an S-wave spin-singlet system is defined by

$$V_{\rm LO}^{^1S_0}(r) = \frac{1}{R_{^1S_0}(\vec{r}, t-t_0)} \left[\left(\frac{1+3\delta^2}{8\mu} \right) \frac{\partial^2}{\partial t^2} - \frac{\partial}{\partial t} - H_0 \right] R_{^1S_0}(\vec{r}, t-t_0), \tag{3.32}$$

for sufficiently large $t - t_0$, where $R_{^1S_0}(\vec{r}, t-t_0)$ is defined as

$$R_{^1S_0}(\vec{r}, t-t_0) \equiv P^{(L=0)} P^{(S=0)}_{\beta\alpha} R_{\alpha\beta}(\vec{r}, t-t_0), \tag{3.33}$$

with projection operators to the total spin $S = 0$ and the orbital angular momentum $L = 0$. In the continuum space, the projection operator $P^{(L=0)}$ corresponds to the spherical surface integral. On the lattice, however, we instead employ the cubic transformation group for the projection because the integral cannot be carried out. We then define the projection $P^{(L=0)}$ as

$$P^{(L=0)} R(\vec{r}, t-t_0) \equiv \frac{1}{24} \sum_{g \in SO(3,Z)} R(g^{-1}\vec{r}, t-t_0), \tag{3.34}$$

where g is one of 24 elements in $SO(3, Z)$ group. This projection picks up an A_1^+ representation of $SO(3, Z)$ group, which contains not only $L = 0$ component but also the higher components with $L \geq 4$ [48]. We expect, however, that contributions from $L \geq 4$ states are negligible at low energies, as seen in Chap. 4.

Next, we consider the leading order potential in an S-wave spin-triplet system. Using the projection operator to the $S = 1$, we define the potential as

$$V_{\rm LO}^{^3S_1}(r) = \frac{1}{R_{^3S_1}(\vec{r}, t-t_0)} \left[\left(\frac{1+3\delta^2}{8\mu} \right) \frac{\partial^2}{\partial t^2} - \frac{\partial}{\partial t} - H_0 \right] R_{^3S_1}(\vec{r}, t-t_0), \tag{3.35}$$

where $R_{^3S_1}(\vec{r}, t-t_0)$ is

$$R_{^3S_1}(\vec{r}, t-t_0) \equiv P^{(L=0)} P^{(S=1)}_{\beta\alpha} R_{\alpha\beta}(\vec{r}, t-t_0). \tag{3.36}$$

In this system, the ${}^3D_1$ state couples with the ${}^3S_1$ state because the angular momentum is not a good quantum number in QCD. Therefore, the potential $V_{\rm LO}^{{}^3S_1}(r)$ here is an effective central potential which implicitly includes the effect of the tensor potential through the virtual processes such as ${}^3S_1 \to {}^3D_1 \to {}^3S_1$. If the tensor potential is sufficiently weak, the interaction in ${}^3S_1$ system is described well by the effective potential $V_{\rm LO}^{{}^3S_1}(r)$. If the tensor potential is large, however, It is better to use the tensor potential directory to solve the Schrödinger equation. To this end, we introduce the D-wave projection as $P^{(L=2)} \equiv (1 - P^{(L=0)})$, and construct the coupled channel equation for S-wave and D-wave by acting $P^{(L=0)}$ and $P^{(L=2)}$ to Eq. (3.31) with $U(\vec{r}, \vec{r'}) \simeq V_{\rm LO}(\vec{r})\delta^{(3)}(\vec{r} - \vec{r'})$,

$$\begin{aligned}
\mathcal{K}\left[P^{L=0}R_{\alpha\beta}(\vec{r})\right] &= V_C^{1+}(\vec{r})\left[P^{L=0}R_{\alpha\beta}(\vec{r})\right] + V_T(\vec{r})\left[P^{L=0}(S_{12}R)_{\alpha\beta}(\vec{r})\right] \\
\mathcal{K}\left[P^{L=2}R_{\alpha\beta}(\vec{r})\right] &= V_C^{1+}(\vec{r})\left[P^{L=2}R_{\alpha\beta}(\vec{r})\right] + V_T(\vec{r})\left[P^{L=2}(S_{12}R)_{\alpha\beta}(\vec{r})\right], \quad (3.37)
\end{aligned}$$

where $\mathcal{K}$ is the operator in the left-hands of Eq. (3.31), given by

$$\mathcal{K} \equiv \left(\frac{1+3\delta^2}{8\mu}\right)\frac{\partial^2}{\partial t^2} - \frac{\partial}{\partial t} - H_0, \quad (3.38)$$

and we omit $t - t_0$ in R-correlator for simplicity. We define $V_C^{1+}(\vec{r})$ as the central potential part in the $V_{\rm LO}$ which is given $V_C^{1+}(r) = V_0(r) + V_\sigma(r)$ since $(\vec{\sigma}_1 \cdot \vec{\sigma}_2)\psi_{{}^3S_1}^{(W)} = \psi_{{}^3S_1}^{(W)}$. From Eq. (3.37), we have

$$\begin{pmatrix} V_C^{1+}(\vec{r}) \\ V_T(\vec{r}) \end{pmatrix} = \begin{pmatrix} P^{L=0}R_{\alpha\beta}(\vec{r}) & P^{L=0}(S_{12}R)_{\alpha\beta}(\vec{r}) \\ P^{L=2}R_{\alpha\beta}(\vec{r}) & P^{L=2}(S_{12}R)_{\alpha\beta}(\vec{r}) \end{pmatrix}^{-1} \begin{pmatrix} \mathcal{K}\left[P^{L=0}R_{\alpha\beta}(\vec{r})\right] \\ \mathcal{K}\left[P^{L=2}R_{\alpha\beta}(\vec{r})\right] \end{pmatrix}, \quad (3.39)$$

for given $\alpha.\beta$.

Finally, we show conversions of the central potentials into the operator basis potentials, such as V_0 and V_σ. From the definitions of the $V_{LO}^{{}^1S_0}(r)$ and $V_C^{1+}(r)$, the spin-independent potential V_0 and spin-spin potential V_σ are extracted as

$$\begin{pmatrix} V_0(\vec{r}) \\ V_\sigma(\vec{r}) \end{pmatrix} = \frac{1}{4}\begin{pmatrix} 1 & 3 \\ -1 & 1 \end{pmatrix}\begin{pmatrix} V_{LO}^{{}^1S_0}(\vec{r}) \\ V_C^{1+}(\vec{r}) \end{pmatrix}, \quad (3.40)$$

for systems with an isospin 0 particle. If the particles in the system have non-zero isospin, the potentials are further decomposed into isospin-independent part and isospin-dependent part. In the case of $\Sigma_c N$ system which has isospin 1/2 and 3/2, the operator

basis potentials are given as

$$\begin{pmatrix} V_0^0(\vec{r}) \\ V_\sigma^0(\vec{r}) \\ V_0^\tau(\vec{r}) \\ V_\sigma^\tau(\vec{r}) \end{pmatrix} = \frac{1}{24} \begin{pmatrix} 2 & 6 & 4 & 12 \\ -2 & 2 & -4 & 4 \\ -1 & -3 & 1 & 3 \\ 1 & -1 & -1 & 1 \end{pmatrix} \begin{pmatrix} V_{LO}^{^1S_0,\ I=1/2}(\vec{r}) \\ V_C^{1+,\ I=1/2}(\vec{r}) \\ V_{LO}^{^1S_0,\ I=3/2}(\vec{r}) \\ V_C^{1+,\ I=3/2}(\vec{r}) \end{pmatrix}, \tag{3.41}$$

for central potentials, and

$$\begin{pmatrix} V_T^0(\vec{r}) \\ V_T^\tau(\vec{r}) \end{pmatrix} = \frac{1}{6} \begin{pmatrix} 2 & 4 \\ -1 & 1 \end{pmatrix} \begin{pmatrix} V_T^{I=1/2}(\vec{r}) \\ V_T^{I=3/2}(\vec{r}) \end{pmatrix}, \tag{3.42}$$

for tensor potentials.

3.2 Inelastic scattering case

In this section, we briefly review the HAL QCD method extended to an inelastic scattering process [44, 52], such as $a+b \to c+d$, where a, b, c, and d are arbitrary one-particle states. We assume here that the total energy W is larger than the mass threshold of each channel, namely $W > m_c + m_d > m_a + m_b$. As in the case of the elastic scattering in Sec. 3.1, we focus two particle system with spin 1/2 baryons. Although this method can be applied to arbitrary multi-particle scattering processes [45], we present the formulation for the two-channel case for simplicity. In Sec. 3.2.1, we define the coupled channel Schrödinger equation for non-local potentials from NBS wave functions. The extraction of the coupled channel potentials from NBS wave functions on the lattice is presented in Sec. 3.2.2. As shown in Sec. 3.1.3, one of the problems in the practical simulation is that it is difficult to obtain the ground state NBS wave function due to large statistical noises. The improved method, time-dependent HAL QCD method, can overcome such a problem as shown in Sec. 3.1.4. In Sec. 3.2.3 we apply the time-dependent HAL QCD method to the coupled channel Schrödinger equation.

3.2.1 Coupled channel Schrödinger equation for non-local potentials

We first define NBS wave functions for channel $X = [ab], [cd]$ in the center of mass frame,

$$\psi^{(W)}_{X,\xi}(\vec{r})e^{-Wt} = \frac{1}{\sqrt{Z_{X_1}}\sqrt{Z_{X_2}}}\sum_{\vec{x}}\langle 0|B_{X_1,\xi_1}(\vec{r}+\vec{x},t)B_{X_2,\xi_2}(\vec{x},t)|B=2;W\rangle \tag{3.43}$$

where $B_{X_i,\xi_i}(\vec{x},t)$ $(X_i = a,b,c,d)$ is the local interpolating operator for a baryon X_i with its renormalization factor $\sqrt{Z_{X_i}}$, and $|B=2;W\rangle$ stands for a QCD asymptotic in-state for two baryon system at the total energy of W which is defined by $W = \sqrt{|\vec{k}_{ab}|^2+m_a^2}+\sqrt{|\vec{k}_{ab}|^2+m_b^2} = \sqrt{|\vec{k}_{cd}|^2+m_c^2}+\sqrt{|\vec{k}_{cd}|^2+m_d^2}$ with the baryon mass m_{X_i} and the relative momentum $\vec{k}_X$ for the channel X. Here ξ represents quantum numbers other than W, such as spin. In the infinite volume, the energy eigenstate $|B=2;W\rangle$ can be expressed in terms of the asymptotic in-states in channel $[ab]$ and $[cd]$ as

$$|B=2;W\rangle = c_{ab}|ab;W\rangle + c_{cd}|cd;W\rangle + \cdots, \tag{3.44}$$

$$|ab;W\rangle = |a;\vec{k}_{ab}\rangle_{\rm in}\otimes|b;-\vec{k}_{ab}\rangle_{\rm in}, \tag{3.45}$$

$$|cd;W\rangle = |c;\vec{k}_{cd}\rangle_{\rm in}\otimes|d;-\vec{k}_{cd}\rangle_{\rm in}, \tag{3.46}$$

where c_X is arbitrary constant, and $|X_i;\vec{k}_X\rangle_{\rm in}$ denotes an asymptotic state for a baryon X_i with the momentum $\vec{k}_X$. We then define the function $K_{X,\xi}(\vec{r},\vec{k})$ multiplying the NBS wave functions by $\left(|\vec{k}_X|^2+\vec{\nabla}^2\right)$:

$$\left(|\vec{k}_X|^2+\vec{\nabla}^2\right)\psi^{(W)}_{X,\xi}(\vec{r}) \equiv K_{X,\xi}(\vec{r},\vec{k}). \tag{3.47}$$

For $|\vec{r}| > R$ in which all of two body interactions are absent, the NBS wave functions satisfy the Helmholtz equation

$$\left(|\vec{k}_X|^2+\vec{\nabla}^2\right)\psi^{(W)}_{X,\xi}(\vec{r}) = 0, \tag{3.48}$$

and the NBS wave functions carry the information of scattering amplitude until the new channel opens and their asymptotic behaviors are similar to those of scattering waves in Quantum mechanics even without non-relativistic approximation [44].

For $|\vec{r}| < R$, on the other hand, we define non-local potentials through the coupled-

channel Schrödinger equation as the same procedure in the case of elastic scattering. First, we introduce the dual basis for NBS wave function in channel X:

$$\tilde{\psi}^{(W_k)}_{X,\xi}(\vec{r}) = \sum_{\zeta} \int d^3q \; \eta^{-1}_{\xi,\zeta}(\vec{k},\vec{q}) \; \psi^{\dagger\,(W_q)}_{X,\zeta}(\vec{r}), \tag{3.49}$$

where $W_p = \sqrt{|\vec{p}|^2 + m^2_{X_1}} + \sqrt{|\vec{p}|^2 + m^2_{X_2}}$ for $p = k, q$. The function $\eta_{\xi,\zeta}(\vec{k},\vec{q})$ is defined as

$$\eta_{\xi,\zeta}(\vec{k},\vec{q}) = \sum_{X} \int d^3r \; \psi^{\dagger\,(W_k)}_{X,\xi}(\vec{r}) \psi^{(W_q)}_{X,\zeta}(\vec{r}). \tag{3.50}$$

From Eqs. (3.49) and (3.50), we can see that the dual basis satisfies

$$\sum_{X} \int d^3r \; \tilde{\psi}^{(W_k)}_{X,\xi}(\vec{r}) \psi^{(W_q)}_{X,\zeta}(\vec{r}) \;\; = \;\; \delta_{\xi,\zeta}\delta^{(3)}(\vec{k}-\vec{q}). \tag{3.51}$$

We then define the non-local potential by using the dual basis and Eq. (3.47) as

$$U_{X,Y;\xi,\zeta}(\vec{r},\vec{r'}) \equiv \int d^3k \; K_{X,\xi}(\vec{r},\vec{k}) \tilde{\psi}^{(W_k)}_{Y,\zeta}(\vec{r'}), \tag{3.52}$$

where the non-local potential $U_{X,Y;\xi,\zeta}(\vec{r},\vec{r'})$ is energy-independent due to the integral of k in the right-hand side of Eq. (3.52). By using Eqs. (3.51) and (3.52), we finally obtain the following equation.

$$K_{X,\xi}(\vec{r},\vec{k}) = \left(|\vec{k}|^2 + \vec{\nabla}^2\right) \psi^{(W)}_{X,\xi}(\vec{r}) = \sum_{Y,\zeta} \int d^3r' U_{X,Y;\xi,\zeta}(\vec{r},\vec{r'}) \psi^{(W)}_{Y,\zeta}(\vec{r'}). \tag{3.53}$$

When we rescale the potential as $U = 2\mu_X \tilde{U}$ with a reduced mass $\mu_X = m_{X_1} m_{X_2}/(m_{X_1} + m_{X_2})$ and rewrite $\tilde{U} \to U$, the Eq. (3.53) can be written as the Schrödinger equation for non-local potential:

$$(E_X - H_{0,X}) \, \psi^{(W)}_{X,\xi}(\vec{r}) = \sum_{Y,\zeta} \int d^3r' U_{X,Y;\xi,\zeta}(\vec{r},\vec{r'}) \psi^{(W)}_{Y,\zeta}(\vec{r'}), \tag{3.54}$$

where $E_X = |\vec{k}_X|^2/(2\mu_X)$ and $H_{0,X} = -\vec{\nabla}^2/(2\mu_X)$. The important point here is that we don't need any non-relativistic approximations for the derivation of Eq. (3.54) and the relative momentum $\vec{k}_X$ is determined from the total energy $W = \sqrt{|\vec{k}_X|^2 + m_{X_1}} +$

$\sqrt{|\vec{k}_X|^2 + m_{X_2}}$. Furthermore, by construction in Eq. (3.54), the energy-independent non-local potentials defined from NBS wave functions reproduce the correct scattering amplitude below the new channel threshold.

We next consider the extraction of the leading order potentials of the derivative expansion for non-local potentials. For simplicity, we omit the spin indices in this discussion. To this end, we need two pairs of NBS wave functions which have different total energy, namely $\psi_X^{(W)}$ and $\psi_X^{(W')}$ ($W \neq W'$). Using Eq. (3.10), we can rewrite the Eq.(3.54) as a simple 2×2 matrix form:

$$\begin{pmatrix} \frac{K_{ab}(\vec{r},\vec{k})}{2\mu_{ab}} & \frac{K_{ab}(\vec{r},\vec{k'})}{2\mu_{ab}} \\ \frac{K_{cd}(\vec{r},\vec{k})}{2\mu_{cd}} & \frac{K_{cd}(\vec{r},\vec{k'})}{2\mu_{cd}} \end{pmatrix} = \begin{pmatrix} V_{ab,ab}(\vec{r}) & V_{ab,cd}(\vec{r}) \\ V_{cd,ab}(\vec{r}) & V_{cd,cd}(\vec{r}) \end{pmatrix} \begin{pmatrix} \psi_{ab}^{(W)}(\vec{r}) & \psi_{ab}^{(W')}(\vec{r}) \\ \psi_{cd}^{(W)}(\vec{r}) & \psi_{cd}^{(W')}(\vec{r}) \end{pmatrix}. \tag{3.55}$$

Thus the leading order potentials $V_{X,Y}$ can be extracted by solving the inverse problem of Eq. (3.55).

We now discuss the non-locality of the potential. As shown in this section (see also Sec. 3.1.1), the non-local potential is defined as energy-independent until the new threshold opens. The local potential, however, may be energy-dependent below the inelastic threshold because the non-locality of the potential becomes larger as the total energy W approaches the inelastic threshold. In order to see the non-locality of the potential, let us consider an effective potential for a channel $[ab]$ from coupled channel potentials. Assuming the coupled channel potentials $U_{X,Y}(\vec{r},\vec{r'})$ can be approximated as the local potential $V_{X,Y}(\vec{r})\delta^{(3)}(\vec{r}-\vec{r'})$, we define the effective potential for the channel $[ab]$:

$$U_{ab}^{\text{eff}}(\vec{r},\vec{r'}) = V_{ab,ab}(\vec{r})\delta^{(3)}(\vec{r}-\vec{r'}) + V_{ab,cd}(\vec{r})\frac{1}{E_{cd} - H_{0,cd} - V_{cd,cd}}(\vec{r},\vec{r'})V_{cd,ab}(\vec{r'}), \tag{3.56}$$

where the non-locality of the effective potential comes from the second term. In order to estimate the magnitude of non-locality, we omit the $V_{cd,cd}$ in Eq. (3.56) for simplicity. When the total energy W is below the inelastic threshold (i.e. $m_a + m_b < W < m_c + m_d$), we have

$$\frac{1}{E_{cd} - H_{0,cd}}(\vec{r},\vec{r'}) = \frac{2\mu_{cd}}{4\pi|\vec{r}-\vec{r'}|}e^{-q|\vec{r}-\vec{r'}|}, \tag{3.57}$$

where $q^2 = -|\vec{k}_{cd}|^2$. Therefore, the non-locality caused by channel couplings is exponen-

tially suppressed as long as the q is sufficiently large. However, if the q becomes small (which is equivalent that the total energy W approaches the inelastic threshold from below), the non-locality of the effective potential becomes large. Note that larger transition potentials $V_{ab,cd}, V_{cd,ab}$ also make the non-locality larger. In practical calculations, we have to remember this observation when the scattering energies are close to the inelastic threshold. In such a case, we can check the non-locality of the potential by comparing the coupled channel potential with the single channel potential.

3.2.2 Extraction of the coupled channel potentials on the lattice

In the previous section, we define the coupled channel Schrödinger equation for non-local potentials and we show that one needs two sets of NBS wave functions with different total energy, namely $\psi_X^{(W)}$ $(X = ab, cd)$ and $\psi_X^{(W')}$ with $W \neq W'$. In a finite volume, $|ab; W\rangle$ and $|cd; W\rangle$ in Eq. (3.44) are no longer energy eigenstates of the Hamiltonian. These energy eigenvalues are shifted from W to $W + \mathcal{O}(L^{-2})$ with L being the spacial extension. Under this circumstance, we can obtain the two sets of NBS wave functions as follows. First, we prepare two source operators defined by

$$\mathcal{J}_{ab}(t_0) = \overline{B_a(t_0)B_b(t_0)}, \tag{3.58}$$

$$\mathcal{J}_{cd}(t_0) = \overline{B_c(t_0)B_d(t_0)}, \tag{3.59}$$

which create eigenstates on the lattice as

$$\mathcal{J}_{ab}(t_0)|0\rangle = C_a|B = 2; W_0\rangle + C_b|B = 2; W_1\rangle + \cdots, \tag{3.60}$$

$$\mathcal{J}_{cd}(t_0)|0\rangle = C_c|B = 2; W_0\rangle + C_d|B = 2; W_1\rangle + \cdots, \tag{3.61}$$

where C_i $(i = a, b, c, d)$ is arbitrary constant. The state $|B = 2; W_n\rangle$ stands for the n-th energy eigenstate with the energy W_n. The constants C_i can be determined from baryon two-point correlation functions by diagonalization method in lattice QCD simulations. Using C_i, we next define optimized source operators as

$$\begin{pmatrix} \mathcal{J}_{W_1}(t_0) \\ \mathcal{J}_{W_2}(t_0) \end{pmatrix} = \begin{pmatrix} C_a & C_b \\ C_c & C_d \end{pmatrix}^{-1} \begin{pmatrix} \mathcal{J}_{ab}(t_0) \\ \mathcal{J}_{cd}(t_0) \end{pmatrix}, \tag{3.62}$$

where $\mathcal{J}_{W_n}(t_0)$ $(n = 0, 1)$ creates the states as

$$\mathcal{J}_{W_1}(t_0)|0\rangle = |B = 2; W_0\rangle + \cdots , \tag{3.63}$$

$$\mathcal{J}_{W_2}(t_0)|0\rangle = |B = 2; W_1\rangle + \cdots . \tag{3.64}$$

Finally, we extract the NBS wave functions from baryon four-point correlation functions at large $t - t_0$, as shown in Sec. 3.1.3.

$$\begin{aligned} G_{ab}^{\mathcal{J}_{W_n}}(\vec{r}, t - t_0) &= \sum_{\vec{x}} \langle 0|B_a(\vec{r} + \vec{x}, t)B_b(\vec{x}, t)\mathcal{J}_{W_n}(t_0)|0\rangle \\ &\to \sqrt{Z_a}\sqrt{Z_b}\ \psi_{ab}^{(W_n)}(\vec{r})e^{-W_n(t-t_0)} + \mathcal{O}(e^{-W_2(t-t_0)}), \end{aligned} \tag{3.65}$$

$$\begin{aligned} G_{cd}^{\mathcal{J}_{W_n}}(\vec{r}, t - t_0) &= \sum_{\vec{x}} \langle 0|B_c(\vec{r} + \vec{x}, t)B_d(\vec{x}, t)\mathcal{J}_{W_n}(t_0)|0\rangle \\ &\to \sqrt{Z_c}\sqrt{Z_d}\ \psi_{cd}^{(W_n)}(\vec{r})e^{-W_n(t-t_0)} + \mathcal{O}(e^{-W_2(t-t_0)}), \end{aligned} \tag{3.66}$$

where $n = 0, 1$.

From those baryon four-point correlation functions, the leading order of the derivative expansion for coupled channel potentials (Eq. (3.55)) can be derived:

$$\begin{aligned} &\begin{pmatrix} V_{ab,ab}(\vec{r}) & V_{ab,cd}(\vec{r}) \\ V_{cd,ab}(\vec{r}) & V_{cd,cd}(\vec{r}) \end{pmatrix} \\ = &\begin{pmatrix} \sqrt{Z_a}\sqrt{Z_b} & 0 \\ 0 & \sqrt{Z_c}\sqrt{Z_d} \end{pmatrix}^{-1} \\ \times &\begin{pmatrix} \left(E_{ab}^{(W_0)} - (H_0)_{ab}\right) G_{ab}^{\mathcal{J}_{W_0}}(\vec{r}, t - t_0) & \left(E_{ab}^{(W_1)} - (H_0)_{ab}\right) G_{ab}^{\mathcal{J}_{W_1}}(\vec{r}, t - t_0) \\ \left(E_{cd}^{(W_0)} - (H_0)_{cd}\right) G_{cd}^{\mathcal{J}_{W_0}}(\vec{r}, t - t_0) & \left(E_{cd}^{(W_1)} - (H_0)_{cd}\right) G_{cd}^{\mathcal{J}_{W_1}}(\vec{r}, t - t_0) \end{pmatrix} \\ \times &\begin{pmatrix} G_{ab}^{\mathcal{J}_{W_0}}(\vec{r}, t - t_0) & G_{ab}^{\mathcal{J}_{W_1}}(\vec{r}, t - t_0) \\ G_{cd}^{\mathcal{J}_{W_0}}(\vec{r}, t - t_0) & G_{cd}^{\mathcal{J}_{W_1}}(\vec{r}, t - t_0) \end{pmatrix}^{-1} \begin{pmatrix} \sqrt{Z_a}\sqrt{Z_b} & 0 \\ 0 & \sqrt{Z_c}\sqrt{Z_d} \end{pmatrix}, \end{aligned} \tag{3.67}$$

for sufficiently large $t - t_0$ where contributions from states with the total energies $W \geq W_2$ can be negligible. Here $(H_0)_X$ is defined as $(H_0)_X = \vec{\nabla}^2/(2\mu_X)$ with the reduced mass for channel X, and $E_X^{(W_n)}$ is defined as $E_X^{(W_n)} = |(\vec{k}_X)_n|^2/(2\mu_X)$, where the discrete relative momentum $(\vec{k}_X)_n$ for channel X is determined from W_n. Z-factors in Eq. (3.67)

can be calculated from the baryon two-point correlation function, as we will explain in Appendix C.

3.2.3 Time-dependent HAL QCD method for coupled channel potentials

In practical lattice QCD calculation, we have a difficulty to obtain the ground state NBS wave function due to large statistical noise at large $t - t_0$, as we discussed in Sec. 3.1.3. We then explained an improved method to extract the potential without the ground state domination of the NBS wave function in Sec. 3.1.4 for an elastic scattering case, namely the time-dependent HAL QCD method. The time-dependent HAL QCD method can be extended straightforwardly to the case of inelastic scatterings. In this subsection, we present the coupled channel formalism of the time-dependent HAL QCD method.

Let us start from the normalized baryon four-point correlation function R in channel X defined as

$$\begin{aligned} R_X^{\mathcal{J}_Y}(\vec{r}, t - t_0) &\equiv \frac{G_X^{\mathcal{J}_Y}(\vec{r}, t - t_0)}{e^{-m_{B_{X_1}}(t-t_0)} e^{-m_{B_{X_2}}(t-t_0)}} \\ &= \sum_n \sqrt{Z_{X_1}} \sqrt{Z_{X_2}}\, \psi_X^{(W_n)}(\vec{r}) e^{-\Delta W_n^X (t-t_0)} A_n^{\mathcal{J}_Y} + \cdots , \end{aligned} \tag{3.68}$$

where $m_{B_{X_i}}$ $(i = 1, 2)$ is a baryon mass in channel X, the ΔW_n^X is defined as $\Delta W_n^X = W_n - (m_{B_{X_1}} + m_{B_{X_2}})$, and $A_n^{\mathcal{J}_Y} = \langle W_n | \mathcal{J}_Y(0) | 0 \rangle$. The baryon four-point correlation functions are defined using original source operator $\mathcal{J}_Y$ $(Y = ab, cd)$ instead of $\mathcal{J}_{W_n}$ (i.e., one doesn't need the diagonalization of source operators). The ellipses in Eq. (3.68) denote inelastic contributions coming from channels above the channel X.

In the case of $m_{B_{X_1}} = m_{B_{X_2}} \equiv m_X$, the ΔW_n^X satisfies

$$\frac{k_n^2}{m_X} = \Delta W_n^X + \frac{1}{4m_X} \left(\Delta W_n^X \right)^2 . \tag{3.69}$$

Using above relation and Eq. (3.52), we obtain the time-dependent coupled channel Schödinger equation for R-correlator:

$$\left[-\frac{\partial}{\partial t} + \frac{1}{4m} \frac{\partial^2}{\partial t^2} - (H_0)_X \right] R_X^{\mathcal{J}_Y}(\vec{r}, t - t_0)$$

$$
\begin{aligned}
&= \sum_n \sqrt{Z_{X_1}}\sqrt{Z_{X_2}} \left[-\frac{\partial}{\partial t} + \frac{1}{4m}\frac{\partial^2}{\partial t^2} - (H_0)_X \right] \psi_X^{(W_n)}(\vec{r}) e^{-\Delta W_n^X (t-t_0)} A_n^{\mathcal{J}_Y} \\
&= \sum_n \sqrt{Z_{X_1}}\sqrt{Z_{X_2}} \left[\Delta W_n + \frac{1}{4m}(\Delta W_n)^2 - (H_0)_X \right] \psi_X^{(W_n)}(\vec{r}) e^{-\Delta W_n^X (t-t_0)} A_n^{\mathcal{J}_Y} \\
&= \sum_n \sqrt{Z_{X_1}}\sqrt{Z_{X_2}} \left[E_X^{(W_n)} - (H_0)_X \right] \psi_X^{(W_n)}(\vec{r}) e^{-\Delta W_n^X (t-t_0)} A_n^{\mathcal{J}_Y} \\
&= \sum_n \sqrt{Z_{X_1}}\sqrt{Z_{X_2}} \left[\sum_{X'=ab,cd} \int d^3r' U_{X,X'}(\vec{r},\vec{r'}) \psi_{X'}^{(W_n)}(\vec{r'}) \right] e^{-\Delta W_n^X (t-t_0)} A_n^{\mathcal{J}_Y} \\
&= \sum_{X'=ab,cd} \int d^3r' \ \Delta_{X,X'} \ U_{X,X'}(\vec{r},\vec{r'}) R_{X'}^{\mathcal{J}_Y}(\vec{r'}, t-t_0), \qquad (3.70)
\end{aligned}
$$

for moderately large $t - t_0$ where inelastic contributions from channels other than the $[ab]$ and the $[cd]$ can be neglected. A factor $\Delta_{X,X'}$ in Eq. (3.70) is defined by

$$
\Delta_{X,X'} = \frac{\sqrt{Z_{X_1}}\sqrt{Z_{X_2}} e^{-(m_{B_{X_1'}} + m_{B_{X_2'}})(t-t_0)}}{\sqrt{Z_{X_1'}}\sqrt{Z_{X_2'}} e^{-(m_{B_{X_1}} + m_{B_{X_2}})(t-t_0)}}. \qquad (3.71)
$$

In the case of $m_{B_{X_1}} \neq m_{B_{X_2}}$, as shown in Sec. 3.1.4, the R-correlators satisfy

$$
\begin{aligned}
&\left[\left(\frac{1+3\delta_X^2}{8\mu_X} \right) \frac{\partial^2}{\partial t^2} - \frac{\partial}{\partial t} - (H_0)_X \right] R_X^{\mathcal{J}_Y}(\vec{r}, t-t_0) \\
&= \sum_{X'=ab,cd} \int d^3r' \ \Delta_{X,X'} \ U_{X,X'}(\vec{r},\vec{r'}) R_{X'}^{\mathcal{J}_Y}(\vec{r'}, t-t_0), \qquad (3.72)
\end{aligned}
$$

up to $\mathcal{O}\left((\Delta W_n)^2\right)$, where $\delta_X = (m_{B_{X_1}} - m_{B_{X_2}})/(m_{B_{X_1}} + m_{B_{X_2}})$.

Chapter 4

Partial wave decomposition on the lattice

As we reviewed in the previous chapter, we can define non-local energy-independent potential from NBS wave functions through the Schrödinger equation by the HAL QCD method. In practice, we have to calculate the potential in the desired spin-isospin channel to see the interaction of the corresponding system. This potential is constructed from the spin-isospin projected NBS wave function as we presented in Sec. 3.1.5. At this time, we employ the cubic transformation group for projection to the orbital angular momentum $L = 0$ (Eq. (3.34)) on the lattice because the spherical surface integral cannot be carried out on the discrete space. This projection picks up an A_1^+ representation of $SO(3, Z)$ group, which contains not only $L = 0$ component but also the higher components with $L \geq 4$ [48]. If the $L \geq 4$ components of the NBS wave function are completely zero, the NBS wave function (and also the potential) should be isotropic. We often observe, however, the comb-like structures in the potential on the radial coordinate (e.g. see Fig. 2 in Ref. [53]) which represent the anisotropy of the potential. This observation implies that the $L \geq 4$ components remain in the NBS wave functions and contaminate the potential. In order to construct more robust potential, removing the $L \geq 4$ components from the NBS wave function is mandatory. In this chapter, we propose three methods to remove the $L \geq 4$ components from the NBS wave function. From Sec. 4.1 to Sec. 4.3, we present the method section by section. Throughout this chapter, we write the NBS

wave function as $\psi(\vec{x})$ with $\vec{x} = (x, y, z)$ or (r, θ, ϕ)[1] , which is expanded in term of the spherical harmonics $Y_{lm}(\theta, \phi)$ as

$$\psi(\vec{x}) = \sum_{l=0}^{\infty} \sum_{m=-l}^{l} g_{lm}(r) Y_{lm}(\theta, \phi), \tag{4.1}$$

where $g_{lm}(r)$ represents a radial function for an (l, m) component [2]. Also, we assume that the lattice spacing is scaled to unity.

4.1 r-binning method

Let us consider the extraction $g_{00}(r)$ for given $r = R$ from the NBS wave function. In the continuum space, we can get $g_{00}(R)$ by taking the spherical surface integral at $r = R$ as

$$g_{00}(R) = \int_S d\Omega \; Y_{00}^*(\theta, \phi) \psi(\vec{x}; r = R), \tag{4.2}$$

because of the orthogonality of the spherical harmonics,

$$\int_S d\Omega \; Y_{lm}^*(\theta, \phi) Y_{l'm'}(\theta, \phi) = \delta_{ll'} \delta_{mm'}. \tag{4.3}$$

In the discrete space, the spherical surface integrals in Eqs. (4.2) and (4.3) are replaced by the average of the lattice data located on $\{\vec{x} | r = R\}$ as

$$\frac{1}{4\pi} \int_S d\Omega \implies \frac{1}{N_p} \sum_{\vec{x} \in \{\vec{x} | r = R\}}, \tag{4.4}$$

with a number of data points N_p, where the orthogonality of the spherical harmonics does not hold completely.

In order to retain the orthogonality approximately, we propose the binning method

[1] The relation between the coordinates (x, y, z) and (r, θ, ϕ) is defined as

$$\begin{aligned} x &= r \sin\theta \cos\phi \\ y &= r \sin\theta \sin\phi \\ z &= r \cos\theta. \end{aligned}$$

[2] We often call it "Spherical harmonics amplitude".

of the radial coordinate for the NBS wave functions. We consider a spherical shell $S_{R,\Delta}$ with thickness Δ surrounding the sphere surface $r = R$ defined by

$$S_{R,\Delta} \equiv \{\vec{x} | R - \Delta \leq r \leq R + \Delta\}, \tag{4.5}$$

and define a radial binned NBS wave function $\psi_{\rm rbin}(R)$ by the average of the data in $S_{R,\Delta}$ as

$$\psi_{\rm rbin}(R) \equiv \frac{\sqrt{4\pi}}{N_{\rm rbin}} \sum_{\vec{x} \in S_{R,\Delta}} \psi(\vec{x}), \tag{4.6}$$

where $N_{\rm rbin}$ stands for a number of all data points in $S_{R,\Delta}$. Here $\psi_{\rm rbin}(R)$ corresponds to $g_{00}(R)$. In this approach, compared to Eq. (4.4), possible angle to use for average the NBS wave function increases and the average value is approximated to the spherical surface integral. It should be noted that fluctuation of $g_{00}(r)$ in $R - \Delta \leq r \leq R + \Delta$ is must be small, otherwise the average in Eq. (4.6) hides the detailed structure of the $g_{00}(r)$. The advantage point of this approach is that the numerical cost is small so that it can easily be applied to large scale data.

4.2 Decomposition from A_1^+ projected data in fixed r

In this subsection, we propose an alternative method to extract $g_{00}(R)$ from the NBS wave function. We here use the A_1^+ projected NBS wave function defined by

$$\begin{aligned} \psi^{A_1^+}(\vec{x}) &\equiv P^{A_1^+} \psi(\vec{x}) \\ &= Y_{00}^{A_1^+}(\theta, \phi) g_{00}(r) + \sum_{m=0,\pm 4} Y_{4m}^{A_1^+}(\theta, \phi) g_{4m}(r) + \cdots, \end{aligned} \tag{4.7}$$

where $P^{A_1^+}$ is the projection operator into A_1^+ representation defined in Eq. (3.34), $Y_{00}^{A_1^+}(\theta, \phi)$ and $Y_{4m}^{A_1^+}(\theta, \phi)$ stand for the A_1^+ projected spherical harmonics, and the ellipses show the higher angular momentum components such as $L = 6, 8$. $L =$ odd integer and $L = 2$ components are removed by the A_1^+ projection. Since the property of the rotation transformation, the spherical harmonics $Y_{4m}(\theta, \phi)$ with $m = \pm 1, \pm 2$ and ± 3 are also removed while the components with $m = 0, \pm 4$ remain non-zero values. The definitions of $Y_{00}^{A_1^+}(\theta, \phi)$ and

$Y_{4m}^{A_1^+}(\theta,\phi)$ in the orthogonal coordinate system are as follows:

$$Y_{00}^{A_1^+}(x,y,z) = Y_{00}(x,y,z) = \frac{1}{\sqrt{4\pi}} \tag{4.8}$$

$$Y_{40}^{A_1^+}(x,y,z) = \frac{7}{8\sqrt{\pi}} \frac{x^4+y^4+z^4-3(x^2y^2+y^2z^2+z^2x^2)}{r^4} \tag{4.9}$$

$$Y_{4,+4}^{A_1^+}(x,y,z) = Y_{4,-4}^{A_1^+}(x,y,z) = \sqrt{\frac{5}{14}} Y_{40}^{A_1^+}(x,y,z). \tag{4.10}$$

Since $Y_{40}^{A_1^+}$ (also $Y_{4,\pm4}^{A_1^+}$) has an angular dependence, the NBS wave function at given $r = R$ has multi-values, which make comb-like structures in the potential on the radial coordinate. Let us consider there are N points of the A_1^+ projected NBS wave function $\{\psi^{A_1^+}(\vec{x_i})\}$ $(i = 1, \cdots, N)$ for $|\vec{x_i}| = R$ which have different values each other. Neglecting the components of $L \geq 6$, each NBS wave function is written as

$$\begin{aligned} \psi^{A_1^+}(\vec{x_i}) &= Y_{00}^{A_1^+} g_{00}(r) + \sum_{m=0,\pm4} Y_{4m}^{A_1^+}(\vec{x}_i) g_{4m}(r), \\ &\equiv Y_{00}^{A_1^+} g_{00}(r) + Y_4^{A_1^+}(\vec{x}_i) g_4(r), \end{aligned} \tag{4.11}$$

where we omit the arguments for $Y_{00}^{A_1^+}$ since it is just a constant, and we write together the $L = 4$ components because $Y_{40}^{A_1^+}(\vec{x})$ and $Y_{4,\pm4}^{A_1^+}(\vec{x})$ have the same angular dependence. Eq. (4.11) can be rewritten using the matrix form as

$$\begin{pmatrix} \psi^{A_1^+}(\vec{x}_1) \\ \vdots \\ \psi^{A_1^+}(\vec{x}_N) \end{pmatrix} = \begin{pmatrix} Y_{00}^{A_1^+} & Y_4^{A_1^+}(\vec{x}_1) \\ \vdots & \vdots \\ Y_{00}^{A_1^+} & Y_4^{A_1^+}(\vec{x}_N) \end{pmatrix} \begin{pmatrix} g_{00}(r) \\ g_4(r) \end{pmatrix}, \tag{4.12}$$

where the matrix in the right-hand side is an $N \times 2$ rectangle matrix. When $N \geq 2$, we can solve the Eq. (4.12) by using the Singular Value Decomposition (SVD) for the rectangle matrix. When we write the SVD for an $M \times N$ $(M > N)$ rectangle matrix A as $A = U\Sigma V^\dagger$ with unitary matrixes U, V and a diagonal matrix for the singular values Σ, the generalized inverse matrix is defined as $A^{-1} = V\Sigma^{-1}U^\dagger$, where Σ and Σ^{-1} are defined by

$$\Sigma \equiv \begin{pmatrix} \mathrm{diag}(\sigma_1, \cdots, \sigma_N) \\ \mathbf{0}_{(M-N)\times N} \end{pmatrix} \tag{4.13}$$

$$\Sigma^{-1} \equiv \left(\mathrm{diag}(\sigma_1^{-1}, \cdots, \sigma_N^{-1}) \quad \mathbf{0}_{N\times(M-N)} \right), \tag{4.14}$$

where $\mathbf{0}_{M\times N}$ represents the $M \times N$ zero matrix[3]. Note that the SVD corresponds to the Eigen Value Decomposition (EVD) for the square matrix.

Advantages of this approach are as follows. First, we can obtain the radial function not only for $L = 0$ component but also for $L = 4$ component. By comparing these components, we can see the magnitude of $L = 4$ contamination in the NBS wave function. Second, the extraction of higher angular momentum components is easily applicable. Including the $L = 6$ component, for instance, we can extract the radial functions for $L = 0, 4$, and 6 by solving the equation

$$\begin{pmatrix} \psi^{A_1^+}(\vec{x}_1) \\ \vdots \\ \psi^{A_1^+}(\vec{x}_N) \end{pmatrix} = \begin{pmatrix} Y_{00}^{A_1^+} & Y_4^{A_1^+}(\vec{x}_1) & Y_6^{A_1^+}(\vec{x}_1) \\ \vdots & \vdots & \vdots \\ Y_{00}^{A_1^+} & Y_4^{A_1^+}(\vec{x}_N) & Y_6^{A_1^+}(\vec{x}_N) \end{pmatrix} \begin{pmatrix} g_{00}(r) \\ g_4(r) \\ g_6(r) \end{pmatrix}, \tag{4.15}$$

where the matrix in the right-hand side is an $N \times 3$ rectangle matrix. Note that we need at least 3 points of the NBS wave function at given $|\vec{x}_i| = R$ which are not related by A_1^+ projection.

We next consider the extraction of the Laplacian for the radial function such as $g_{00}(r)$ in order to construct the potentials. When we neglecting the components of $L \geq 6$ again, the Laplacian of the NBS wave function (Eq. (4.11)) is shown as

$$\vec{\nabla}^2 \psi^{A_1^+}(\vec{x}_i) = Y_{00}^{A_1^+} \vec{\nabla}^2 g_{00}(r) + \vec{\nabla}^2 \left[Y_4^{A_1^+}(\vec{x}_i) g_4(r) \right]. \tag{4.16}$$

where the second term can be calculated in the continuum space as

$$\vec{\nabla}^2 \left[Y_4^{A_1^+}(\vec{x}_i) g_4(r) \right] = Y_4^{A_1^+}(\vec{x}_i) \left[\vec{\nabla}^2 - \frac{4(4+1)}{r^2} \right] g_4(r). \tag{4.17}$$

[3]We assume here that all singular values have a non-zero value, otherwise the generalized inverse matrix cannot be defined.

Using Eqs. (4.11) and (4.16), we have

$$\begin{pmatrix} \psi^{A_1^+}(\vec{x}_1) \\ \vec{\nabla}^2\psi^{A_1^+}(\vec{x}_1) \\ \vdots \\ \psi^{A_1^+}(\vec{x}_N) \\ \vec{\nabla}^2\psi^{A_1^+}(\vec{x}_N) \end{pmatrix} = \begin{pmatrix} Y_{00}^{A_1^+} & 0 & Y_4^{A_1^+}(\vec{x}_1) & 0 \\ 0 & Y_{00}^{A_1^+} & -\frac{4(4+1)}{r^2} & Y_4^{A_1^+}(\vec{x}_1) \\ \vdots & \vdots & \vdots & \vdots \\ Y_{00}^{A_1^+} & 0 & Y_4^{A_1^+}(\vec{x}_N) & 0 \\ 0 & Y_{00}^{A_1^+} & -\frac{4(4+1)}{r^2} & Y_4^{A_1^+}(\vec{x}_N) \end{pmatrix} \begin{pmatrix} g_{00}(r) \\ \vec{\nabla}^2 g_{00}(r) \\ g_4(r) \\ \vec{\nabla}^2 g_4(r) \end{pmatrix}, \quad (4.18)$$

which can be solved by SVD. Note that the Eq. (4.17) has $\mathcal{O}(a^n)$ $(n > 1)$ discretized errors in a discrete space.

4.3 Misner's method

In this subsection, we present a method to get spherical harmonics amplitudes proposed by C. W. Misner [54], which has been employed for extracting gravitational waveforms from simulations of radiating systems. The idea of this method is similar to the r-binning method we propose in Sec. 4.1, that is the spherical harmonics amplitude is calculated from the NBS wave function data in a spherical shell $S_{R,\Delta}$ by using the orthogonality of the spherical harmonics. He employs, however, not only the spherical harmonics but also orthonormal basis functions in the radial coordinate $G_n^{R,\Delta}(r)$ $(n = 0, \cdots, \infty)$ which are orthonormal with respect to integration over the radial interval $[R-\Delta, R+\Delta]$, as

$$\int_{R-\Delta}^{R+\Delta} dr\ r^2\ \overline{G_n^{R,\Delta}(r)} G_m^{R,\Delta}(r) = \delta_{nm}, \quad (4.19)$$

where the overline represents the complex conjugate. One of the candidates for $G_n^{R,\Delta}(r)$ is given by

$$G_n^{R,\Delta}(r) = \frac{1}{r}\sqrt{\frac{2n+1}{2\Delta}} P_n\left(\frac{r-R}{\Delta}\right), \quad (4.20)$$

where $P_n(r)$ is the Legendre polynomial, which obviously satisfies Eq. (4.19).

Let us consider the extraction $g_{lm}(R)$ for given $r = R$ from the NBS wave function (Eq. (4.1)) in the continuum space. Here we introduce orthonormal basis functions

$\mathcal{Y}^{R,\Delta}_{nlm}(r,\theta,\phi) \equiv G^{R,\Delta}_{n}(r)Y_{lm}(\theta,\phi)$ which obey

$$\int_{S_{R,\Delta}} d^3x \ \overline{\mathcal{Y}^{R,\Delta}_{nlm}(r,\theta,\phi)}\mathcal{Y}^{R,\Delta}_{n'l'm'}(r,\theta,\phi) = \delta_{nn'}\delta_{ll'}\delta_{mm'}, \tag{4.21}$$

where the integral over $S_{R,\Delta}$ is defined as

$$\int_{S_{R,\Delta}} d^3x = \int_{R-\Delta}^{R+\Delta} dr \int_S d\Omega. \tag{4.22}$$

Using the orthonormal basis functions, the NBS wave function is expanded by

$$\psi(\vec{x}) = \sum_{n=0}^{\infty}\sum_{l=0}^{\infty}\sum_{m=-l}^{l} c^{R,\Delta}_{nlm}\ \mathcal{Y}^{R,\Delta}_{nlm}(r,\theta,\phi), \tag{4.23}$$

in a spherical shell $S_{R,\Delta}$ with coefficients $c^{R,\Delta}_{nlm}$. From the definitions in Eqs. (4.21) and (4.23), we can get the coefficients $c^{R,\Delta}_{nlm}$ as

$$c^{R,\Delta}_{nlm} = \int_{S_{R,\Delta}} d^3x \ \overline{\mathcal{Y}^{R,\Delta}_{nlm}(r,\theta,\phi)}\ \psi(\vec{x}), \tag{4.24}$$

and spherical harmonics amplitude $g_{lm}(R)$ can be given by

$$g_{lm}(R) = \sum_{n=0}^{\infty} c^{R,\Delta}_{nlm}\ G^{R,\Delta}_{n}(R). \tag{4.25}$$

One of the advantages in this method is that Eq. (4.24) is defined as a volume integral which can be simply replaced by the sum of a unit cube on the lattice. In a discrete space, the volume integral is rewritten by

$$\int_{S_{R,\Delta}} d^3x \implies \sum_{\vec{x}} \omega^{R,\Delta}(\vec{x}), \tag{4.26}$$

where $\omega^{R,\Delta}(\vec{x})$ stands for a weight which corresponds to overlap between the shell $S_{R,\Delta}$ and a unit cube around the point $\vec{x}$. If the unit cube lies entirely inside the shell $S_{R,\Delta}$, the weight is given by $\omega^{R,\Delta}(\vec{x}) = a^3$ with a lattice spacing a, while $\omega^{R,\Delta}(\vec{x}) = 0$ when the unit cube lies entirely outside the shell. For other points, however, the overlap is complicated and difficult to calculate. In Ref. [54], the author has used following simple definition for

the weight:

$$\omega^{R,\Delta}(\vec{x}) = \begin{cases} a^3 & \text{for } |r-R| < \Delta - \frac{1}{2}a \\ 0 & \text{for } |r-R| > \Delta + \frac{1}{2}a \\ a^2\left(\Delta + \frac{1}{2}a - |R-r|\right) & \text{otherwise} \end{cases}, \tag{4.27}$$

which corresponds to the overlap of a unit cube parallel to the axis in the radial direction.

Here we define an inner product of functions $f(\vec{x})$ and $g(\vec{x})$ in the shell $S_{R,\Delta}$ for both continuum and discrete spaces as

$$\langle f|g\rangle^{\rm cont}_{S_{R,\Delta}} = \int_{S_{R,\Delta}} d^3x\ \overline{f(\vec{x})}\ g(\vec{x}) \tag{4.28}$$

$$\langle f|g\rangle^{\rm disc}_{S_{R,\Delta}} = \sum_{\vec{x}} \omega^{R,\Delta}(\vec{x})\ \overline{f(\vec{x})}\ g(\vec{x}). \tag{4.29}$$

In these notations, Eqs. (4.21) and (4.24) are simply rewritten by

$$\langle \mathcal{Y}^{R,\Delta}_A|\mathcal{Y}^{R,\Delta}_B\rangle^{\rm cont}_{S_{R,\Delta}} = \delta_{AB} \tag{4.30}$$

$$\langle \mathcal{Y}^{R,\Delta}_A|\psi\rangle^{\rm cont}_{S_{R,\Delta}} = c^{R,\Delta}_A, \tag{4.31}$$

where $A, B \equiv (n,l,m)$. Since the basis functions $\mathcal{Y}^{R,\Delta}_A$ are not orthonormal in the discrete space, however, a hermitian matrix defined as $\mathcal{G}_{AB} \equiv \langle \mathcal{Y}^{R,\Delta}_A|\mathcal{Y}^{R,\Delta}_B\rangle^{\rm disc}_{S_{R,\Delta}}$ is no longer unit matrix. In this case, the coefficients $c^{R,\Delta}_{nlm}$ can be determined only approximately. In order to overcome this problem, one can define the following dual basis functions $\tilde{\mathcal{Y}}^{R,\Delta}_A$ using the inverse of matrix $\mathcal{G}_{AB}$:

$$\tilde{\mathcal{Y}}^{R,\Delta}_A(\vec{x}) \equiv \sum_B \mathcal{Y}^{R,\Delta}_B(\vec{x})\ \mathcal{G}^{-1}_{BA}, \tag{4.32}$$

where the index B runs over a finite set of (n,l,m), which satisfy

$$\langle \tilde{\mathcal{Y}}^{R,\Delta}_A|\mathcal{Y}^{R,\Delta}_B\rangle^{\rm disc}_{S_{R,\Delta}} = \sum_C \mathcal{G}^{-1}_{AC}\langle \mathcal{Y}^{R,\Delta}_C|\mathcal{Y}^{R,\Delta}_B\rangle^{\rm cont}_{S_{R,\Delta}} = \sum_C \mathcal{G}^{-1}_{AC}\mathcal{G}_{CB} = \delta_{AB} \tag{4.33}$$

$$\langle \tilde{\mathcal{Y}}^{R,\Delta}_A|\psi\rangle^{\rm disc}_{S_{R,\Delta}} \sim c^{R,\Delta}_A. \tag{4.34}$$

Once we obtain the coefficients $c^{R,\Delta}_A$, the spherical harmonics amplitude $g_{lm}(R)$ can be calculated from Eq. (4.25). We note that when we consider only $n_{\rm max} = l_{\rm max} = 0$ and

define the basis function in the radial coordinate and the weight function as

$$\begin{aligned} G_0^{R,\Delta}(r) &= \text{constant} \\ \omega^{R,\Delta}(\vec{x}) &= \begin{cases} a^3 & \text{for } \vec{x} \in S_{R,\Delta} \\ 0 & \text{otherwise} \end{cases}, \end{aligned} \tag{4.35}$$

one can find that the method is equivalent to the r-binning method proposed in Sec. 4.1.

We next consider the calculation of the Laplacian for the spherical harmonics amplitude $g_{lm}(r)$ which will be used for calculating potentials in the HAL QCD method. In a conventional way, we define the Laplacian for lattice data as a second-order finite differential which has some discretization errors. In Misner's method, however, we can estimate the Laplacian for $g_{lm}(r)$ in analytically. For example, when the orthonormal basis functions in the radial coordinate are given by Eq. (4.20), we have

$$\begin{aligned} \vec{\nabla}^2 g_{lm}(r) &= \frac{1}{r}\frac{\partial^2}{\partial r^2}\left[r g_{lm}(r)\right] \\ &= \sum_{n=0}^{\infty} c_{nlm}^{R,\Delta}\, \frac{1}{r}\frac{\partial^2}{\partial r^2}\left[r G_n^{R,\Delta}(r)\right] \\ &= \frac{1}{r}\sum_{n=0}^{\infty} c_{nlm}^{R,\Delta}\, \frac{\partial^2}{\partial r^2}\left[\sqrt{\frac{2n+1}{2\Delta}} P_n\left(\frac{r-R}{\Delta}\right)\right] \\ &= \frac{1}{r\Delta^2}\sqrt{\frac{2n+1}{2\Delta}} \sum_{n=0}^{\infty} c_{nlm}^{R,\Delta}\, P_n''\left(\frac{r-R}{\Delta}\right), \end{aligned} \tag{4.36}$$

where P_n'' shows the second-order derivative for the Legendre polynomial.

Before finishing this subsection, we present some comments for applying this method to lattice QCD data. First, we cannot calculate the dual orthonormal function with all of the set of (n, l, m), so that the Eq. (4.34) is approximate. In this case, as we discuss in the next subsection, the mean square error between $\langle \tilde{\mathcal{Y}}_A^{R,\Delta} | \psi \rangle_{S_{R,\Delta}}^{\text{disc}}$ and $c_A^{R,\Delta}$ is minimized by the dual basis function

$$\tilde{\mathcal{Y}}_{nlm}^{R,\Delta}(\vec{x}) \equiv \sum_{n'=0}^{n_{\max}} \sum_{l'=0}^{l_{\max}} \sum_{m'=-l}^{l} \mathcal{Y}_{n'l'm'}^{R,\Delta}(\vec{x})\, \mathcal{G}^{-1}_{n'l'm',nlm}, \tag{4.37}$$

for given $n_{\max}$ and $l_{\max}$. These parameters are determined from a balance between reproducibility of NBS wave functions and numerical instability. If the variation of the NBS wave function in the radial coordinate is large, for instance, one should increase $n_{\max}$ to

reproduce correct spherical harmonics amplitude $g_{lm}(r)$, while the inverse of the matrix $\mathcal{G}_{AB}$ may cause numerical instability due to its small determinant[4]. Second, the most costly calculation in practice is the construction of the matrix $\mathcal{G}_{AB}$. Once we calculate the matrix, however, we can use it for different lattice data (e.g. NBS wave functions calculated on different gauge samples). Therefore, it is better to calculate the dual basis functions (Eq. (4.37)) once before the calculation of the spherical harmonics amplitude from NBS wave functions and use them for later analysis. Finally, the dual basis functions consume large memory to store. For example, when the lattice size is $L = 32$ and the number of the basis is given by $n_{\max} = 4$ and $l_{\max} = 6$, required memory for $\tilde{\mathcal{Y}}^{R,\Delta}_{nlm}(\vec{x})$ is $32^3 \times 5 \times (1+3+5+7+9+11+13) \times 16$ (bytes) $= 122.5$ MB. In order to reduce the memory, it is better to calculate the following function:

$$G^{R,\Delta}_{lm}(\vec{x}) \equiv \sum_{n=0}^{n_{\max}} \overline{G^{R,\Delta}_{n}(R)}\ \tilde{\mathcal{Y}}^{R,\Delta}_{nlm}(\vec{x}), \tag{4.38}$$

which required only $32^3 \times (1+3+5+7+9+11+13) \times 16$ (bytes) $= 24.5$ MB in memory. Using this function, the spherical harmonics amplitude $g_{lm}(R)$ can be calculated directory as

$$\begin{aligned} \langle G^{R,\Delta}_{lm}|\psi\rangle^{\rm disc}_{S_{R,\Delta}} &= \sum_{n=0}^{n_{\max}} G^{R,\Delta}_{n}(R)\ \langle \tilde{\mathcal{Y}}^{R,\Delta}_{nlm}|\psi\rangle^{\rm disc}_{S_{R,\Delta}} \\ &\sim \sum_{n=0}^{n_{\max}} G^{R,\Delta}_{n}(R)\ c^{R,\Delta}_{nlm} \\ &\sim g_{lm}(R). \end{aligned} \tag{4.39}$$

Furthermore, since the weight function $\omega^{R,\Delta}(\vec{x})$ has non-zero values at points only around the shell $S_{R,\Delta}$, it enough to store the $G^{R,\Delta}_{lm}(\vec{x})$ in memory only at points where the weight function is non-zero.

[4]This situation is similar to the parameter fitting by the least squares method. When we employ a test function with a large number of parameters for a small number of data points, the fitting may have strong numerical instability.

4.4 Consideration from the least square method

We have presented two different approaches to extract spherical harmonics amplitudes in Secs. 4.2 and 4.3. The method in Sec. 4.2, we solve the simultaneous equation for the A_1^+ projected NBS wave function as Eqs. (4.12) and (4.15) in a fixed r. If we consider the extraction up to $L = 4$ component, the equation can be solved exactly for a number of points at the same r $N = 2$. For $N > 2$, however, the solution is given as approximately because a number of the solution is smaller than a number of the equation. In this case, we can minimize mean square errors of the solution by using the SVD. In order to see how the SVD minimizes the error, it is useful to consider this inverse problem on a least square aspect. Furthermore, the consideration from the least square method also gives us knowledge how the dual basis function defined in Eq. (4.37) for Misner's method minimizes the mean square errors [55]. From these considerations, we will find that the method in Secs. 4.2 and 4.3 can be regarded as one of the parameter fittings by the least square method for the spherical harmonics amplitudes.

4.4.1 The case of the decomposition from A_1^+ projected data in fixed r

Let us consider that there are N data points of the A_1^+ projected NBS wave function at fixed r, and we write them as $N \times 1$ column vector $\boldsymbol{\Psi}^{A_1^+} \equiv (\psi^{A_1^+}(\vec{x}_1), \cdots, \psi^{A_1^+}(\vec{x}_N))^T$, where $|\vec{x}_i| = r$ for $i = 1, \cdots, N$. We assume that each NBS wave function is decomposed as

$$\psi^{A_1^+}(\vec{x_i}) = Y_{00}^{A_1^+} g_{00}(r) + Y_4^{A_1^+}(\vec{x}_i) g_4(r) + Y_6^{A_1^+}(\vec{x}_i) g_6(r) + \cdots , \tag{4.40}$$

where $Y_l^{A_1^+}(\vec{x}_i)$ represents the A_1^+ projected spherical harmonics for an angular momentum l. For the spherical harmonics amplitudes $g_l(r)$, let us define $\boldsymbol{G}$ as $M \times 1$ column vector $\boldsymbol{G} = (g_{00}(r), g_4(r), g_6(r), \cdots)^T$. We finally define the design matrix $\boldsymbol{Y}^{A_1^+}$ as an $N \times M$ rectangle matrix which consists of the A_1^+ projected spherical harmonics, which is given

by

$$\boldsymbol{Y}^{A_1^+} = \begin{pmatrix} Y_{00}^{A_1^+} & Y_4^{A_1^+}(\vec{x}_1) & Y_6^{A_1^+}(\vec{x}_1) & \cdots \\ \vdots & \vdots & \vdots & \\ Y_{00}^{A_1^+} & Y_4^{A_1^+}(\vec{x}_N) & Y_6^{A_1^+}(\vec{x}_N) & \cdots \end{pmatrix}. \tag{4.41}$$

When we write an approximate solution of the spherical harmonics amplitudes $\tilde{\boldsymbol{G}}$, the sum of squared residuals $F(\tilde{\boldsymbol{G}})$ between $\boldsymbol{\Psi}^{A_1^+}$ and the given solution vector $\tilde{\boldsymbol{\Psi}}^{A_1^+} \equiv \boldsymbol{Y}^{A_1^+}\tilde{\boldsymbol{G}}$ is defined by

$$\begin{aligned} F(\tilde{\boldsymbol{G}}) &= \left(\tilde{\boldsymbol{\Psi}}^{A_1^+} - \boldsymbol{\Psi}^{A_1^+}\right)^\dagger \left(\tilde{\boldsymbol{\Psi}}^{A_1^+} - \boldsymbol{\Psi}^{A_1^+}\right) \\ &= \left(\boldsymbol{Y}^{A_1^+}\tilde{\boldsymbol{G}} - \boldsymbol{\Psi}^{A_1^+}\right)^\dagger \left(\boldsymbol{Y}^{A_1^+}\tilde{\boldsymbol{G}} - \boldsymbol{\Psi}^{A_1^+}\right), \end{aligned} \tag{4.42}$$

which is minimized at $dF(\tilde{\boldsymbol{G}}_{\min})/d\tilde{\boldsymbol{G}} = 0$. $\tilde{\boldsymbol{G}}_{\min}$ is calculated by

$$\tilde{\boldsymbol{G}}_{\min} = \left((\boldsymbol{Y}^{A_1^+})^\dagger \boldsymbol{Y}^{A_1^+}\right)^{-1} (\boldsymbol{Y}^{A_1^+})^\dagger \ \boldsymbol{\Psi}^{A_1^+}. \tag{4.43}$$

Here $\left((\boldsymbol{Y}^{A_1^+})^\dagger \boldsymbol{Y}^{A_1^+}\right)^{-1} (\boldsymbol{Y}^{A_1^+})^\dagger$ is nothing but the generalized inverse matrix defined by the SVD. In order to see this, we decompose $\boldsymbol{Y}^{A_1^+}$ by the SVD as $\boldsymbol{Y}^{A_1^+} = U\Sigma V^\dagger$ with unitary matrixes U, V and a diagonal matrix for the singular values Σ defined in Eq. (4.13), then we have

$$\begin{aligned} \tilde{\boldsymbol{G}}_{\min} &= \left((U\Sigma V^\dagger)^\dagger U\Sigma V^\dagger\right)^{-1} (U\Sigma V^\dagger)^\dagger \ \boldsymbol{\Psi}^{A_1^+} \\ &= \left(V\Sigma^\dagger U^\dagger U\Sigma V^\dagger\right)^{-1} V\Sigma^\dagger U^\dagger \ \boldsymbol{\Psi}^{A_1^+} \\ &= V(\Sigma^\dagger\Sigma)^{-1}V^\dagger V\Sigma^\dagger U^\dagger \ \boldsymbol{\Psi}^{A_1^+} \\ &= V(\Sigma^\dagger\Sigma)^{-1}\Sigma^\dagger U^\dagger \ \boldsymbol{\Psi}^{A_1^+}, \end{aligned} \tag{4.44}$$

where $(\Sigma^\dagger\Sigma)^{-1}\Sigma^\dagger$ equals to Σ^{-1} defined in Eq. (4.14) since the singular values defined in positive real values. Obviously, $\tilde{\boldsymbol{G}}_{\min} = V\Sigma^{-1}U^\dagger \ \boldsymbol{\Psi}^{A_1^+}$ is the solution calculated from SVD.

We here discuss in the viewpoint of a parameter fitting by the least square method. The forms of the equations (4.42) and (4.43) are equivalent to those in the parameter fitting. In this context, we regard $\boldsymbol{\Psi}^{A_1^+}, \boldsymbol{G}$, and $\boldsymbol{Y}^{A_1^+}$ as data points, fit parameters, and

fit functions, respectively. Therefore, we can consider the method in Sec. 4.2 as fitting for the spherical harmonics amplitudes by the fit function $\boldsymbol{Y}^{A_1^\dagger}$.

4.4.2 The case of the Misner's method

We give here the consideration from the viewpoint of the least square method for Misner's method discussed in Ref. [55]. Let us consider $N \times 1$ column vector $\boldsymbol{\Psi}$ as N data points of the NBS wave functions in/around the shell $S_{R,\Delta}$ in which the weight $\omega^{R,\Delta}(\vec{x})$ has a non-zero value. Each NBS wave function is decomposed as Eq. (4.23). Similarly, let us define an $N \times M$ rectangle matrix $\boldsymbol{Y}$ as N points of the M basis functions $\mathcal{Y}^{R,\Delta}_{nlm}$. For example, for $n_{\max} = 2$ and $l_{\max} = 2$, $\boldsymbol{Y}$ is given by

$$\boldsymbol{Y} = \begin{pmatrix} \mathcal{Y}^{R,\Delta}_{0,0,0}(\vec{x}_1) & \mathcal{Y}^{R,\Delta}_{0,1,-1}(\vec{x}_1) & \mathcal{Y}^{R,\Delta}_{0,1,0}(\vec{x}_1) & \cdots & \mathcal{Y}^{R,\Delta}_{2,2,2}(\vec{x}_1) \\ \vdots & \vdots & \vdots & & \vdots \\ \mathcal{Y}^{R,\Delta}_{0,0,0}(\vec{x}_N) & \mathcal{Y}^{R,\Delta}_{0,1,-1}(\vec{x}_N) & \mathcal{Y}^{R,\Delta}_{0,1,0}(\vec{x}_N) & \cdots & \mathcal{Y}^{R,\Delta}_{2,2,2}(\vec{x}_N) \end{pmatrix}, \tag{4.45}$$

where the number of rows is $M = 3 \times (1 + 3 + 5) = 27$. When we define an $N \times N$ diagonal matrix $\boldsymbol{W}$ for the weight $\omega^{R,\Delta}(\vec{x})$, the matrix $\mathcal{G}_{AB}$ introduced in Eq. (4.32) is simply written by $\boldsymbol{\mathcal{G}} = \boldsymbol{Y}^\dagger \boldsymbol{W} \boldsymbol{Y}$. Using above matrixes, let us estimate the sum of squared residuals $F(\tilde{\boldsymbol{G}})$ between the $\boldsymbol{\Psi}$ and an approximate solution vector $\tilde{\boldsymbol{\Psi}} \equiv \boldsymbol{Y}\tilde{\boldsymbol{G}}$, where $\tilde{\boldsymbol{G}}$ is $M \times 1$ column vector for an approximate solution of the coefficient in Eq. (4.23). Since we have weights $\boldsymbol{W}$, $F(\tilde{\boldsymbol{G}})$ is better to estimate as the weighted sum of squared residuals defined by

$$\begin{aligned} F(\tilde{\boldsymbol{G}}) &= \left(\tilde{\boldsymbol{\Psi}} - \boldsymbol{\Psi}\right)^\dagger \boldsymbol{W} \left(\tilde{\boldsymbol{\Psi}} - \boldsymbol{\Psi}\right) \\ &= \left(\boldsymbol{Y}\tilde{\boldsymbol{G}} - \boldsymbol{\Psi}\right)^\dagger \boldsymbol{W} \left(\boldsymbol{Y}\tilde{\boldsymbol{G}} - \boldsymbol{\Psi}\right), \end{aligned} \tag{4.46}$$

which is minimized at $dF(\tilde{\boldsymbol{G}}_{\min})/d\tilde{\boldsymbol{G}} = 0$ with

$$\begin{aligned} \tilde{\boldsymbol{G}}_{\min} &= \left(\boldsymbol{Y}^\dagger \boldsymbol{W} \boldsymbol{Y}\right)^{-1} \boldsymbol{Y}^\dagger \boldsymbol{W}\ \boldsymbol{\Psi} \\ &= \boldsymbol{\mathcal{G}}^{-1} \boldsymbol{Y}^\dagger \boldsymbol{W}\ \boldsymbol{\Psi}. \end{aligned} \tag{4.47}$$

This solution is equivalent to Eq. (4.34) for a finite number of the basis function. We find, indeed, that the dual basis function defined in Eq. (4.37) minimizes the mean square

error between $\langle \tilde{\mathcal{Y}}_A^{R,\Delta} | \psi \rangle_{S_{R,\Delta}}^{\text{disc}}$ and $c_A^{R,\Delta}$ for given $n_{\max}$ and $l_{\max}$.

In the context of the least square method, we can consider Misner's method as a fitting for the spherical harmonics amplitudes by fit functions $\boldsymbol{Y}$ with the weight $\boldsymbol{W}$ in/around the shell $S_{R,\Delta}$.

Chapter 5

Numerical results

5.1 Simulation setup

For numerical simulations in this thesis, we employ the $(2+1)$-flavor full QCD configurations generated by PACS-CS Collaboration with the renormalization-group improved Iwasaki gluon action and a nonperturbatively $\mathcal{O}(a)$ improved Wilson-clover quark action at $\beta = 6/g^2 = 1.90$ on a $L^3 \times T = 32^3 \times 64$ lattice [16]. The improved clover coefficient is determined nonperturbatively in Ref. [56] as $c_{SW} = 1.715$. The corresponding lattice spacing is $a = 0.0907(13)$ fm and physical lattice size is $La = 2.902(42)$ fm. This gauge ensemble data are available on the website of the Japan Lattice Data Grid (JLDG) [57].

There are six ensembles, which cover the pion mass from 700 MeV to 156 MeV. Due to the limited computational resources, we utilize the heavier quark masses in our lattice simulation. In order to see the quark mass dependence of observables, we employ three ensembles. Table. 5.1 show that hopping parameters and corresponding pion masses and kaon masses for each gauge ensemble which is used in this thesis.

Table 5.1: Hopping parameters and corresponding pion masses and kaon masses for gauge ensembles we used in this thesis. The pion masses and the kaon masses are referred to Ref. [16].

	κ_{ud}	κ_s	m_π [MeV]	m_K [MeV]
Ensemble 1	0.13700	0.13640	701	790
Ensemble 2	0.13727	0.13640	570	713
Ensemble 3	0.13754	0.13640	411	635

For the charm quark, we employ the relativistic heavy quark (RHQ) action [36] to avoid the leading $\mathcal{O}\left((m_Q a)^n\right)$ and the next-to-leading $\mathcal{O}\left((m_Q a)^n (a\Lambda_{\rm QCD})\right)$ discretization errors due to the charm quark mass m_Q. We take the improved parameters κ_Q, r_s, ν, c_B and c_E determined in Ref. [18] so as to reproduce the experimental value of the mass and the relativistic dispersion relation for the charmonium in spin-averaged $1S$ state. The RHQ parameters are listed in Table 5.2. Note that charm quark creation and annihilation

Table 5.2: RHQ parameters in our simulations. These parameters are determined in Ref. [18] so as to reproduce the experimental value of the mass and the relativistic dispersion relation for the charmonium in spin-averaged $1S$ state.

κ_Q	r_s	ν	c_B	c_E
0.10959947	1.1881607	1.1450511	1.9849139	1.7819512

effects are not included in the gauge configuration. That is, we treat the charm quark in the quenched approximation. The effects of charm loops for charmed baryons, however, are expected to be small as studied e.g. in Refs. [58, 59]. Nevertheless, the effect to the charmed baryon interaction is an interesting open question to be investigated in the future.

We calculate quark propagators with the periodic boundary condition for the spatial directions, while the Dirichlet boundary condition is imposed on the temporal direction at the time-slice $t = 32 + t_0$. The reason for imposing the Dirichlet boundary condition is that we independently treat correlation functions for forward propagation and backward propagation in time to take an average them for increasing the statistics. The correlation functions are calculated using the unified contraction algorithm [60]. For the source operator, we employ the wall source defined below Eq. (3.16) to get better signals. We take 64 different time-slices for each configuration as the wall source location. The total statistics of each ensemble are given in Table 5.3.

For all analyses in this thesis, we employ the Jackknife method to estimate statistical errors. The methodology of the Jackknife method is summarized in Appendix A.2. The binsize of Jackknife samples is taken to 57, 40 and 45 for the Ensemble 1, 2 and 3, respectively. We confirm that change of binsize does not affect the errors for hadron masses as well as the errors for potentials and phase shifts.

Various hadron masses are calculated by fitting hadron two-point correlation functions

Table 5.3: The number of configurations and sources. The factor of two in # of sources means forward and backward propagations in time.

	# of gauge configs.	# of sources
Ensemble 1	399	64×2
Ensemble 2	400	64×2
Ensemble 3	450	64×2

with the exponential type fit function. The results are summarized in Table 5.4.

Table 5.4: Calculated hadron masses in unit of [MeV] for each ensemble. The fit range in $t - t_0$ is [10, 20] for π in Ensemble 2, [10, 15] for π in Ensemble 3, [19,24] for Ξ_{cc} and [15, 20] for all other cases.

	Ensemble 1	Ensemble 2	Ensemble 3
m_π	702(2)	570(1)	412(2)
m_K	789(2)	713(1)	637(2)
m_D	1999(1)	1949(2)	1904(2)
m_N	1581(6)	1399(9)	1215(9)
m_Λ	1642(6)	1493(7)	1342(6)
m_Σ	1657(6)	1522(8)	1395(9)
m_Ξ	1709(5)	1599(7)	1500(7)
m_{Λ_c}	2685(3)	2555(5)	2434(6)
m_{Σ_c}	2780(5)	2674(7)	2575(9)
$m_{\Xi_{cc}}$	3801(2)	3727(3)	3673(4)

For the local interpolating operators in Eq. (3.14), we employ the following form for a nucleon, Λ_c, Σ_c, and Ξ_c as

$$B_\alpha(x) = \epsilon_{ijk} \left[q_i^T(x) C\gamma_5 q_j(x) \right] q_{k,\alpha}(x), \tag{5.1}$$

where $x = (\vec{x}, t)$, and i, j, k are color indices. C is the charge conjugation matrix defined by $C = \gamma_2\gamma_4$, and $q = u, d, c$ stand for quark operators for up-, down- and charm-quarks, respectively. Flavor structures are given by

$$N = \begin{pmatrix} p \\ n \end{pmatrix} = \begin{pmatrix} [ud]\, u \\ [ud]\, d \end{pmatrix}$$

$$
\begin{aligned}
\Lambda_c &= \frac{1}{\sqrt{6}}\left([cd]\,u + [uc]\,d - 2\,[du]\,c\right) \\
\Sigma_c &= \begin{pmatrix} \Sigma_c^{++} \\ \Sigma_c^{+} \\ \Sigma_c^{0} \end{pmatrix} = \begin{pmatrix} [cu]\,u \\ \frac{1}{\sqrt{2}}\left([cd]\,u + [cu]\,d\right) \\ [cd]\,d \end{pmatrix} \\
\Xi_{cc} &= \begin{pmatrix} \Xi_{cc}^{++} \\ \Xi_{cc}^{+} \end{pmatrix} = \begin{pmatrix} [cu]\,c \\ [cd]\,c \end{pmatrix}
\end{aligned} \tag{5.2}
$$

5.2 2-body interaction in $\Lambda_c N$ system

In this section, we show the numerical results of single channel potentials for the $\Lambda_c N$ system and discuss the $\Lambda_c N$ interaction. In order to investigate all of the leading order potentials in the velocity expansion defined in Sec. 3.1.5, we calculate the $\Lambda_c N$ potentials in both ${}^1S_0$ channel and ${}^3S_1 - {}^3D_1$ channel. These potentials are constructed from the NBS wave functions for the $\Lambda_c N$ system projected into the desired spin channel. For the angular momentum projection, we employ Misner's method explained in Sec. 4.3. Before we show the results of the potential, we present the numerical results of applying Misner's method to the R-correlator. The discussion of applying Misner's method is based on Ref. [26], while the discussion of the $\Lambda_c N$ interaction is based on Refs. [22, 23].

5.2.1 R-correlator for the $\Lambda_c N$ system in ${}^1S_0$ channel with Misner's method

We first present numerical results of the R-correlator (normalized baryon four-point correlation function) defined as Eq. (3.25) for $\Lambda_c N$ system in the ${}^1S_0$ channel. The R-correlator is calculated at $t - t_0 = 13$ for $m_\pi \simeq 700$ MeV case. The projection to the ${}^1S_0$ channel is given in Eq. (3.33). This quantity corresponds to the NBS wave function for the $\Lambda_c N$ system in the ${}^1S_0$ channel. As we discussed in Sec. 3.1.5, however, the A_1^+ projection leaves $L \geq 4$ components in the wave function, which may make comb-like structures in the R-correlator plot as a function of the radial r. In order to see the effects of the higher partial wave components, we apply Misner's method to decompose the $L = 0$ component (the spherical harmonics amplitude for $Y_{0,0}$) directly from the non-A_1^+ projected R-correlator. For Misner's method, we employ the parameters $\Delta, n_{\max}$, and $l_{\max}$ as a (lattice spacing)

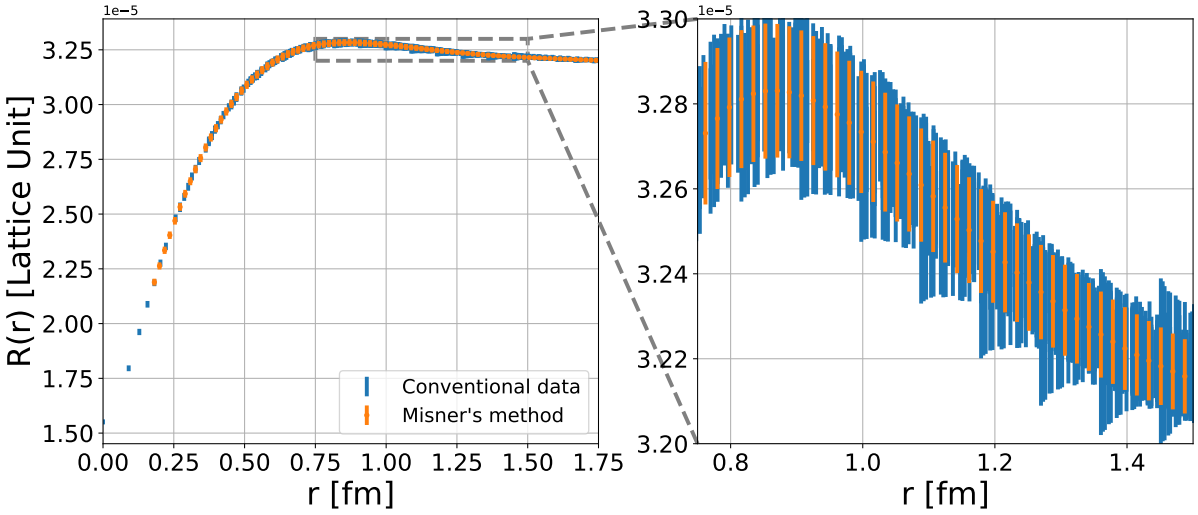

Figure 5.1: R-correlator (normalized baryon four-point correlation function) for $\Lambda_c N$ system in the ${}^1S_0$ channel. The R-correlator is calculated at $t - t_0 = 13$ for $m_\pi \simeq 700$ MeV case. The blue line shows the R-correlator with A_1^+ projection divided by Y_{00}, and the orange line corresponds to the spherical harmonics amplitude for $Y_{0,0}$ calculated by Misner's method.

, 3, and 5, respectively. Misner's method is applied for a spherical shell around given $r = R$. We calculate each R in unit of $0.2a$ from $2a$ to $16a$ for radial coordinates of the spherical harmonics amplitude, so that some data are repeatedly used to calculate the spherical harmonics amplitude. When we apply Misner's method for $R < 2a$, the solution cannot be obtained due to few data points. For $R > 16a$, on the other hands, we may obtain insufficient solution because the spherical shell becomes too large to enclose in a finite spatial extension. Misner's method is applied to each Jackknife sample for the R-correlators and we estimate the statistical errors for the spherical harmonics amplitude. Fig. 5.1 shows the R-correlator with A_1^+ projection as well as the $L = 0$ component calculated by Misner's method. From Fig. 5.1, we find small comb-like structures in the R-correlator, which are not appeared in the $L = 0$ component by Misner's method. This observation shows that the $L \geq 4$ components are small but exist so that they make comb-like structures in the R-correlator plot.

Next, we give results for Laplacian of the R-correlator in Misner's method, which affect the structure of the potential. In the conventional method, the Laplacian is defined by a finite second-order difference. In Misner's method, however, it is calculated analytically as the second-order derivative defined in Eq. (4.36). We give their results in Fig. 5.2, which

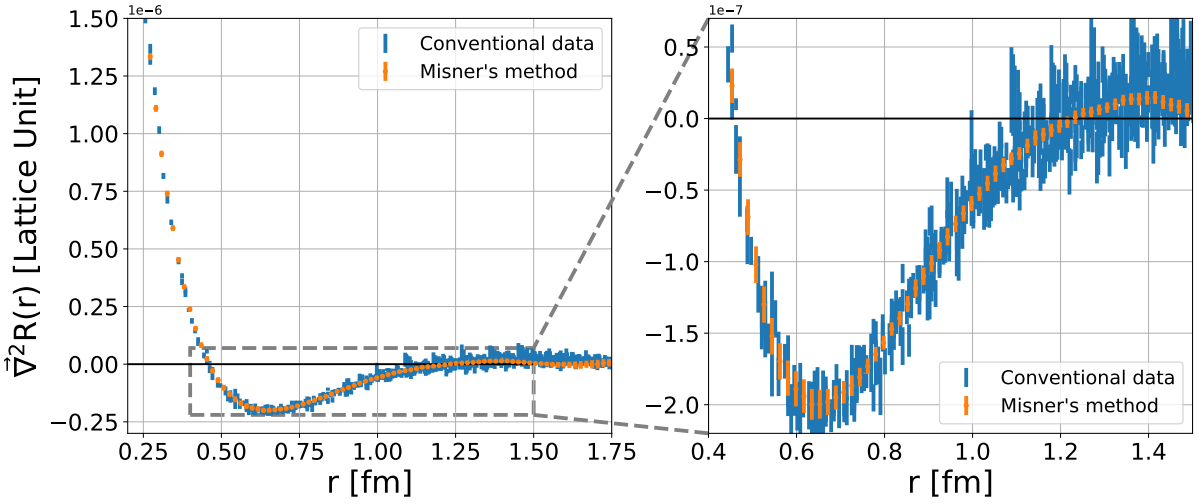

Figure 5.2: The Laplacian of R-correlator (normalized baryon four-point correlation function) for $\Lambda_c N$ system in the ${}^1S_0$ channel. The R-correlator is calculated at $t - t_0 = 13$ for $m_\pi \simeq 700$ MeV case. The blue line shows the Laplacian of the R-correlator with A_1^+ projection divided by Y_{00}, and the orange line corresponds to the Laplacian of the spherical harmonics amplitude for $Y_{0,0}$ calculated by Misner's method. The former Laplacian is defined by a finite second-order difference, while the latter is calculated as in Eq. (4.36).

shows that the comb-like structures in the Laplacian of the R-correlator are reduced in Misner's method. From their observations, we find that the $L \geq 4$ components in the wave function may produce large comb-like structures in the Laplacian (also in potential) even the amplitude of the $L \geq 4$ components is small. Since the comb-like structures are unphysical (i.e. lattice artifacts), it is better to use Misner's method to calculate the Laplacian of the R-correlator.

5.2.2 R-correlator for the $\Lambda_c N$ system in ${}^3S_1 - {}^3D_1$ channel with Misner's method

We next show numerical results of the R-correlator for $\Lambda_c N$ system in the ${}^3S_1 - {}^3D_1$ channel. The R-correlator is calculated at $t - t_0 = 13$ for $m_\pi \simeq 700$ MeV case. Since the wall source is A_1^+ symmetric, the total angular momentum in the source is fixed to $J^P = 1^+$ by projecting the total spin to $S = 1$. In this case, S-wave component and D-wave component are mixed in $t - t_0 > 0$ because the spin and the orbital angular momentum are not preserved in QCD. In order to extract individual components, we define the D-wave projection by $(1 - P^{(A_1^+)})$ with the A_1^+ projection $P^{(A_1^+)}$. Since the A_1^+

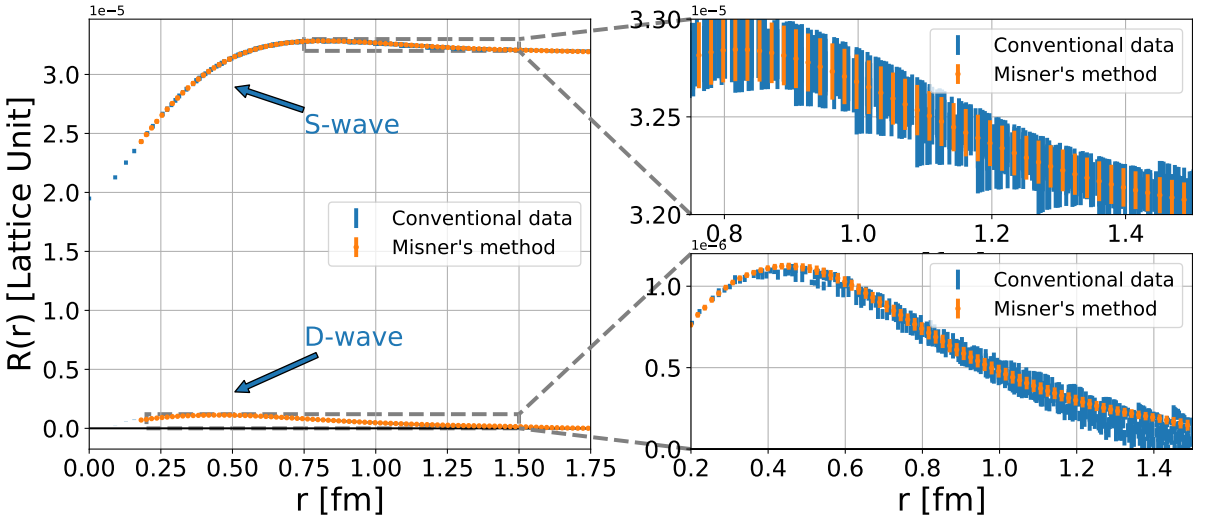

Figure 5.3: R-correlator (normalized baryon four-point correlation function) for $\Lambda_c N$ system in the ${}^3S_1 - {}^3D_1$ channel. The R-correlator is calculated at $t - t_0 = 13$ for $m_\pi \simeq 700$ MeV case. The blue line shows the original R-correlator data and the orange line corresponds to the spherical harmonics amplitude calculated by Misner's method.

projection cannot remove $L \geq 4$ components, the $(1 - P^{(A_1^+)})$ projection also leaves $L \geq 4$ components into D-wave R-correlator. Fig. 5.3 shows that the R-correlators in the ${}^3S_1$ and the ${}^3D_1$ channels as well as the $L = 0$ and the $L = 2$ components of the spherical harmonics amplitudes extracted by Misner's method. The numerical setup for Misner's method is the same as in the ${}^1S_0$ channel case. We find comb-like structures in original R-correlator data for both channels, where the contaminations from higher partial waves in D-wave channel seem larger than those in S-wave channel.

The Laplacians of the R-correlator are also calculated by a finite second-order difference for original R-correlator data while they are calculated analytically for the spherical harmonics amplitudes extracted by Misner's method, as shown in Fig. 5.4. The comb-like structures in the Laplacian of the R-correlator are reduced as in the case of the ${}^1S_0$ channel.

Hereafter, we employ Misner's method to calculate all of the results on the lattice simulation.

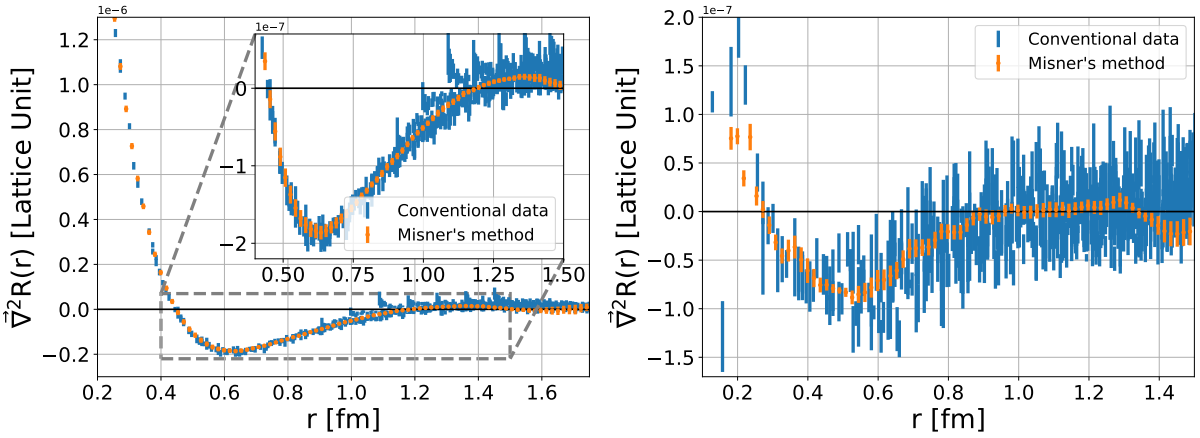

Figure 5.4: The Laplacian of R-correlator (normalized baryon four-point correlation function) for $\Lambda_c N$ system in the ${}^3S_1 - {}^3D_1$ channel. The R-correlator is calculated at $t - t_0 = 13$ for $m_\pi \simeq 700$ MeV case. The blue line shows the Laplacian of the original R-correlator data and the orange line corresponds to the Laplacian of the spherical harmonics amplitude calculated by Misner's method. The former Laplacian is defined by a finite second-order difference, while the latter is calculated as in Eq. (4.36).

5.2.3 Potentials for the $\Lambda_c N$ system in ${}^1S_0$ channel

Using the R-correlators calculated with Misner's method, we next construct the central potentials for the $\Lambda_c N$ system. The left figure in Fig. 5.5 shows the $\Lambda_c N$ central potential in the ${}^1S_0$ channel for each gauge ensemble. We employ the time-dependent HAL QCD method defined in Sec. 3.1.4 to construct the potentials. The potentials are calculated at $t - t_0 = 13$ (Ensemble 1: $m_\pi \simeq 700$ MeV), $t - t_0 = 11$ (Ensemble 2: $m_\pi \simeq 570$ MeV) and $t - t_0 = 9$ (Ensemble 3: $m_\pi \simeq 410$ MeV). We confirm the stability of the potential against the time separations $t - t_0$, which indicates that the contributions from inelastic channels can be neglected. We find a repulsive core at a short distance ($r \lesssim 0.5$ fm) and an attractive pocket at an intermediate distance ($0.5 \lesssim r \lesssim 1.5$ fm) in the $\Lambda_c N$ potential. We also observe that the height of the repulsive core increases and the minimum of the attractive pocket shifts outward, as u, d quark masses decrease. A variation of the repulsive core against u, d quark masses may be explained by the fact that the color magnetic interaction is proportional to the inverse of the constituent quark mass [61]. For comparison, we calculate the interactions for the ΛN system in ${}^1S_0$ channel, which are also shown in the right figure in Fig. 5.5. From the comparison, we notice that the attraction of the $\Lambda_c N$ potential seems weaker than that of the ΛN potential.

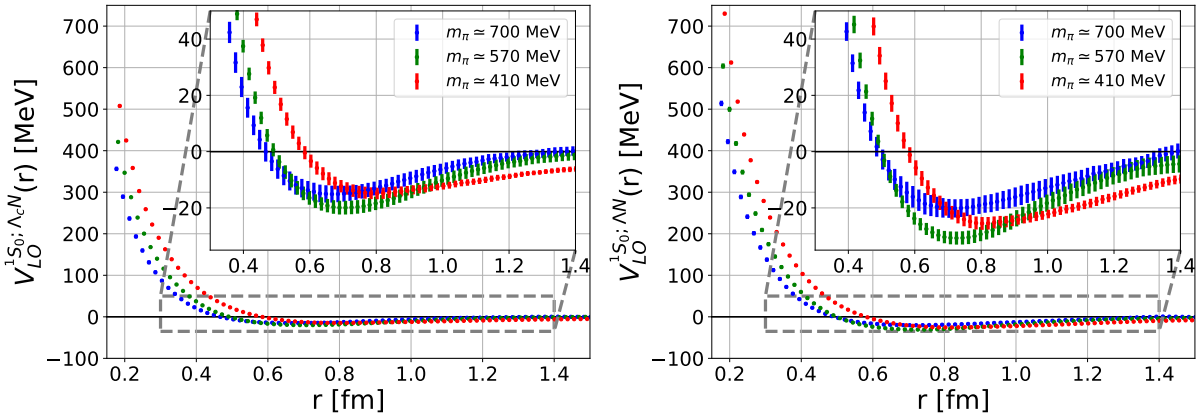

Figure 5.5: The $\Lambda_c N$ central potential (Left figure) and the ΛN central potential (Right figure) in the $^1S_0$ channel for each gauge ensemble. The potentials are calculated at $t - t_0 = 13$ for $m_\pi \simeq 700$ MeV case (Blue), $t - t_0 = 11$ for $m_\pi \simeq 570$ MeV case (Green) and $t - t_0 = 9$ for $m_\pi \simeq 410$ MeV case (Red).

5.2.4 $\Lambda_c N$ central and tensor potentials in $^3S_1 - ^3D_1$ channel

The upper two figures in Fig. 5.6 show the central potential (Left figure) and the tensor potential (Right figure) for the $\Lambda_c N$ system with $J^P = 1^+$. In the lower two figures, we also show the potentials for the ΛN system with $J^P = 1^+$. Each potential is calculated by the time-dependent HAL QCD method defined in Sec. 3.1.4. These potentials are calculated at $t - t_0 = 13$ (Ensemble 1: $m_\pi \simeq 700$ MeV), $t - t_0 = 11$ (Ensemble 2: $m_\pi \simeq 570$ MeV) and $t - t_0 = 9$ (Ensemble 3: $m_\pi \simeq 410$ MeV). It is confirmed that these potentials are stable against the change of $t - t_0$ within the statistical errors, as was observed in the central potential in the $^1S_0$ channel. We notice that the central potential is similar to the one in the $^1S_0$ channel except at short distance ($r \lesssim 0.5$ fm). The tensor potential of the $\Lambda_c N$ system is weak compared to that of the ΛN system. We also find that the u, d quark mass dependence of the tensor potentials is weak for the $\Lambda_c N$ system.

The weaker $\Lambda_c N$ potential than ΛN could be explained by the following facts: (i) The long-range contribution is expected to be caused by the K meson exchange for ΛN interaction [6]. In the $\Lambda_c N$ system, however, the K meson (strange quark) exchange is replaced by the D meson (charm quark) exchange, and this contribution is highly suppressed due to the much larger D meson mass than the K meson mass. (ii) The one-pion-exchange in the $\Lambda N - \Sigma N$ transition is considered to give a sizable contribution to the effective ΛN interaction. In the $\Lambda_c N$ system, however, this contribution is expected to be suppressed due to the large mass difference between $\Lambda_c N$ and $\Sigma_c N$.

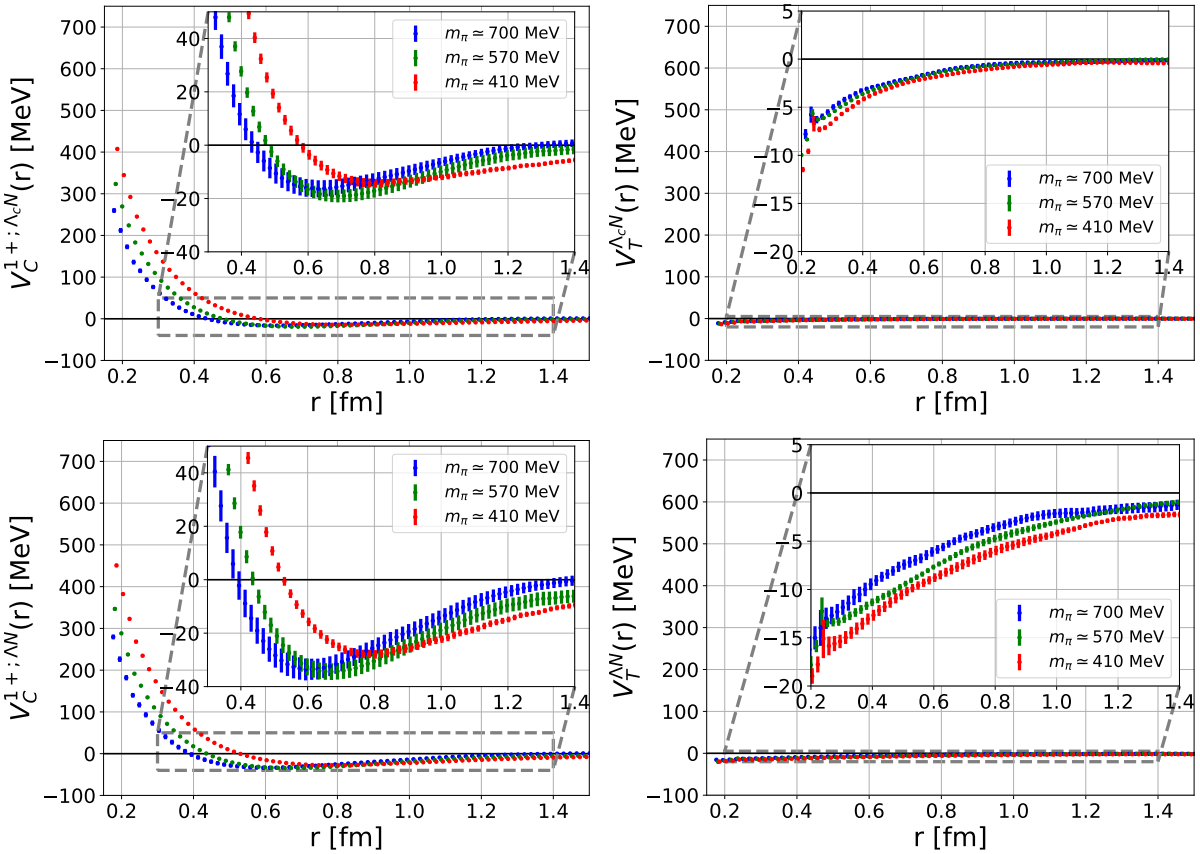

Figure 5.6: The central potential V_C and the tensor potential V_T for the $\Lambda_c N$ system (Upper two figures) and the ΛN system (Lower two figures) in the ${}^3S_1 - {}^3D_1$ channel for each ensemble. The potentials are calculated at $t - t_0 = 13$ for $m_\pi \simeq 700$ MeV case (Blue), $t - t_0 = 11$ for $m_\pi \simeq 570$ MeV case (Green) and $t - t_0 = 9$ for $m_\pi \simeq 410$ MeV case (Red).

5.2.5 Spin-independent potential and spin-spin potential for $\Lambda_c N$ system

The upper two figures in Fig. 5.7 show the $\Lambda_c N$ spin-independent central potential V_0 (Left figure) and the spin-dependent one V_σ (Right figure) defined in Eq. (3.40), while we show those potentials for ΛN system in the lower two figures. It is easy to see that the spin-dependent potential V_σ for $\Lambda_c N$ system is negligibly small compared to one for ΛN system, and the spin-independent central potential gives a significant contribution for $\Lambda_c N$ potentials. The observation of the small spin-dependent potential V_σ for $\Lambda_c N$ system can be explained by the heavy D-meson mass and the large separation of the $\Lambda_c N - \Sigma_c N$ threshold, as we discussed in the previous subsection.

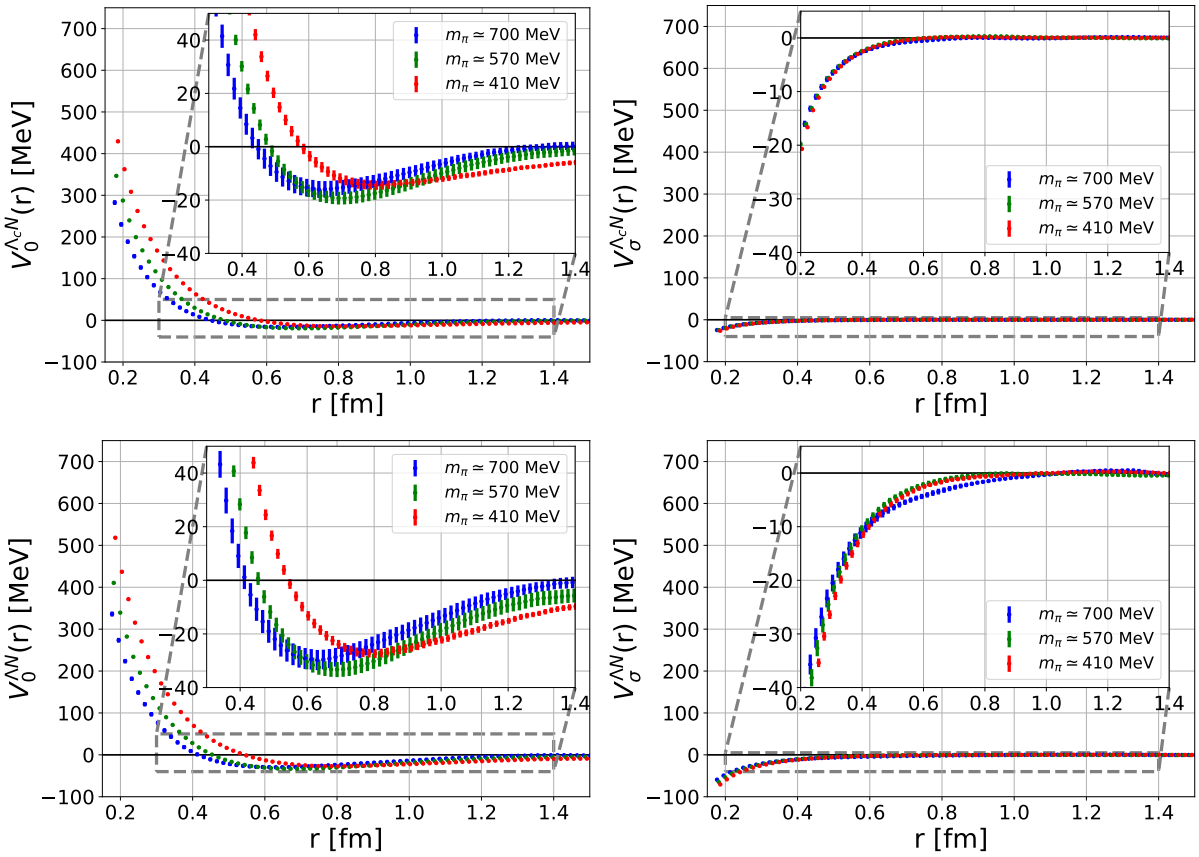

Figure 5.7: The spin-independent central potential V_0 and the spin-dependent one V_σ for the $\Lambda_c N$ system (Upper two figures) and the ΛN system (Lower two figures). The potentials are calculated at $t - t_0 = 13$ for $m_\pi \simeq 700$ MeV case (Blue), $t - t_0 = 11$ for $m_\pi \simeq 570$ MeV case (Green) and $t - t_0 = 9$ for $m_\pi \simeq 410$ MeV case (Red).

5.2.6 Phase shifts for $\Lambda_c N$ elastic scattering

We have calculated the $\Lambda_{(c)} N$ potentials in the previous three subsections and find that the $\Lambda_c N$ potentials seem weaker than the ΛN potentials. We also observe that the spin-independent $\Lambda_c N$ potential gives a significant contribution. Since the potential is not observable, however, we should discuss the interaction using physical observables such as scattering phase shifts. For this purpose, we interpolate the potential data with fit-functions and solve the Schrödinger equation with the fitted potentials in the infinite volume. For the fit-function for the $\Lambda_c N$ central potentials, we employ the following functional form:

$$V_{C;\mathrm{fit}}(r) = a_1 e^{-\left(\frac{r}{a_2}\right)^2} + a_3 e^{-\left(\frac{r}{a_4}\right)^2} + a_5 \left[\left(1 - e^{-a_6 r^2}\right) \frac{e^{-a_7 r}}{r}\right]^2, \tag{5.3}$$

where two Gaussians describe the repulsive core, while the third term reproduces an attractive pocket in the potential. The form of the third term is employed by respecting the fact that the long-range attraction in the $\Lambda_c N$ system is caused by the two-pion exchange. For the $\Lambda_c N$ tensor potentials, we employ the following functional form:

$$V_{T;\mathrm{fit}}(r) = a_1 \left(1 - e^{-a_2 r^2}\right) \left(1 - \frac{3}{a_3 r} - \frac{3}{(a_3 r)^2}\right) \frac{e^{-a_3 r}}{r}, \tag{5.4}$$

which is the phenomenological functional form for the tensor potential. We use the potential data at $r \in [2a, 16a]$ fm for the fitting.

In order to solve the Schrödinger equation, we employ a finite difference method starting from $r \sim 0$, and extract phase shifts from the asymptotic behavior of the wave function. Fig. 5.8 shows the phase shift for the $\Lambda_c N$ system in the ${}^1S_0$ channel for each

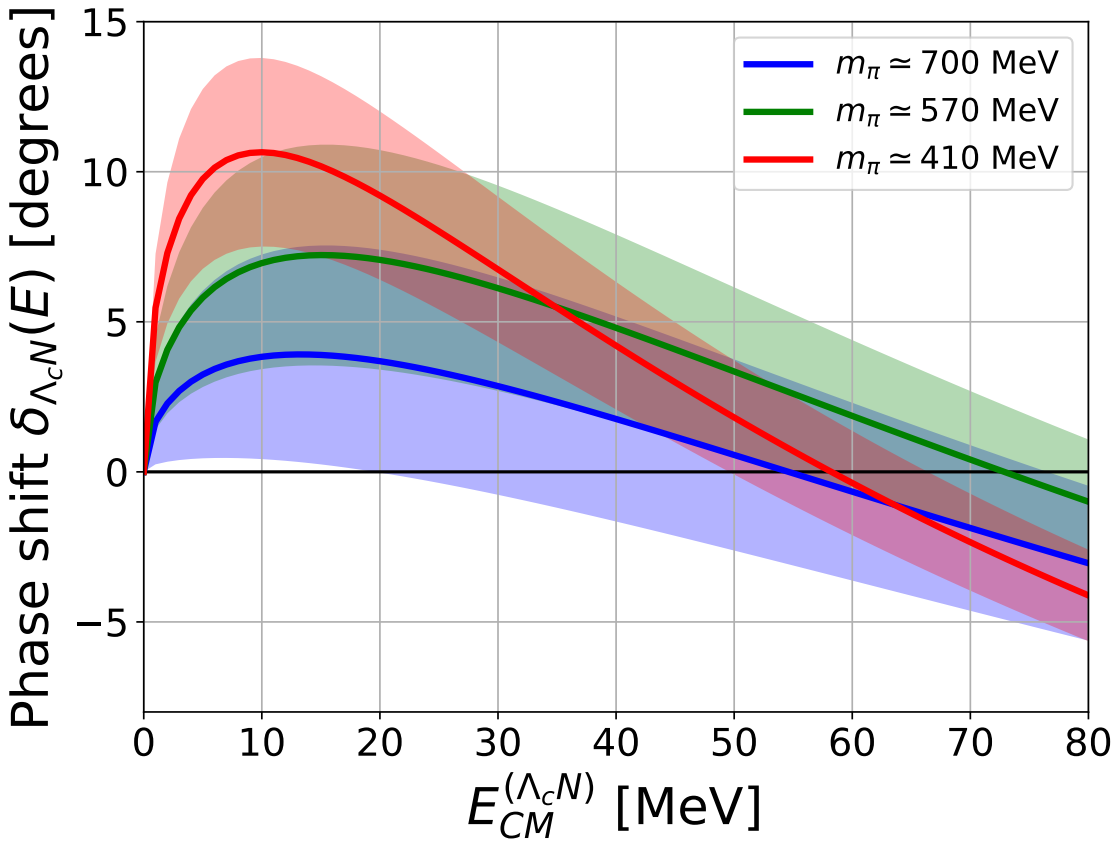

Figure 5.8: The phase shift for the $\Lambda_c N$ system in the ${}^1S_0$ channel.

ensemble. Results show that the net interaction in the ${}^1S_0$ channel is attractive for all cases at $E_{\mathrm{CM}} \lesssim 40$ MeV but not strong enough to form bound states. We also notice that

the attraction at low energies becomes stronger as the pion mass decreases.

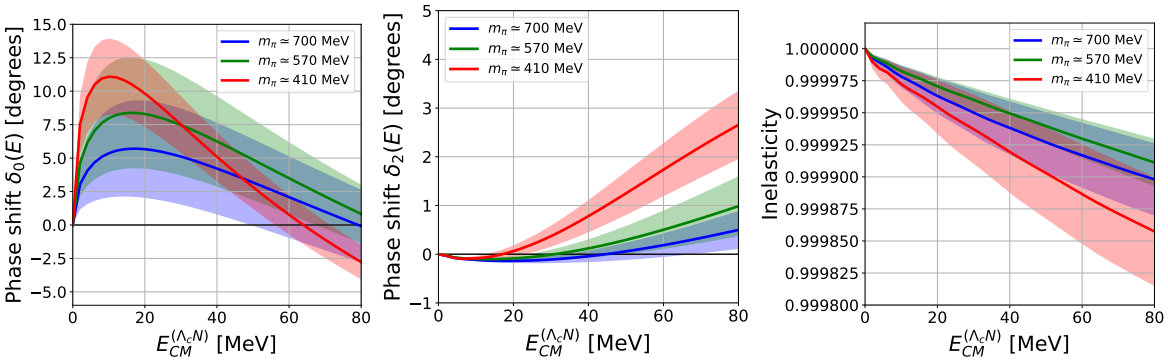

Figure 5.9: The phase shifts in the ${}^3S_1$ channel (Left figure), the ${}^3D_1$ channel (Middle figure) and the inelasticity (Right figure) for the $\Lambda_c N$ system in ${}^3S_1 - {}^3D_1$ channel.

Fig. 5.9 shows the phase shifts for the $\Lambda_c N$ system in the ${}^3S_1 - {}^3D_1$ channel for each ensemble. In this case, we solve the coupled channel Schrödinger equation for $S-D$ wave coupling. We find that the phase shift in the ${}^3S_1$ channel is almost the same to the one in the ${}^1S_0$ channel. The inelasticity, a strength of the $S-D$ coupling, is extremely small so that the S-wave and the D-wave are decoupled in the $\Lambda_c N$ system. These observations are coming from the fact that both of spin-spin potential and tensor potential for the $\Lambda_c N$ system are weak.

Note that the leading order approximation of the $\Lambda_c N$ potential may have sizable systematic errors around the $\Sigma_c N$ threshold ($E_{\rm CM} \simeq 95, 119$ and 141 MeV for $m_\pi \simeq 700, 570$ and 410 MeV case, respectively) due to the truncation of the derivative expansion of the non-local potential as we discussed in Sec. 3.2.1. Size of such systematic uncertainties of the $\Lambda_c N$ interactions near the $\Sigma_c N$ threshold can be estimated even at the leading order if the coupled-channel HAL QCD method is employed. This effect is discussed in the next section.

We next calculate low-energy parameters, the scattering length a_0 and the effective range $r_{\rm eff}$, defined by the effective range expansion:

$$k \cot \delta_0(k) = \frac{1}{a_0} + \frac{r_{\rm eff}}{2} k^2 + \mathcal{O}(k^4), \tag{5.5}$$

which give us significant information for interactions at low energies. Note that we employ the particle physics convention for the definition of scattering length which has opposite sign from the historical sign convention of the baryon-baryon interaction. The scattering

length and the effective range are determined by fitting $k \cot \delta_0(k)$ data at $k \in (0, 0.5]$ MeV with Eq. (5.5) as the fit-function. The results for $\Lambda_c N$ system are listed in Tables 5.5 and 5.6. From two results, we find the low-energy parameters for $\Lambda_c N$ system in $^1S_0$ channel

Table 5.5: The scattering length for the $\Lambda_c N$ system. We employ the particle physics convention for the definition of scattering length which has opposite sign from the historical sign convention of the baryon-baryon interaction.

m_π	$^1S_0$ channel	$^3S_1$ channel
412(2) MeV	0.50 (17) fm	0.51 (16) fm
570(1) MeV	0.25 (13) fm	0.28 (16) fm
702(2) MeV	0.13 (11) fm	0.17 (11) fm

Table 5.6: The effective range for the $\Lambda_c N$ system.

m_π	$^1S_0$ channel	$^3S_1$ channel
412(2) MeV	5.59 (1.24) fm	5.33 (0.96) fm
570(1) MeV	6.02 (3.37) fm	5.16 (2.34) fm
702(2) MeV	11.6 (11.3) fm	6.92 (4.45) fm

and $^3S_1$ channel are almost identical within the statistical errors, which suggest that the $\Lambda_c N$ interaction is almost spin-independent at low energies. In order to investigate the spin-independency, we calculate the low-energy parameters by only using the spin-independent central potential $V_0(r)$ and compare with the values in Tables 5.5 and 5.6, which are shown in Fig. 5.10. The figure suggests that the spin-independent central potential well reproduces $\Lambda_c N$ interaction.

We have discussed the interpretations for the weak strength of both the tensor potential and the spin-spin potential from the point of view of the meson exchange interactions in secs. 5.2.4 and 5.2.5. In another point of view, the similarity of the $\Lambda_c N$ phase shifts in $^1S_0$ and $^3S_1$ may be understood by the heavy quark spin symmetry [62], which is fundamental symmetry of the heavy quark in QCD. First, in the heavy quark limit, the spin of the heavy quark can be considered as the conserved quantity and decouples from the total spin of other components made of light quarks and gluons. In this situation, a heavy hadron system including one heavy quark with total angular momentum J can be interpreted as $|[\mathrm{L}]_j Q\rangle_J$, where Q is a heavy quark and $[\mathrm{L}]_j$ stands for the light components of the heavy

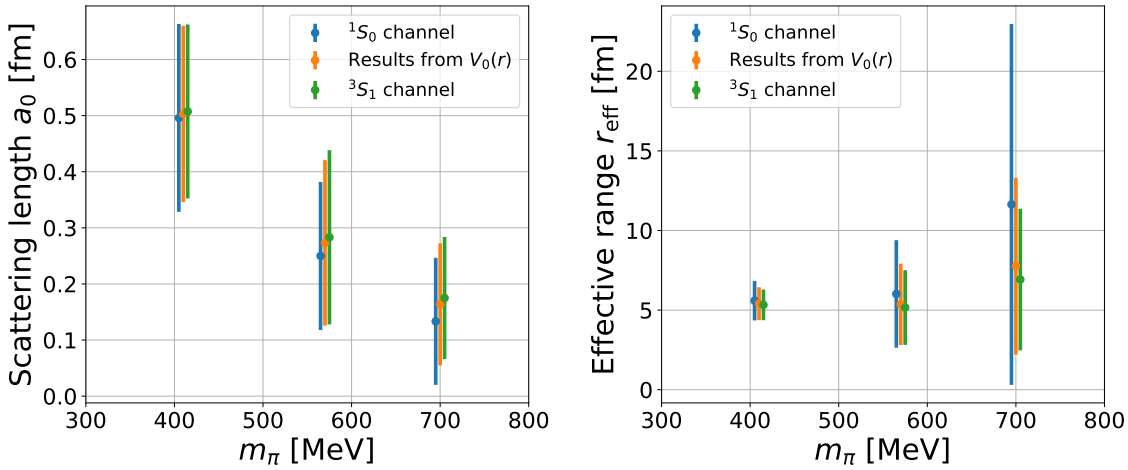

Figure 5.10: Scattering lengths (Left figure) and effective ranges (Right figure) for the $\Lambda_c N$ system. These values are calculated by using the central potential in $^1S_0$ channel, the central potential in $^3S_1$ channel and the spin-independent central potential $V_0(r)$. For the scattering lengths, we employ the particle physics convention for the definition of scattering length which has opposite sign from the historical sign convention of the baryon-baryon interaction.

hadron system with total spin j. Since the total angular momentum is conserved, the total spin of light components is also conserved in heavy quark mass limit. The compound state in $J = j + 1/2$ and $J = j - 1/2$ channel are degenerated because the spin direction of the heavy quark is irrelevant to the total energy in the heavy quark mass limit. This consideration can be applied to not only a single heavy hadron but also multi-hadron systems with a heavy quark [63]. In the case of the two baryon system with single charm quark in total angular momentum $J = 0$, the total spin of light-components should be $j = 1/2$, which degenerates with the system in total angular momentum $J = 1$ in the heavy quark mass limit. Next, in a finite volume, an energy eigenstate has a discrete total energy. When we denote the total energy for the n-th energy eigenstate in $J = 0$ ($J = 1$) as W_n ($\tilde{W}_n$), the NBS wave function with the total energy W_n ($\tilde{W}_n$) is defined in Eq.(3.1), denoted by $\psi^{W_n}_{J=0}$ ($\psi^{\tilde{W}_n}_{J=1}$). A plausible assumption that the heavy quark spin symmetry holds also in the finite volume leads to $W_n = \tilde{W}_n$, which implies that the phase shifts for $J = 0$ and $J = 1$ states agree at $W_n = \tilde{W}_n$, according to Lüscher's finite volume formula [20]. Since this argument holds for an arbitrary volume, the scattering phase shifts agree between $J = 0$ and $J = 1$ states at all energy below the inelastic threshold. Note that the breaking of the heavy quark symmetry due to the heavy but finite charm quark mass

generates a small spin-dependent in the phase shifts and scattering lengths.

We finally discuss the differences between values of physical observables calculated from the potentials constructed with Misner's method and those in Ref. [23] in which the observables are calculated from the conventional HAL QCD potential constructed from the A_1^+ projected R-correlator data. The comparisons of scattering lengths with

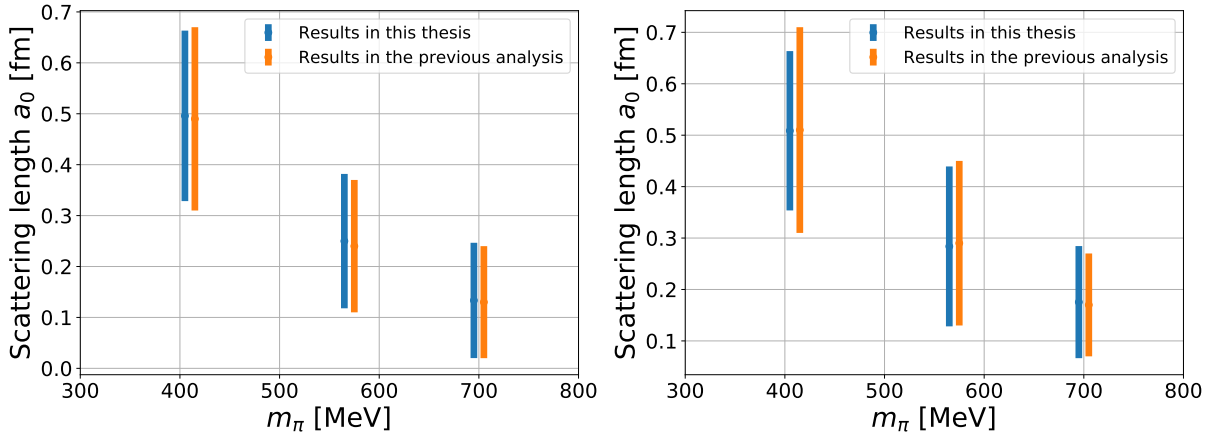

Figure 5.11: Comparisons of the scattering lengths in ${}^1S_0$ channel (Left figure) and ${}^3S_1$ channel (Right figure) for the $\Lambda_c N$ system. For the scattering lengths, we employ the particle physics convention for the definition of scattering length which has opposite sign from the historical sign convention of the baryon-baryon interaction.

the conventional calculation are given in Fig. 5.11, which show consistent results within statistical errors. This suggests that the potential fitting reproduces the $L = 0$ component well although the higher partial wave contributions are included. Note that since the fit-range of the potentials is different between the analysis in this section and in Ref. [23], there may exist systematic errors in the values of scattering lengths due to this difference.

5.3 Inelastic scattering in $\Lambda_c N$ system and $\Sigma_c N$ interaction in $I = 1/2$ channel

As we discussed in Sec. 3.2.1, the non-locality of the $\Lambda_c N$ single channel potential may become sizable when the energy approaches an inelastic threshold, that is the $\Sigma_c N$ threshold. In this section, we calculate the coupled channel potential for $\Lambda_c N$-$\Sigma_c N$ system to investigate inelastic scattering effects. Furthermore, from the coupled channel potential, we can also study interactions for the $\Sigma_c N$ system with the isospin $I = 1/2$. The NBS wave

function for the $\Sigma_c N$ system in $I = 1/2$ channel is obtained by the following projection:

$$\psi_{\Sigma_c N(I=1/2)}(\vec{x}) = \sqrt{\frac{1}{3}}\psi_{\Sigma_c^+ p}(\vec{x}) - \sqrt{\frac{2}{3}}\psi_{\Sigma_c^{++} n}(\vec{x}). \tag{5.6}$$

The discussion in this section is based on Refs. [24, 25].

5.3.1 Coupled channel potential for $\Lambda_c N$-$\Sigma_c N$ system in $^1S_0$ channel

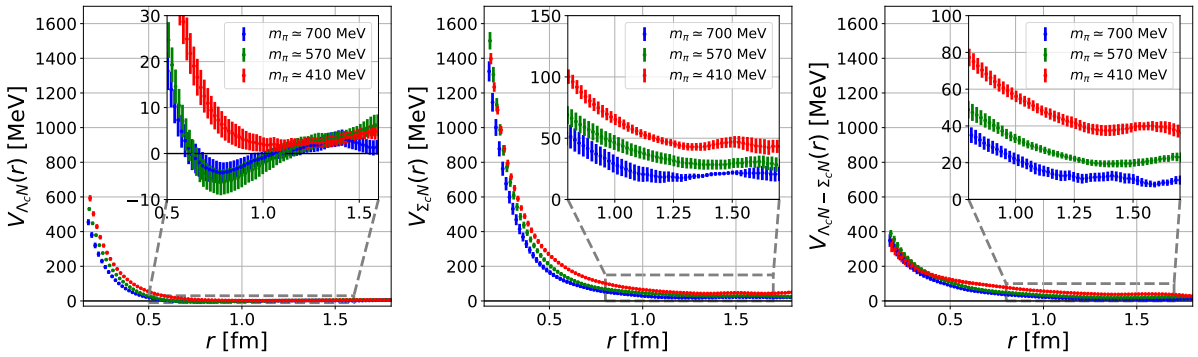

Figure 5.12: The $\Lambda_c N$-$\Sigma_c N$ coupled channel potential in $^1S_0$ channel. The potentials are calculated at $t - t_0 = 13$ for $m_\pi \simeq 700$ MeV case (Blue), $t - t_0 = 11$ for $m_\pi \simeq 570$ MeV case (Green) and $t - t_0 = 9$ for $m_\pi \simeq 410$ MeV case (Red). Left and middle figures correspond to the diagonal potentials for the $\Lambda_c N$ and the $\Sigma_c N$ channels, and the right figure shows the averaged off-diagonal potential.

We first show the coupled channel potential for the $\Lambda_c N$-$\Sigma_c N$ system in $^1S_0$ channel. The potentials are calculated by time-dependent HAL QCD method for the coupled channel potential presented in Sec. 3.2.3. We employ Misner's method to extract the $L = 0$ component of the NBS wave function for each Jackknife sample. For Misner's method, we employ the parameters $\Delta, n_{\max}$, and $l_{\max}$ as a (lattice spacing) , 3, and 5, respectively. We calculate each R in unit of $0.2a$ from $2a$ to $20a$ for radial coordinates of the spherical harmonics amplitude, so that some data are repeatedly used to calculate the spherical harmonics amplitude. The numerical results are shown in Fig. 5.12. The potentials are calculated at $t-t_0 = 13$ (Ensemble 1: $m_\pi \simeq 700$ MeV), $t-t_0 = 11$ (Ensemble 2: $m_\pi \simeq 570$ MeV) and $t - t_0 = 9$ (Ensemble 3: $m_\pi \simeq 410$ MeV).

From the results, we find that the tail of the potentials deviates from the zero (especially in the $\Sigma_c N$ potential and off-diagonal potential). Furthermore, we observe that the

time-dependence of the potentials is still large. These observations suggest that the time-separation between the source operator and the sink operator $(t - t_0)$ is not large enough so that the inelastic states cannot be negligible. When we take more large $t - t_0$, we need more large statistics because the statistical errors increase for large $t - t_0$. However, we cannot have further statistics due to the limited number of the gauge configurations in our numerical setup. In the future calculation, we should employ a more large number of gauge configurations to investigate the $\Lambda_c N$-$\Sigma_c N$ system in ${}^1S_0$ channel.

5.3.2 Coupled channel potential for $\Lambda_c N$-$\Sigma_c N$ system in ${}^3S_1 - {}^3D_1$ channel

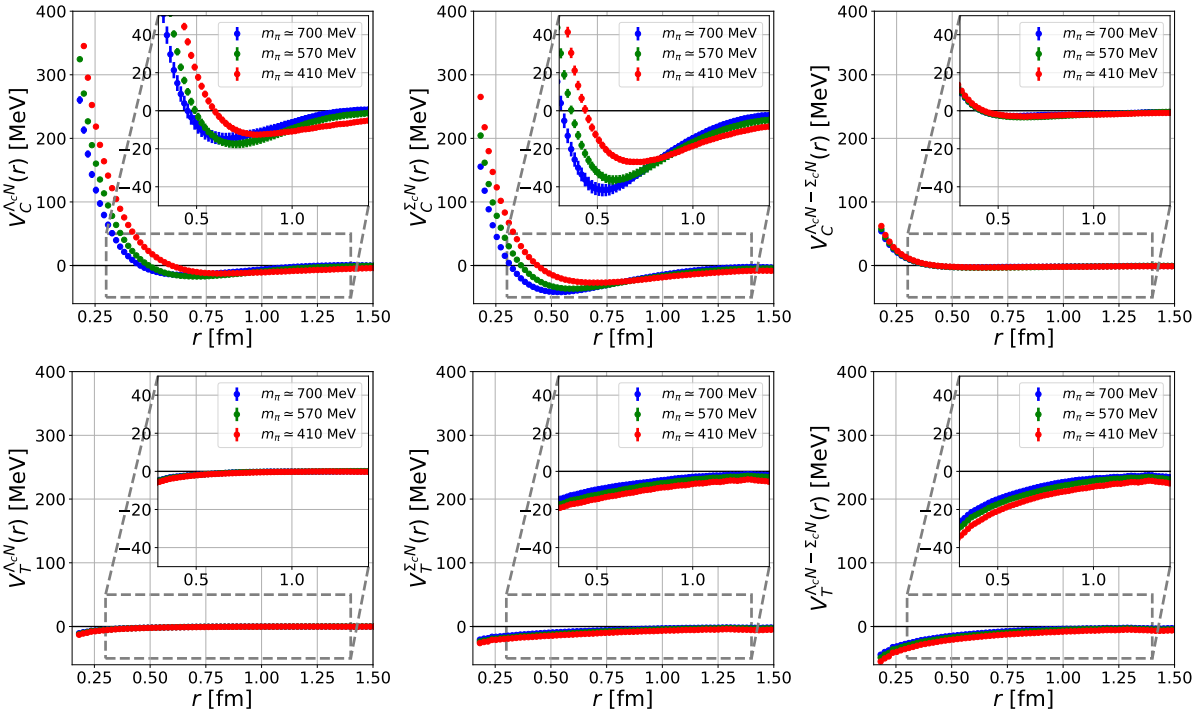

Figure 5.13: The coupled channel potential for the $\Lambda_c N$-$\Sigma_c N$ system in ${}^3S_1 - {}^3D_1$ channel. Upper three figures show the central potentials while the lower three figures show the tensor potentials for each component. The potentials are calculated at $t - t_0 = 13$ for $m_\pi \simeq 700$ MeV case (Blue), $t - t_0 = 11$ for $m_\pi \simeq 570$ MeV case (Green) and $t - t_0 = 9$ for $m_\pi \simeq 410$ MeV case (Red). Left and middle figures correspond to the diagonal potentials for the $\Lambda_c N$ and the $\Sigma_c N$ channels, and the right figure shows the averaged off-diagonal potential.

We next show the coupled channel potential for the $\Lambda_c N$-$\Sigma_c N$ system in ${}^3S_1 - {}^3D_1$

channel. The potentials are calculated by time-dependent HAL QCD method with Misner's method as in the previous subsection. In order to calculate both central and tensor potentials, we combine Eqs. (3.37) and (3.72). Fig. 5.13 shows the numerical results of the potentials calculated at $t - t_0 = 13$ (Ensemble 1: $m_\pi \simeq 700$ MeV), $t - t_0 = 11$ (Ensemble 2: $m_\pi \simeq 570$ MeV) and $t - t_0 = 9$ (Ensemble 3: $m_\pi \simeq 410$ MeV). These potentials are confirmed that they are stable against the change of $t - t_0$ within the statistical errors, which indicates that the inelastic contributions from channels other than the $\Lambda_c N$ and the $\Sigma_c N$ can be neglected. In the figures, we write $V_C^{\Lambda_c N}$, $V_T^{\Lambda_c N}$, $V_C^{\Sigma_c N}$, $V_T^{\Sigma_c N}$, $V_C^{\Lambda_c N - \Sigma_c N}$, and $V_T^{\Lambda_c N - \Sigma_c N}$ as $\Lambda_c N$ central potential, $\Lambda_c N$ tensor potential, $\Sigma_c N$ central potential, $\Sigma_c N$ tensor potential, off-diagonal (transition) central potential, and off-diagonal (transition) tensor potential, respectively.

From the results, we observe that the central potentials for $\Lambda_c N$ channel ($V_C^{\Lambda_c N}$) are almost identical to the $\Lambda_c N$ potentials in the single channel analysis (i.e. the potentials in Fig. 5.6) within the statistical errors. We also find a strong attraction in the $\Sigma_c N$ central potential. Fig. 5.14 shows the comparison between the $\Sigma_c N$ and ΣN central potential for

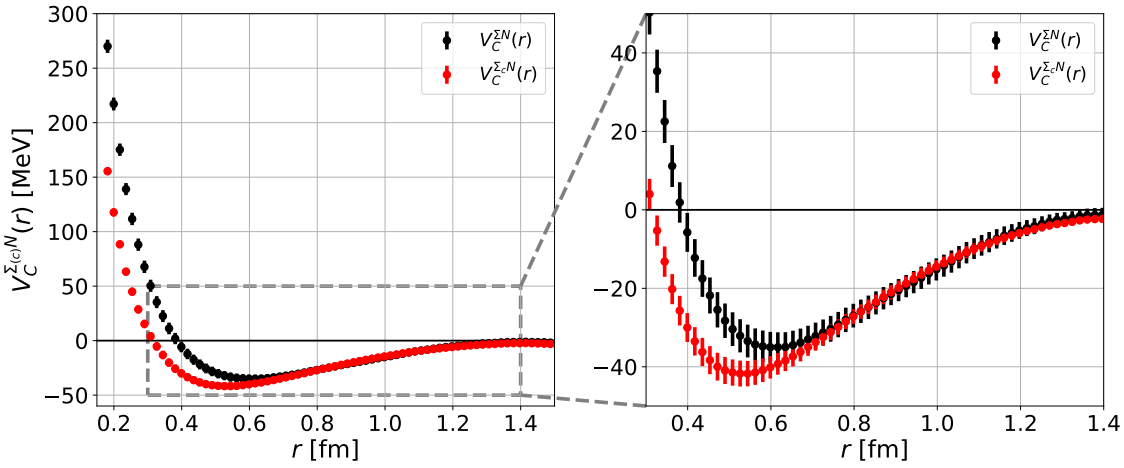

Figure 5.14: The comparison between the central potential for the $\Sigma_c N$ channel and the ΣN channel in the ${}^3S_1$ channel. The potentials are calculated at $t - t_0 = 13$ for $m_\pi \simeq 700$ MeV case.

$m_\pi \simeq 700$ MeV case. The figure shows the tails of these potentials are comparable, which might be a manifestation of the one-pion-exchange. Furthermore, we observe that the height of the repulsive core in the $\Sigma_c N$ potential is smaller than that in the ΣN potential. As the result, the region of the attraction in $\Sigma_c N$ potential is extended. This motivates us to search the $\Sigma_c N$ two-body bound state. For the off-diagonal (transition) potential, we

find that the central potential ($V_C^{\Lambda_c N - \Sigma_c N}$) is negligibly weak while the tensor potential ($V_T^{\Lambda_c N - \Sigma_c N}$) is strong. This suggests that if there exists a would-be $\Sigma_c N$ bound state, it becomes a resonance in the D-wave $\Lambda_c N$ state through the strong transition tensor potential.

5.3.3 Phase shifts for the $\Lambda_c N$ and the $\Sigma_c N$ channel in $^3S_1 - ^3D_1$ channel

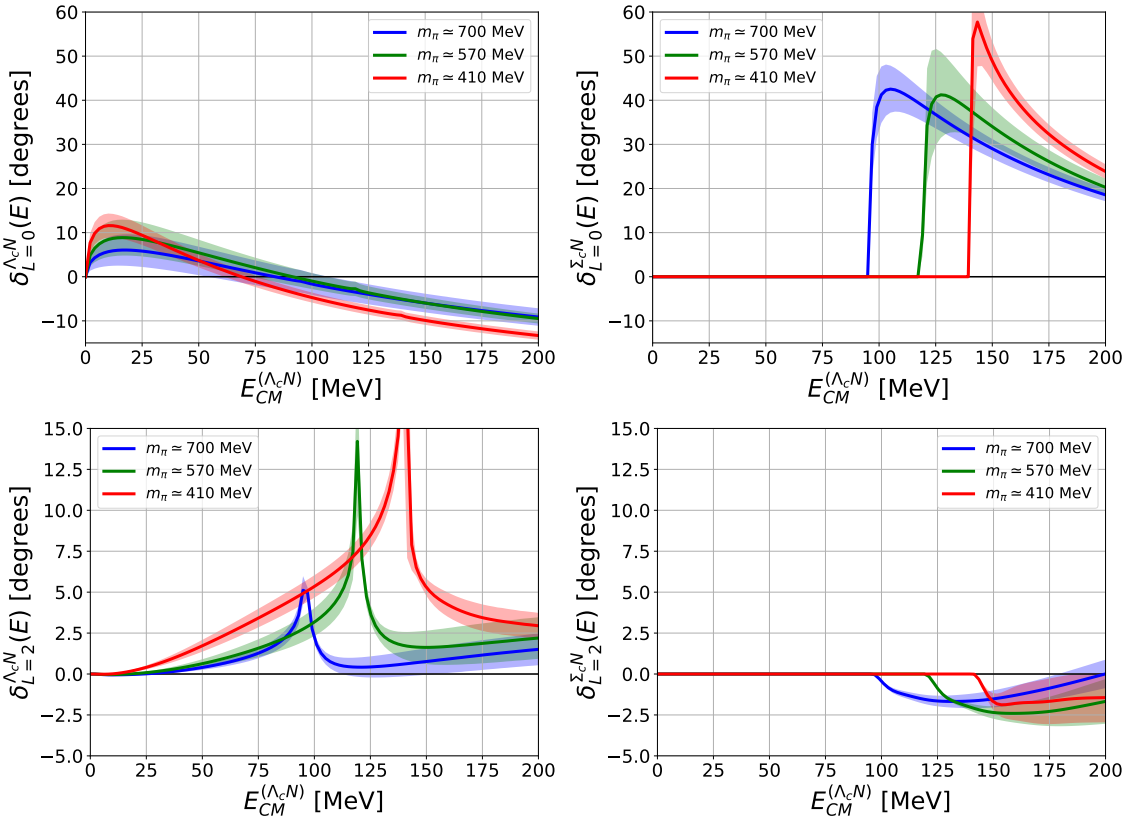

Figure 5.15: The phase shifts of S-wave $\Lambda_c N$ system (Upper left figure), S-wave $\Sigma_c N$ system (Upper right figure), D-wave $\Lambda_c N$ system (Lower left figure), D-wave $\Sigma_c N$ system (Lower right figure) for each pion mass case. The phase shift is defined as Eq. (5.8).

We then calculate physical observables such as scattering phase shifts from the potentials. For this purpose, we fit the potential data with the functional form defined in Eq. (5.3) for the $\Lambda_c N$ central potentials, while the $\Sigma_c N$ central potentials and the

off-diagonal central potentials are fitted with the following functional form:

$$V_{C;\mathrm{fit}}(r) = a_1 e^{-\left(\frac{r}{a_2}\right)^2} + a_3 e^{-\left(\frac{r}{a_4}\right)^2} + a_5 \left(1 - e^{-a_6 r^2}\right) \frac{e^{-a_7 r}}{r}, \tag{5.7}$$

where the third term is employed by respecting the fact that the long-range attraction in the $\Sigma_c N$ system is caused by the one-pion-exchange. For the tensor potentials, we employ the fit-function defined in Eq. (5.4). We use the potential data at $r \in [2a, 16a]$ fm for the fitting.

Using the fitted potentials, we solve the coupled channel Schrödinger equation by the finite difference method and calculate the S-matrix from an asymptotic behavior of wave functions. From the obtained S-matrix, we define the phase shifts for the coupled channel system as:

$$\delta_j(k) \equiv \frac{1}{2i} \log \left(\frac{S_{jj}}{|S_{jj}|} \right), \tag{5.8}$$

where j represents an index for the channel.

Fig. 5.15 shows the phase shifts of each channel. From the figures, we first find that there are no bound states for both $\Lambda_c N$ and $\Sigma_c N$ channels at all pion masses, even though the attraction of the S-wave $\Sigma_c N$ system at low energies is rather strong. In the results of the D-wave $\Lambda_c N$ phase shift, we observe a cusp-like structure around the $\Sigma_c N$ threshold, which is induced by the strong transition tensor potential. On the other hand, there exist no such a structure in the S-wave $\Lambda_c N$ phase shift, which suggests that the strong attraction in the S-wave $\Sigma_c N$ interaction does not affect the S-wave $\Lambda_c N$ interaction. This observation is understood from the weak off-diagonal part of the central potential ($V_C^{\Lambda_c N - \Sigma_c N}$).

5.3.4 Non-locality of the single channel $\Lambda_c N$ potential

In order to investigate the non-locality of the single channel potential calculated in Sec. 5.2.4, we compare the phase shifts for the $\Lambda_c N$ system (Left two figures in Fig. 5.15) with those calculated in the single channel analysis (i.e. Fig. 5.9). The results of the comparison are given in Fig. 5.16. From the upper three figures, we find that the S-wave phase shifts in the single channel analysis and coupled channel analysis are almost identical, which imply that the non-locality of the $\Lambda_c N$ central potential in the single channel analysis is small. Furthermore, we observe that these phase shifts are almost the same

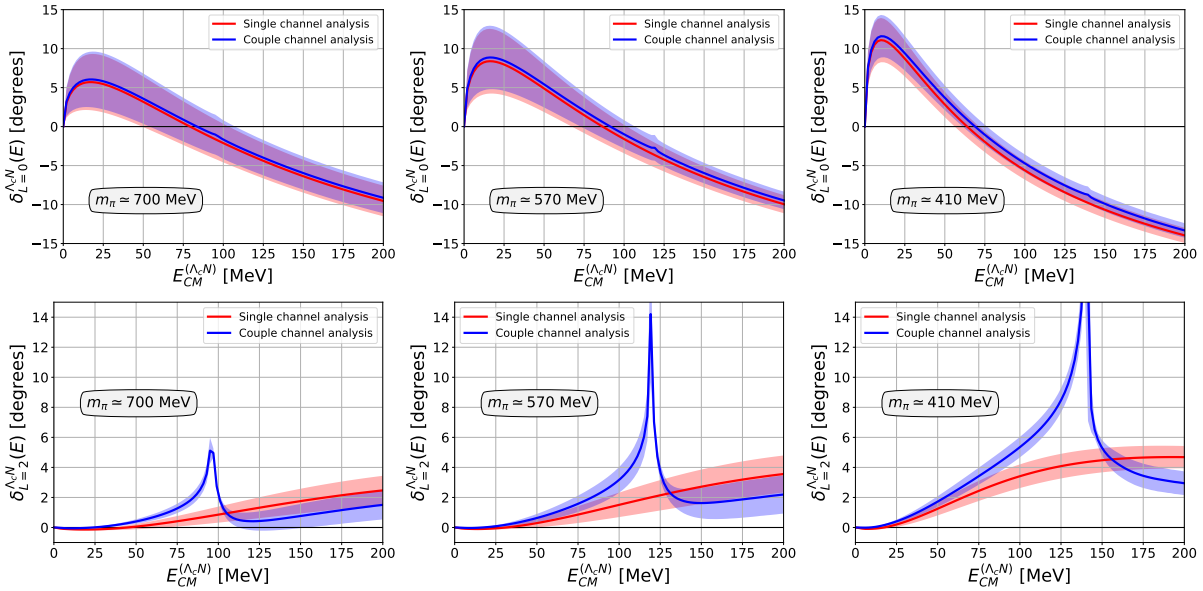

Figure 5.16: Comparisons of the $\Lambda_c N$ phase shifts calculated from single channel potential (Red) and coupled channel potential (Blue).

even above the $\Sigma_c N$ threshold. This observation suggests that the S-wave $\Lambda_c N$ system is almost decoupled from the $\Sigma_c N$ system. In the lower figures, on the other hand, we find that the D-wave phase shifts are different around the $\Sigma_c N$ threshold although these are almost identical in the low-energies. This implies that the non-locality of the $\Lambda_c N$ tensor potential in the single channel analysis is large near and above the $\Sigma_c N$ threshold.

5.4 $\Xi_{cc}N$ interaction in $I = 0$ channel

The Ξ_{cc} baryon is a doubly charmed baryon whose spin-isospin is $J(I) = 1/2\ (1/2)$. Recently, the Ξ_{cc}^{++} baryon has been found in the LHCb experiment [19] and the mass is estimated as $m_{\Xi_{cc}^{++}} \simeq 3621$ MeV.

In this section, we present the 2-body interaction between Ξ_{cc} baryon and a nucleon in spin-isospin $J(I) = 0(0)$ channel. Since this system couples to spin-singlet $\Lambda_c\Lambda_c$ system, we should consider the coupled channel system for $\Xi_{cc}N - \Lambda_c\Lambda_c$.

The $\Xi_{cc}N$ system with spin-isospin $J(I) = 0(0)$ is interesting because this system relates to the charm version of the H-dibaryon. The H-dibaryon is a candidate of the six-quark ($uuddss$) exotic state in a spin and isospin singlet state first proposed by Jaffe [64]. In the recent work in the HAL QCD Collaboration [74], we found that the strength

of ΞN attraction is key to clarify the fate of H-dibaryon in nature. As a natural extension, the investigation of the $\Xi_{cc}N$ interaction is important to study the charm version of the H-dibaryon.

In order to construct the $\Lambda_c\Lambda_c$-$\Xi_{cc}N(I = 0)$ coupled channel potential, we calculate the NBS wave function for the $\Xi_{cc}N$ system in $I = 0$ channel obtained by the following projection:

$$\psi_{\Xi_{cc}N(I=0)}(\vec{x}) = \sqrt{\frac{1}{2}}\psi_{\Xi^+_{cc}p}(\vec{x}) - \sqrt{\frac{1}{2}}\psi_{\Xi^{++}_{cc}n}(\vec{x}). \tag{5.9}$$

5.4.1 Coupled channel potential for $\Lambda_c\Lambda_c$-$\Xi_{cc}N$ system in $^1S_0$ channel

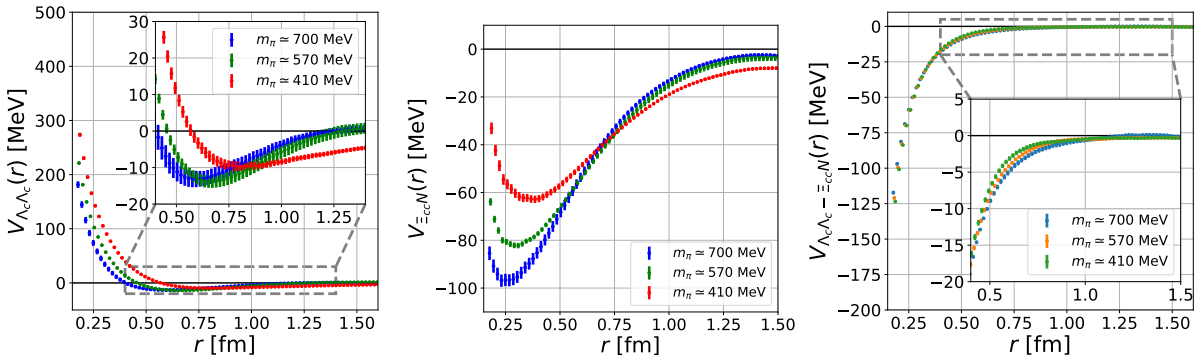

Figure 5.17: The $\Lambda_c\Lambda_c$-$\Xi_{cc}N(I = 0)$ coupled channel potential in $^1S_0$ channel. The potentials are calculated at $t - t_0 = 13$ for $m_\pi \simeq 700$ MeV case (Blue), $t - t_0 = 11$ for $m_\pi \simeq 570$ MeV case (Green) and $t - t_0 = 9$ for $m_\pi \simeq 410$ MeV case (Red). Left and middle figures correspond to the diagonal potentials for the $\Lambda_c\Lambda_c$ and the $\Xi_{cc}N(I = 0)$ channels, and right figure shows the averaged off-diagonal potential.

We show the coupled channel potential for the $\Lambda_c\Lambda_c$-$\Xi_{cc}N(I = 0)$ system in $^1S_0$ channel. The potentials are calculated by time-dependent HAL QCD method for the coupled channel potential presented in Sec. 3.2.3. We employ Misner's method to extract the $L = 0$ component of the NBS wave function for each Jackknife sample with the parameters $\Delta = a$ (lattice spacing), $n_{\max} = 3$, and $l_{\max} = 5$. We calculate each R in unit of $0.2a$ from $2a$ to $16a$ for the radial coordinate of the spherical harmonics amplitude, so that some data are repeatedly used to calculate the spherical harmonics amplitude. The numerical results are shown in Fig. 5.17. The potentials are calculated at $t - t_0 = 13$ (Ensemble 1: $m_\pi \simeq 700$ MeV), $t - t_0 = 11$ (Ensemble 2: $m_\pi \simeq 570$ MeV) and $t - t_0 = 9$

(Ensemble 3: $m_\pi \simeq 410$ MeV). We confirm that their potentials are stable against the change of $t - t_0$ within the statistical errors, which indicates that inelastic contributions from channels other than the $\Lambda_c\Lambda_c$ and the $\Xi_{cc}N$ can be neglected.

From the results, we find the strong attraction in the $\Xi_{cc}N(I = 0)$ potential, while the attraction $\Lambda_c\Lambda_c$ is weak. We also observe the interaction range of the off-diagonal potentials is short. The shot interaction range of the off-diagonal potentials is understood from the following fact. The transition between $\Lambda_c\Lambda_c$ and $\Xi_{cc}N(I = 0)$ is induced by a charm quark exchange. Since the charm quark is heavy, this contribution is suppressed in long-distances.

5.4.2 Phase shifts for the $\Lambda_c\Lambda_c$ and the $\Xi_{cc}N(I = 0)$ system in $^1S_0$ channel

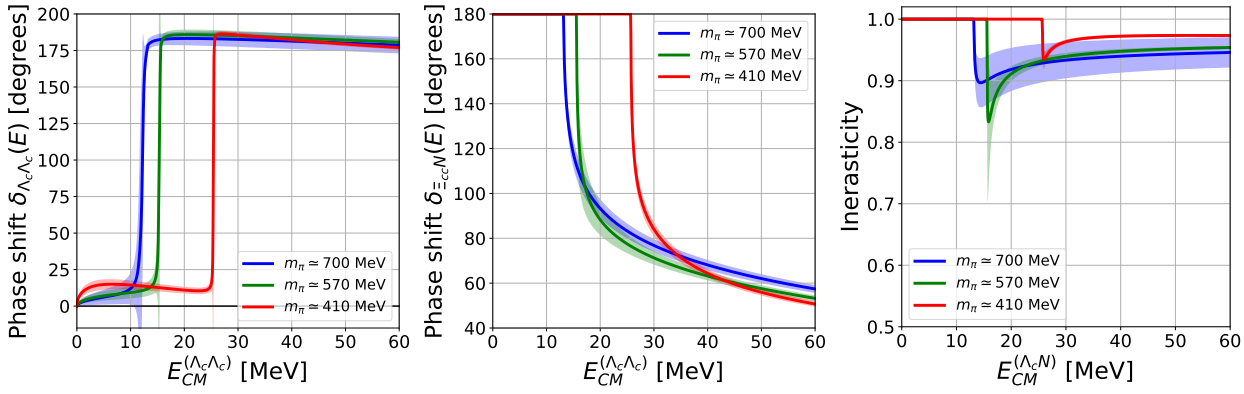

Figure 5.18: The phase shifts of S-wave $\Lambda_c\Lambda_c$ system (Left figure), S-wave $\Xi_{cc}N(I = 0)$ system (Middle figure) and the inelasticity defined as $|S_{\Lambda_c\Lambda_c}|$ (Right figure) for each pion mass case. The phase shifts are defined as Eq. (5.10).

We next calculate the scattering phase shifts from the potentials. For this purpose, we fit the potential data with the functional form defined in Eq. (5.3) for the $\Lambda_c\Lambda_c$ central potentials, while the $\Xi_{cc}N(I = 0)$ central potentials and the off-diagonal central potentials are fitted with the functional form defined in Eq. (5.7). We use the potential data at $r \in [2a, 16a]$ fm for the fitting.

Using the fitted potentials, we solve the coupled channel Schrödinger equation by the finite difference method and calculate the S-matrix from an asymptotic behavior of wave functions. From the obtained S-matrix, we define the phase shifts for the coupled channel

system as

$$\begin{pmatrix} S_{\Lambda_c\Lambda_c,\Lambda_c\Lambda_c} & S_{\Lambda_c\Lambda_c,\Xi_{cc}N} \\ S_{\Xi_{cc}N,\Lambda_c\Lambda_c} & S_{\Xi_{cc}N,\Xi_{cc}N} \end{pmatrix} \equiv \begin{pmatrix} e^{i\bar{\delta}_{\Lambda_c\Lambda_c}} & 0 \\ 0 & e^{i\bar{\delta}_{\Xi_{cc}N}} \end{pmatrix} \begin{pmatrix} \cos 2\bar{\theta} & i\sin 2\bar{\theta} \\ i\sin 2\bar{\theta} & \cos 2\bar{\theta} \end{pmatrix} \begin{pmatrix} e^{i\bar{\delta}_{\Lambda_c\Lambda_c}} & 0 \\ 0 & e^{i\bar{\delta}_{\Xi_{cc}N}} \end{pmatrix}, \tag{5.10}$$

where $\bar{\delta}$ is so-called the bar phase shift and $\bar{\theta}$ is the mixing angle proposed in Ref. [66].

We show the numerical results for the phase shift of each channel and inelasticity defined as $|S_{\Lambda_c\Lambda_c,\Lambda_c\Lambda_c}| = \cos 2\bar{\theta}$ in Fig. 5.18. The inelasticity corresponds to the strength of the transition between $\Lambda_c\Lambda_c$ and $\Xi_{cc}N(I = 0)$. From these figures, we find the $\Lambda_c\Lambda_c$ phase shift cut through 90° below the $\Xi_{cc}N(I = 0)$ threshold, which corresponds to the resonance state. This resonance state is induced by strong $\Xi_{cc}N(I = 0)$ attraction and transition between $\Lambda_c\Lambda_c$ and $\Xi_{cc}N(I = 0)$. The sharpness of the resonance indicates the strength of the transition is weak. This weak transition between $\Lambda_c\Lambda_c$ and $\Xi_{cc}N(I = 0)$ is also seen as small deviations of inelasticity from unity in Fig. 5.18.

Finally, we discuss the fate of the charm version H-dibaryon in nature. In the physical mass, the threshold of $\Lambda_c\Lambda_c$ ($m_{\Lambda_c\Lambda_c} \simeq 4570$) is just above the $\Xi_{cc}N$ threshold ($m_{\Xi_{cc}N(I=0)} \simeq 4560$), so that the $\Xi_{cc}N(I = 0)$ is the ground state for the two baryon system with two charm quarks in $J(I) = 0(0)$ channel. Therefore, if the $\Xi_{cc}N(I = 0)$ attraction is sufficiently strong, the charm version of H-dibaryon appears as a bound state in the system. Our numerical results support this assumption that the $\Xi_{cc}N(I = 0)$ attraction is sufficiently strong to form the bound state.

Chapter 6

Λ_c hypernuclei from HAL QCD potential

Since the $\Lambda_c N$ interaction is dominated by the spin-independent central force, as we discussed in the previous chapter, the spectrum of Λ_c hypernuclei, if they exist, would be simple. In order to investigate Λ_c hypernuclei, we employ the single-folding potential which is an S-wave effective potential between a single particle and spherical nuclei. We construct the folding potential from the lattice potential and discuss the possible Λ_c hypernuclei including the effects of Coulomb repulsion.

6.1 Single-folding potential

The single-folding potential for Λ_c hypernuclei is defined by

$$V_F(\vec{r}) = \int d^3r' \rho_A(\vec{r'}) V_{\Lambda_c N}(\vec{r} - \vec{r'}), \tag{6.1}$$

where $\rho_A(\vec{r})$ denotes nuclear density distributions with the atomic number A. Since the $\Lambda_c N$ interaction is dominated by the spin-independent central force, we take $V_{\Lambda_c N}(\vec{r}) = V_0(\vec{r})$.

For the nuclear density distribution function, we use the two-parameter Fermi form given by

$$\rho_A(\vec{r}) = \rho_0 \left[1 + \exp\left(\frac{r-c}{a}\right)\right]^{-1}, \qquad \int d^3r \ \rho_A(\vec{r}) = A, \tag{6.2}$$

where $r \equiv |\vec{r}|$. We employ the parameters ρ_0, c, a given in Ref. [67] for spherical nuclei such as ^{12}C, ^{28}Si, ^{40}Ca, ^{58}Ni, ^{90}Zr, and ^{208}Pb, which are determined from the electron-nucleus elastic scattering experiments. Strictly speaking, the nuclear density distributions are deformed by the interaction with Λ_c baryon. We assume, however, the deformation is negligible because the $\Lambda_c N$ interaction is weak. Fig. 6.1 shows the nuclear density

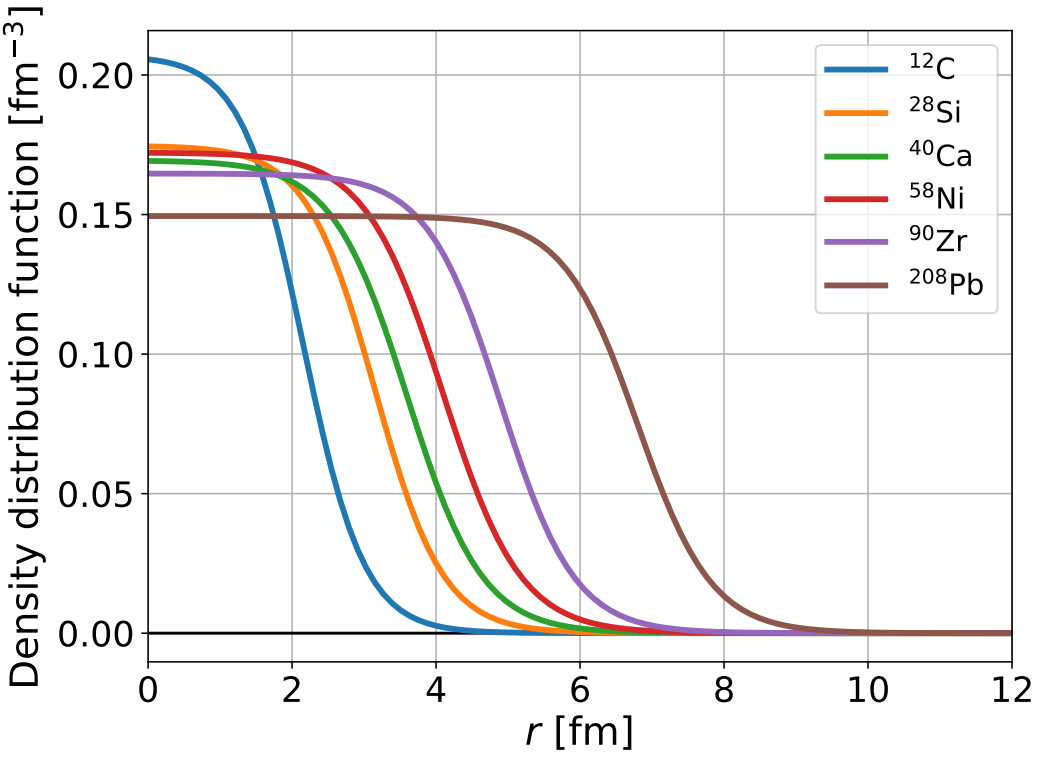

Figure 6.1: Nuclear density distribution functions defined in Eq. (6.2).

distribution functions $\rho_A(r)$ we used in this thesis.

Fig. 6.2 shows the folding potential for Λ_c-^{208}Pb for each ensemble. We observe that the folding potential becomes deeper as the u, d quark masses decrease and becomes as large as -10 to -20 MeV at the origin. This observation is the consequence of the fact that the $\Lambda_c N$ two-body interaction becomes more attractive as the u, d quark masses decrease.

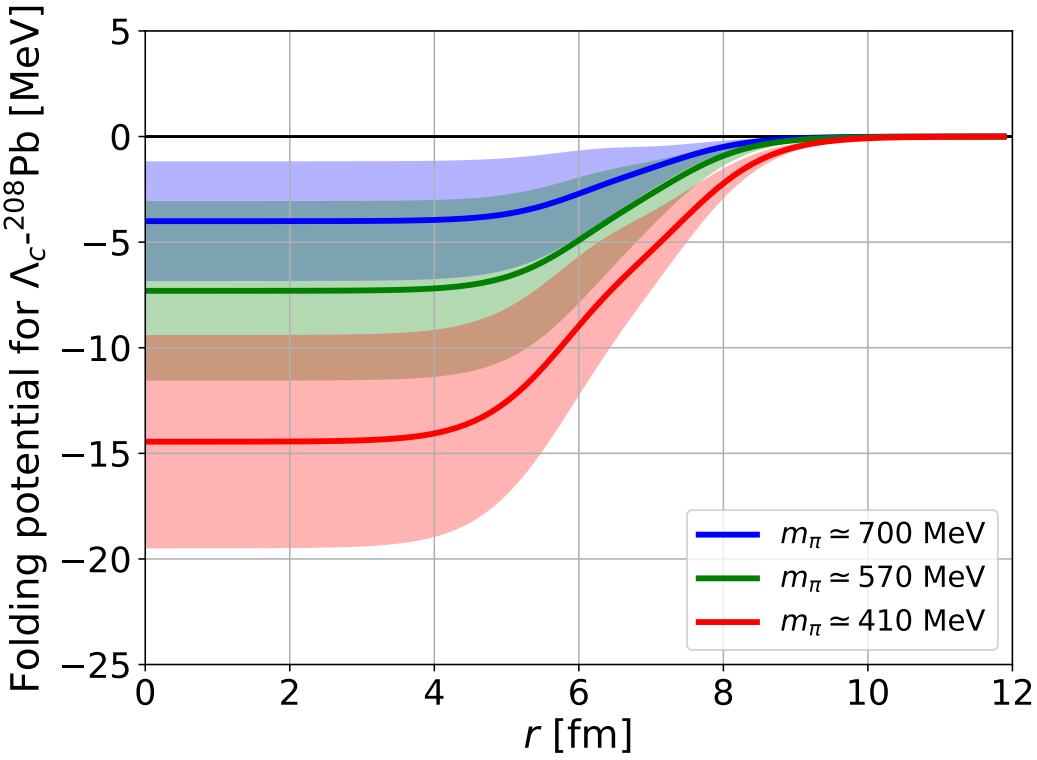

Figure 6.2: Λ_c-^{208}Pb folding potentials calculated from the spin-independent central potential of the $\Lambda_c N$ system (Fig. 5.7) for $m_\pi \simeq 700$, 570, and 410 MeV cases.

6.2 Gaussian expansion method

Using this folding potential, we calculate the binding energy of the Λ_c hypernuclei by the Gaussian expansion method [68] for the S-wave potential, with the physical masses for Λ_c and nuclei. We briefly explain the Gaussian expansion method in this section.

We start from the Schrödinger equation for two particle system with the reduced mass μ:

$$(H_0 + V(\vec{r}))\,\psi_n(\vec{r}) \;=\; E_n\psi_n(\vec{r}) \qquad H_0 = -\frac{\vec{\nabla}^2}{2\mu}. \tag{6.3}$$

We then expand the wave function $\psi_n(\vec{r})$ using some Gaussian functions as

$$\psi_n(\vec{r}) \;=\; \sum_{i=1}^{N}\sum_{l,m} c_{n,l,m,i}\;\phi^G_{l,i}(r)\;Y_{l,m}(\hat{\vec{r}}), \tag{6.4}$$

$$\phi^G_{l,i}(r) = r^l \exp\left[-\left(\frac{r}{\nu_i}\right)^2\right], \tag{6.5}$$

where $\hat{\vec{r}} = (\theta, \phi)$, $Y_{l,m}(\hat{\vec{r}})$ is a spherical harmonic function, and $c_{n,l,m,i}$ stands for a coefficient for expansion. The range of the Gaussian ν_i is determined by $\nu_i = r_0 a^{i-1}$ with arbitrary constants r_0 and a. In the case of S-wave, we obtain the following generalized eigenvalue problem by multiplying a Gaussian function (Eq. (6.5)) from the left in Eq. (6.3) and carry out the integration for $\vec{r}$.

$$H^G \, \vec{C}_n = E_n \, \Phi^G \, \vec{C}_n, \tag{6.6}$$

where $\vec{C}_n$ is an N dimensional vector and H^G, Φ^G are $N \times N$ matrices, which are defined as

$$\vec{C}_n \equiv \begin{pmatrix} c_{n,1} \\ c_{n,2} \\ \vdots \\ c_{n,N} \end{pmatrix}, \tag{6.7}$$

$$\left[H^G\right]_{ij} \equiv \int d^3r \; \phi^G_i(r) H^G_j(\vec{r}) \phi^G_j(r), \tag{6.8}$$

$$\left[\Phi^G\right]_{ij} \equiv \int d^3r \; \phi^G_i(r) \phi^G_j(r), \tag{6.9}$$

$$\phi^G_i(r) \equiv \exp\left[-\left(\frac{r}{\nu_i}\right)^2\right], \tag{6.10}$$

$$H^G_j(\vec{r}) \equiv \frac{1}{\mu \nu_j^2}\left(3 - \frac{2r^2}{\nu_j^2}\right) + V(\vec{r}). \tag{6.11}$$

Except for the potential term, the explicit form of the H^G and the Φ^G are given by

$$\left[\Phi^G\right]_{ij} = \left(\frac{\pi \nu_i^2 \nu_j^2}{\nu_i^2 + \nu_j^2}\right)^{3/2}, \tag{6.12}$$

$$\left[H^G\right]_{ij} = \frac{3}{\mu\left(\nu_i^2 + \nu_j^2\right)}\left(\frac{\pi \nu_i^2 \nu_j^2}{\nu_i^2 + \nu_j^2}\right)^{3/2} + \left[V^G\right]_{ij}, \tag{6.13}$$

where $[V^G]_{ij}$ is defined as

$$[V^G]_{ij} \equiv \int d^3r \ \exp\left[-\left(\frac{r}{\nu_i}\right)^2\right] V(\vec{r}) \exp\left[-\left(\frac{r}{\nu_j}\right)^2\right]. \tag{6.14}$$

The binding energies, as well as the wave functions for the two body system, can be obtained by solving Eq. (6.6) with sufficiently large N and plausible r_0 and a. The parameters N, r_0, and a can be determined so as to minimize the binding energies.

6.3 Numerical results of the binding energy for Λ_c hypernuclei

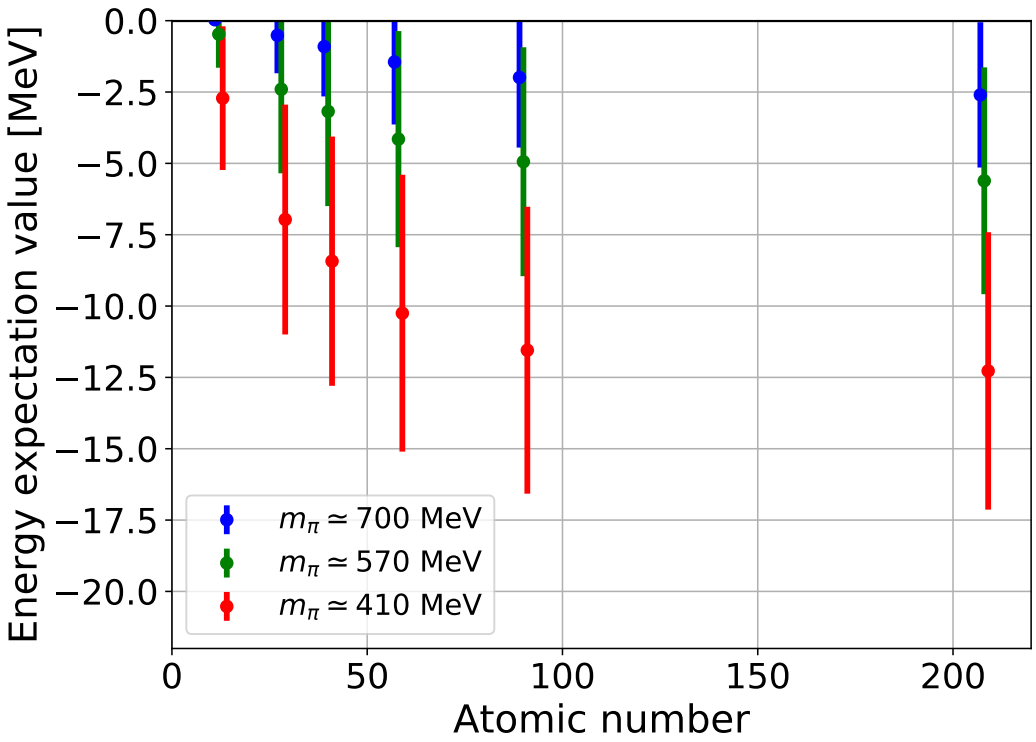

Figure 6.3: Binding energies of Λ_c in spherical nuclei such as ^{12}C, ^{28}Si, ^{40}Ca, ^{58}Ni, ^{90}Zr and ^{208}Pb for each ensemble. The binding energies are calculated from the folding potentials for Λ_c hypernuclei by using the Gaussian expansion method. The folding potentials are constructed from the spin-independent central potential of the $\Lambda_c N$ system (Fig. 5.7) for $m_\pi \simeq 700$, 570 and 410 MeV cases. In the calculation of the binding energies, we adjust the masses of Λ_c and nuclei to those of physical values.

Fig. 6.3 shows the binding energy of several Λ_c hypernuclei for each ensemble. As we expected, the binding energy $|E_b|$ increases as the atomic number increases. Furthermore, as the $\Lambda_c N$ potential approaches to the physical one (as the u, d quark masses decrease toward physical values), the binding energy increases. These results suggest that Λ_c hypernuclei may exist if their binding energy is larger than the Coulomb repulsion. In order to estimate the effect of Coulomb force, we calculate the expectation value for the Coulomb potential using the binding solutions of Λ_c hypernuclei $|\psi_b\rangle$ as

$$E_{\rm Coulomb} = \frac{\langle\psi_b|V_F^C|\psi_b\rangle}{\langle\psi_b|\psi_b\rangle}, \tag{6.15}$$

where V_F^C is the single-folding Coulomb potential defined by

$$V_F^C(\vec{r}) \;=\; \int d^3r' \rho_{\rm ch}(\vec{r'}) V_{\rm Coulomb}(\vec{r}-\vec{r'}), \tag{6.16}$$

where $V_{\rm Coulomb}(\vec{r})$ is an ordinary Coulomb potential and $\rho_{\rm ch}$ is charge density distribution by the Fourier-Bessel coefficient obtained from elastic electron scattering [69]. Fig. 6.4 shows the expectation values of the folding potential for Coulomb force calculated by using the binding solution of Λ_c hypernuclei for Ensemble 3 ($m_\pi \simeq 410$ MeV). For comparison, we also plot the binding energy for Λ_c hypernuclei without Coulomb potential and the sum of them in Fig. 6.4. We observe that the Coulomb repulsion is large for heavy nuclei and Λ_c-^{208}Pb state becomes unbound with the Coulomb force. In the nuclei for $A = 12 - 58$, on the other hand, the expectation values of Coulomb force are not much stronger than the binding energy of Λ_c hypernuclei. Since the binding energy increases as the attraction of the $\Lambda_c N$ potential becomes stronger toward the physical quark mass, this observation suggests a possibility that Λ_c hypernuclei may exist in light or medium-heavy nuclei.

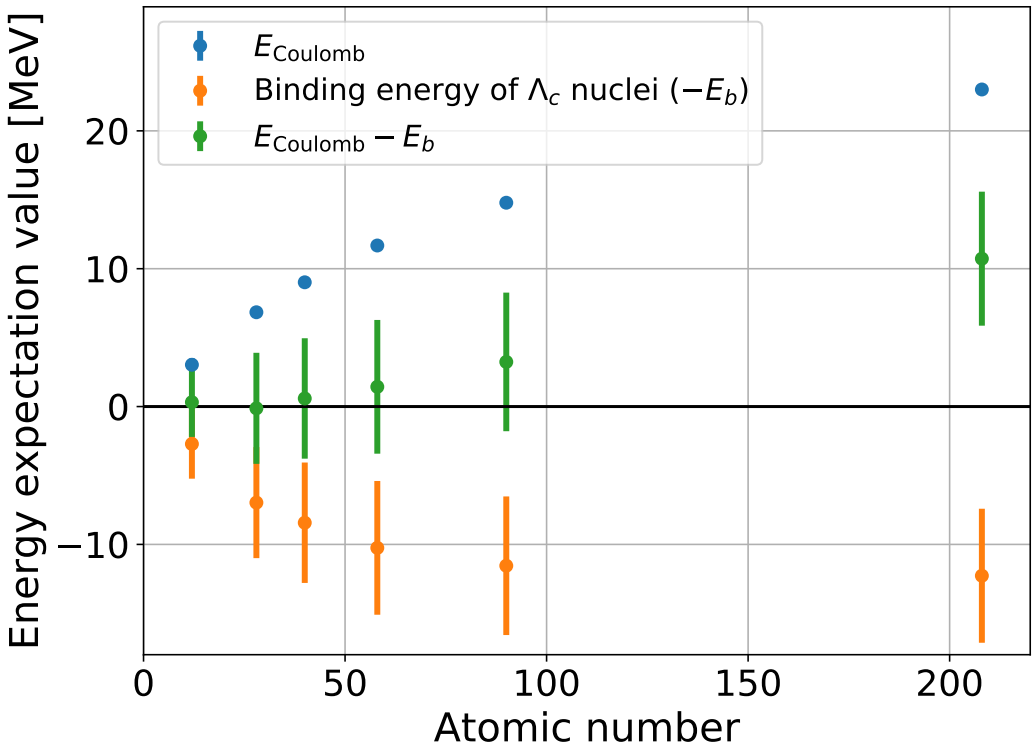

Figure 6.4: Expectation values of folding potential for Coulomb force in Λ_c hypernuclei (Blue). The expectation values are calculated from the binding solution of the Λ_c hypernuclei for Ensemble 3 ($m_\pi \simeq 410$ MeV). For comparison, the binding energy of Λ_c hypernuclei (Orange) and the sum of them (Green) are also plotted.

Chapter 7

Summary and conclusions

In this thesis, we introduce our works on the charmed baryon interactions as well as recent developments of the numerical algorithms for the partial wave decomposition on the lattice. For the numerical simulation, we have employed the $(2+1)$-flavor full QCD configurations generated by PACS-CS Collaboration with the renormalization-group improved Iwasaki gluon action and a non-perturbatively $\mathcal{O}(a)$ improved Wilson-clover quark action at $\beta = 6/g^2 = 1.90$ on a $L^3 \times T = 32^3 \times 64$ lattice (the corresponding lattice spacing is $a = 0.0907(13)$ fm and physical lattice size is $La = 2.902(42)$ fm) [16]. In order to investigate the u, d quark mass dependence, we have employed three ensembles of the gauge configurations with $m_\pi = 411(2),\ 570(1),\ 700(1)$ MeV. For the charm quark, we have employed the relativistic heavy quark (RHQ) action [36] with the RHQ parameters determined in Ref. [18] to avoid the leading $\mathcal{O}\left((m_Q a)^n\right)$ and the next-to-leading $\mathcal{O}\left((m_Q a)^n (a\Lambda_{\rm QCD})\right)$ discretization errors due to the charm quark mass m_Q. The partial wave decomposition for the NBS wave function has been carried out by using Misner's method [54]. We present the summary and conclusions for the application of Misner's method and the results of each charmed baryon interaction on a section by section. In the last section, we also present the future prospect of our calculation.

7.1 Partial wave decomposition for the NBS wave function by Misner's method

In the conventional lattice simulation, we employ the cubic transformation group for projection to the S-wave, which picks up an A_1^+ representation of O_h group. Since the

A_1^+ representation contains not only $L = 0$ component but also $L \geq 4$ components, the resultant projected NBS wave function may have comb-like structures, which correspond to the anisotropy of the wave function induced by $L \geq 4$ components. We have employed Misner's method to extract the $L = 0$ component of the NBS wave function for $\Lambda_c N$ system in $J^P = 0^+$ state in Sec. 5.2.1. We have also carried out the $L = 0$ and $L = 2$ projections by Misner's method to the NBS wave function for $\Lambda_c N$ system in $J^P = 1^+$ state in Sec. 5.2.2. In both systems, we found the small comb-like structures in the A_1^+ projected NBS wave function, which have not appeared in the results with Misner's method. This observation shows that the $L \geq 4$ components are small but exist so that they make comb-like structures. We have next calculated the Laplacian of the NBS wave function in both systems. In the conventional method, the Laplacian is defined by a finite second-order difference, while it is calculated analytically as the second-order derivative in Misner's method. The results have shown that the large comb-like structures in the conventional Laplacian of the NBS wave function are reduced in Misner's method. From their observations, we found that the $L \geq 4$ components in the NBS wave function may produce large comb-like structures in the Laplacian (also in potential) even the amplitude of the $L \geq 4$ components is small.

In Sec. 5.2.6, we have investigated the effect of the contamination of $L \geq 4$ components in potential to the physical observables in low energies, such as scattering length. To this end, we have compared the scattering lengths for the $\Lambda_c N$ system given in Ref. [23] (which may include $L \geq 4$ contamination) and those calculated from the S-wave potential with Misner's method. The results have shown that the scattering lengths are almost the same within the statistical errors, which suggest that the higher partial waves with $L \geq 4$ don't affect the physical observables.

7.2 $\Lambda_c N$ interaction

In Secs. 5.2.3 and 5.2.4, we have shown the $\Lambda_c N$ potentials and discussed their interactions. We have extracted the central potential in ${}^1S_0$ channel while central and tensor potentials in ${}^3S_1 - {}^3D_1$ channel. In the calculation for both potentials, we employ Misner's method to avoid $L \geq 4$ components in the NBS wave function. From the results, we found a repulsion at short distance and an attraction at the intermediate distance in the central potential for both channels. The strength of the attraction seems weaker compared with that in

the ΛN potential, and this weaker attraction is consistent with model calculations [3, 6]. In the tensor potential for the $\Lambda_c N$ system, we found that the (attractive) interaction range becomes shorter and the strength of the attraction is weaker compared with those for the ΛN system. Furthermore, as a consequence of the negligibly weak tensor force, the central potential in the ${}^3S_1 - {}^3D_1$ channel and the effective central potential in the ${}^3S_1$ channel are almost the same. In order to quantify the similarity of potentials between two channels, we have decomposed the central potentials into the spin-independent and spin-dependent ones. We found that the spin-dependent potential is negligibly weak except at a short distance. The observation of the small tensor and spin-dependent potential for $\Lambda_c N$ system can be understood by the heavy D-meson mass and the large separation of the $\Lambda_c N - \Sigma_c N$ threshold.

We then calculated phase shifts and scattering lengths using the potentials in the infinite volume in Sec. 5.2.6, in which we found that the $\Lambda_c N$ interaction is attractive at low energy in both ${}^1S_0$ and ${}^3S_1 - {}^3D_1$ channels. As in the case of potentials, strengths of the attraction are comparable between both channels.

7.3 Inelastic effects for the $\Lambda_c N$ interaction and $\Sigma_c N$ interaction in $I = 1/2$ channel

In order to investigate the inelastic effects for the $\Lambda_c N$ system, we have calculated the $\Lambda_c N$-$\Sigma_c N$ coupled channel potential with Misner's method in Sec. 5.3. In the case of ${}^1S_0$ channel, we have observed that the tail of the potential deviates from zero and the time dependence of the potential is still large, which imply that the time separation between sink operator and source operator $(t - t_0)$ is not large enough. Since statistical errors increase for large $t - t_0$, however, we need more large statistics to investigate the ${}^1S_0$ channel. In the case of ${}^3S_1 - {}^3D_1$ channel, on the other hand, we have obtained reliable results that the potentials are stable against the change of $t - t_0$ within the statistical errors. We have calculated the coupled channel potentials for both central and tensor forces. Results of the potential matrix have shown that the central potential for $\Lambda_c N$ channel is almost the same with the single channel potential. The central potential for $\Sigma_c N$ channel has shown strong attraction. From the comparison with the ΣN potential, we found that the attraction in $\Sigma_c N$ is stronger than that in ΣN. In the off-diagonal element of the potentials, we have observed that the central potential is weak while the

tensor potential is strong.

The phase shifts extracted by solving the Schrödinger equation in the infinite volume with the obtained potentials have shown that the S-wave $\Sigma_c N$ channel has rather strong attraction at low energies but it does not have the two-body bound state at $m_\pi \geq 410$ MeV. In the D-wave $\Lambda_c N$ phase shift, we have observed a cusp-like structure around the $\Sigma_c N$ threshold, while there no such a structure in the S-wave $\Lambda_c N$ phase shift. The cusp-like structure in the D-wave $\Lambda_c N$ phase shift is induced by strong attraction in S-wave $\Sigma_c N$ channel through the strong tensor transition potential. However, the strong attraction in S-wave $\Sigma_c N$ does not affect the S-wave $\Lambda_c N$ because both the tensor potential for $\Lambda_c N$ channel and central transition potential between $\Lambda_c N$-$\Sigma_c N$ are weak.

Furthermore, in Sec. 5.3.4, we investigate the non-locality of the single channel $\Lambda_c N$ potential by comparing the phase shifts in the single channel analysis and those in the coupled channel analysis. From the results, we found that the two S-wave $\Lambda_c N$ phase shifts are almost identical within the statistical errors, which suggest that the non-locality of the $\Lambda_c N$ central potential in the single channel analysis is sufficiently small. In the D-wave $\Lambda_c N$ phase shift, however, the two results are different even below the $\Sigma_c N$ threshold, which imply that the $\Lambda_c N$ tensor potential in the single channel analysis has large non-locality near and above the $\Sigma_c N$ threshold.

7.4 $\Lambda_c\Lambda_c$-$\Xi_{cc}N$ coupled channel system in $J(I) = 0(0)$ channel

In Sec. 5.4, we have investigated the interaction between doubly charmed baryon Ξ_{cc} and a nucleon in the $J(I) = 0(0)$ channel, which relates a charm version of the H-dibaryon. To do this, we calculate the $\Lambda_c\Lambda_c$-$\Xi_{cc}N$ coupled channel potentials with Misner's method. The results of the potential have shown that the attraction in the $\Xi_{cc}N(I = 0)$ potential is strong while the $\Lambda_c\Lambda_c$ and the off-diagonal potentials are weak. The phase shift analysis given in Sec. 5.4.2 has shown that the $\Xi_{cc}N(I = 0)$ attraction is sufficiently strong to form a resonance state in the $\Lambda_c\Lambda_c$ scattering. We also found that the resonance state in the $\Lambda_c\Lambda_c$ scattering is very sharp, which indicates the weak strength of the transition between the $\Lambda_c\Lambda_c$ and $\Xi_{cc}N(I = 0)$.

In the physical mass, the mass threshold of the $\Xi_{cc}N$ is below the $\Lambda_c\Lambda_c$ threshold. Therefore, the charm version of the H-dibaryon appears as a bound state of the $\Xi_{cc}N$ if

the $\Xi_{cc}N$ attraction is sufficiently strong. Our numerical results suggest the possibility of such a state in the physical mass.

7.5 Λ_c-hypernuclei

In the analysis for the $\Lambda_c N$ 2-body interaction, we found that the $\Lambda_c N$ interaction is weakly attractive and spin-independent, which indicates Λ_c baryon can be bound in nuclei with sufficiently large atomic number. Since Λ_c baryon has a charge +1, however, large Coulomb repulsion occurs when the number of the proton is large. In order to investigate possible Λ_c hypernuclei, we have constructed an S-wave effective potential between Λ_c and nuclei. Since the dominant contribution of the $\Lambda_c N$ interaction comes from the spin-independent central potential, the single-folding potential for Λ_c hypernuclei can be constructed from the $\Lambda_c N$ potential obtained in our calculation. For the nuclear density distribution function, we employed the two-parameter Fermi form for symmetric nuclei such as ^{12}C, ^{28}Ni, ^{40}Ca, ^{58}Ni, ^{90}Zr, and ^{208}Pb. By the Gaussian expansion method, we got binding solutions for Λ_c hypernuclei. We found that the binding energy of Λ_c hypernuclei becomes larger as the nucleon number increases and/or the u, d quark mass decreases. This suggests the possibility of Λ_c hypernuclei at the physical u, d quark mass if their binding energy is larger than the Coulomb repulsion. In order to estimate the strength of Coulomb repulsion, we have calculated the expectation value for the Coulomb force using the binding solution of Λ_c hypernuclei. The results show that the expectation values for the Coulomb force are much stronger than the binding energy for heavy nuclei, while they are comparable in light or medium-heavy nuclei. These observations suggest possible Λ_c hypernuclei with light or medium-heavy nuclei in nature.

7.6 Future prospect

Very recently, we have started to carry out $(2+1)$-flavor full QCD simulations near the physical quark masses [70] ($m_\pi \simeq 146$ MeV and $m_K \simeq 525$ MeV) for charmed hadron interactions. This gauge configuration has already been employed for several hyperon interactions [71, 72, 73, 74, 75]. We expect to make definite conclusions on the charmed baryon interactions and charmed hypernuclei in this near future work.

Acknowledgments

First of all, I would like to express my gratitude to Prof. Sinya Aoki for his fruitful guidance and helpful support. I am very grateful to Dr. Kenji Sasaki and Dr. Yoichi Ikeda for stimulating discussions and providing me with instructive advice. I am also grateful to the members of the HAL QCD Collaboration, Prof. Tetsuo Hatsuda, Dr. Noriyoshi Ishii, Dr. Takumi Doi, Prof. Takashi Inoue, Dr. Hidekatsu Nemura, Dr. Takumi Iritani, Dr. Shinya Gongyo, Dr. Daisuke Kawai, and Mr. Yutaro Akahoshi for discussing and collaborating on the research. I would like to thank Dr. Shigehiro Yasui and Dr. Yasuhiro Yamaguchi for fruitful discussions and comments on the charmed baryon interaction. I wish to thank past and present members in YITP, Dr. Tomoki Nosaka, Dr. Tokiro Numasawa, Dr. Kento Watanabe, Mr. Kazuma Shimizu, who will also be my colleague from next April, Mr. Masamichi Miyaji, Mr. Yuki Kamiya, and Mr. Yutaro Akahoshi for warm friendship, interesting discussions and a lot of help. I owe very important debts to my family, Shinya Miyamoto, Sayomi Miyamoto, Yuya Miyamoto, and Yuko Miyamoto for their moral support and warm encouragement.

We thank the PACS-CS Collaboration for providing us their (2+1) flavor gauge configurations [16]. This work is in part based on Bridge++ code [76]. Numerical computations of this work have been carried out by the KEK supercomputer system (BG/Q), [Project numbers: 14/15-21, 15/16-12] and the Cray XC40 in Yukawa Institute for Theoretical Physics (YITP) in Kyoto University.

Appendix A

Analysis for statistical uncertainty

In the lattice QCD calculation, we obtain observables (such as a two-point correlation function and a four-point correlation function) as statistical data due to the Monte-Carlo simulation. One can estimate the statistical uncertainty for the observables using a statistical method. The uncertainty of more "complex" observables (such as an effective mass and a potential) can be estimated by an error propagation. Since each statistical data for the observable is correlated in the Monte-Carlo simulation, however, one may overestimate the uncertainty. In order to estimate correct uncertainty, we utilize the Jackknife method which is useful to estimate the statistical errors for correlated data. The Jackknife method has an advantage that it can be applied to "complex" observables straightforwardly. In this chapter, we briefly present the methodology of the Jackknife method.

A.1 Basic statistical error estimation and error propagation

First of all, we show the formalism for basic statistics. Assume that we have N number of observable data $\{\mathcal{O}_i\}$ $(i = 1, \cdots, N)$. The mean value $\langle\mathcal{O}\rangle$ and the statistical error $\delta\langle\mathcal{O}\rangle$ are given by

$$\langle\mathcal{O}\rangle = \frac{1}{N}\sum_{i=1}^{N}\mathcal{O}_i, \tag{A.1}$$

$$\delta\langle\mathcal{O}\rangle = \sqrt{\frac{\langle\mathcal{O}^2\rangle - \langle\mathcal{O}\rangle^2}{N-1}}, \tag{A.2}$$

where $\langle \mathcal{O}^2 \rangle$ denotes the mean value for the square of the observable data.

We next consider N number of "complex" observable $\{f(\mathcal{O}_i^{(1)}, \cdots, \mathcal{O}_i^{(M)})\}$ $(i = 1, \cdots, N)$ which is a function constructed from the M set of observable data $\{\mathcal{O}_i^{(a)}\}$ $(a = 1, \cdots, M)$. The statistical errors for the "complex" observable are obtained from an error propagation.

$$\delta\langle f(\mathcal{O})\rangle = \sum_a \left| \langle \frac{\partial f}{\partial \mathcal{O}^{(a)}} \rangle \ \delta\langle \mathcal{O}^{(a)} \rangle \right|. \tag{A.3}$$

It is noted that the statistical errors for the "complex" observable $f(\mathcal{O})$ estimated by the error propagation are maybe overestimated due to correlated data. Since some statistical errors are canceled each other when the observables are correlated, the "true" statistical errors could be small.

A.2 Jackknife method

In order to estimate the correlated data correctly, we first define the average of the observable $\{\mathcal{O}_i\}$ without i-th data as

$$\langle \mathcal{O} \rangle_i = \frac{1}{N-1} \sum_{k \neq i}^{N} \mathcal{O}_k, \tag{A.4}$$

which is a so-called Jackknife sample with the binsize (i.e., number of data to remove) of one. Using the Jackknife samples, the mean value and the statistical error for the "complex" observable $f(\mathcal{O})$ are given by

$$\langle f(\mathcal{O})\rangle = \frac{1}{N} \sum_{i=1}^{N} f(\langle \mathcal{O} \rangle_i^{(1)}, \cdots, \langle \mathcal{O} \rangle_i^{(M)}), \tag{A.5}$$

$$\delta\langle f(\mathcal{O})\rangle = \sqrt{(N-1)(\langle f^2(\mathcal{O})\rangle - \langle f(\mathcal{O})\rangle^2)}. \tag{A.6}$$

One of the advantages of the Jackknife method is that it can be easily applied to an arbitrary function $f(\mathcal{O})$. Another advantage is that one can estimate the auto-correlation for the statistical data by increasing the number of data to remove in Eq. (A.4).

In order to estimate the auto-correlation, we generalize the above discussion to the case of binsize of n. We assume that the binsize and the number of statistics satisfy $N = n \times N_b$, where N_b is a number of bins. Therefore, the size of the resultant Jackknife

sample is N_b. The b-th Jackknife sample is defined by

$$\langle \mathcal{O} \rangle_b = \frac{1}{N-n} \left(\sum_{k=1}^{N} \mathcal{O}_k - \sum_{k=1+(b-1)n}^{nb} \mathcal{O}_k \right), \qquad (b = 1, \cdots, N_b) \tag{A.7}$$

and the mean value and the statistical error for the "complex" observable $f(\mathcal{O})$ are given as

$$\langle f(\mathcal{O}) \rangle = \frac{1}{N_b} \sum_{b=1}^{N_b} f(\langle \mathcal{O} \rangle_b^{(1)}, \cdots, \langle \mathcal{O} \rangle_b^{(M)}), \tag{A.8}$$

$$\delta \langle f(\mathcal{O}) \rangle = \sqrt{(N_b - 1)(\langle f^2(\mathcal{O}) \rangle - \langle f(\mathcal{O}) \rangle^2)}. \tag{A.9}$$

Appendix B

Time-dependent HAL QCD method for two-body system with different mass

In this appendix, we derive the relation

$$\frac{k_n^2}{2\mu} = \Delta W_n + \frac{1+3\delta^2}{8\mu}\left(\Delta W_n\right)^2 + \mathcal{O}\left(\left(\Delta W_n\right)^3\right), \tag{B.1}$$

where

$$\Delta W_n = W_n - \left(m_{B^{(1)}} + m_{B^{(2)}}\right), \tag{B.2}$$

$$W_n = \sqrt{k_n^2 + m_{B^{(1)}}^2} + \sqrt{k_n^2 + m_{B^{(2)}}^2}, \tag{B.3}$$

$$\mu = \frac{m_{B^{(1)}} m_{B^{(2)}}}{m_{B^{(1)}} + m_{B^{(2)}}}, \tag{B.4}$$

$$\delta = \frac{m_{B^{(1)}} - m_{B^{(2)}}}{m_{B^{(1)}} + m_{B^{(2)}}}, \tag{B.5}$$

and $m_{B^{(1)}} \neq m_{B^{(2)}}$. For simplicity, we denote $m_{B^{(i)}}$ $(i = 1, 2)$ as m_i in following discussions.

We first calculate $(\Delta W_n)^2$:

$$\begin{aligned}
(\Delta W_n)^2 &= \left(\sqrt{k_n^2+m_1^2}+\sqrt{k_n^2+m_2^2}-(m_1+m_2)\right)^2 \\
&= 2k_n^2+m_1^2+m_2^2+(m_1+m_2)^2+2\sqrt{k_n^2+m_1^2}\sqrt{k_n^2+m_2^2} \\
&\quad -2(m_1+m_2)\sqrt{k_n^2+m_1^2}-2(m_1+m_2)\sqrt{k_n^2+m_2^2} \\
&= 2k_n^2+m_1^2+m_2^2-(m_1+m_2)^2-2(m_1+m_2)\Delta W_n \\
&\quad +2\sqrt{k_n^2+m_1^2}\sqrt{k_n^2+m_2^2} \\
&= 2\left(k_n^2-m_1m_2-(m_1+m_2)\Delta W_n+\sqrt{k_n^2+m_1^2}\sqrt{k_n^2+m_2^2}\right),
\end{aligned} \tag{B.6}$$

thus we obtain

$$\sqrt{k_n^2+m_1^2}\sqrt{k_n^2+m_2^2} = \frac{(\Delta W_n)^2}{2}-k_n^2+m_1m_2+(m_1+m_2)\Delta W_n. \tag{B.7}$$

Next, we take the square of both sides in Eq. (B.7).

$$\begin{aligned}
(\mathrm{lhs})^2 &= \left[\sqrt{k_n^2+m_1^2}\sqrt{k_n^2+m_2^2}\right]^2 \\
&= k_n^4+(m_1^2+m_2^2)k_n^2+m_1^2m_2^2,
\end{aligned} \tag{B.8}$$

$$\begin{aligned}
(\mathrm{rhs})^2 &= \left[\frac{(\Delta W_n)^2}{2}-k_n^2+m_1m_2+(m_1+m_2)\Delta W_n\right]^2 \\
&= k_n^4-2\left(\frac{(\Delta W_n)^2}{2}+m_1m_2+(m_1+m_2)\Delta W_n\right)k_n^2+m_1^2m_2^2 \\
&\quad +2m_1m_2(m_1+m_2)\Delta W_n+m_1m_2(\Delta W_n)^2 \\
&\quad +(m_1+m_2)^2(\Delta W_n)^2+(m_1+m_2)(\Delta W_n)^3+\frac{(\Delta W_n)^4}{4},
\end{aligned} \tag{B.9}$$

then we move k_n-dependent terms to the left-hand side, while k_n-independent terms are moved to the right-hand side.

$$\begin{aligned}
(\text{lhs}) &= (m_1^2+m_2^2)k_n^2 + 2\left(\frac{(\Delta W_n)^2}{2} + m_1m_2 + (m_1+m_2)\Delta W_n\right)k_n^2 \\
&= \left((\Delta W_n)^2 + (m_1+m_2)^2 + 2(m_1+m_2)\Delta W_n\right)k_n^2 \\
&= \left(\Delta W_n + (m_1+m_2)\right)^2 k_n^2 \;= W_n^2\; k_n^2, \qquad (B.10)
\end{aligned}$$

$$\begin{aligned}
(\text{rhs}) &= 2m_1m_2(m_1+m_2)\Delta W_n + m_1m_2(\Delta W_n)^2 \\
&\quad + (m_1+m_2)^2(\Delta W_n)^2 + (m_1+m_2)(\Delta W_n)^3 + \frac{(\Delta W_n)^4}{4}, \qquad (B.11)
\end{aligned}$$

thus we obtain

$$\begin{aligned}
4W_n^2k_n^2 &= 8m_1m_2(m_1+m_2)\Delta W_n + 4m_1m_2(\Delta W_n)^2 \\
&\quad + 4(m_1+m_2)^2(\Delta W_n)^2 + 4(m_1+m_2)(\Delta W_n)^3 + (\Delta W_n)^4. \qquad (B.12)
\end{aligned}$$

Eq. (B.12) can be summarized as follows.

$$\begin{aligned}
4W_n^2k_n^2 &= 8m_1m_2(m_1+m_2)\Delta W_n + 4m_1m_2(\Delta W_n)^2 \\
&\quad + 4(m_1+m_2)^2(\Delta W_n)^2 + 4(m_1+m_2)(\Delta W_n)^3 + (\Delta W_n)^4 \\
&= -4m_1m_2(m_1+m_2)^2 \\
&\quad + \left[(m_1+m_2)^2 + 2(m_1+m_2)\Delta W_n + (\Delta W_n)^2\right]4m_1m_2 \\
&\quad + 3(m_1+m_2)^2(\Delta W_n)^2 + 2(m_1+m_2)(\Delta W_n)^3 \\
&\quad + \left[(m_1+m_2)^2 + 2(m_1+m_2)\Delta W_n + (\Delta W_n)^2\right](\Delta W_n)^2 \\
&= -4m_1m_2(m_1+m_2)^2 + 4W_n^2m_1m_2 + W_n^2(\Delta W_n)^2 \\
&\quad - 2(m_1+m_2)^3\Delta W_n - (m_1+m_2)^2(\Delta W_n)^2
\end{aligned}$$

$$
\begin{aligned}
&+ \left[(m_1+m_2)^2 + 2(m_1+m_2)\Delta W_n + (\Delta W_n)^2\right] 2(m_1+m_2)\Delta W_n \\
&= -4m_1m_2(m_1+m_2)^2 \\
&\quad + 4W_n^2 m_1 m_2 + 2W_n^2(m_1+m_2)\Delta W_n + W_n^2(\Delta W_n)^2 \\
&\quad + (m_1+m_2)^4 \\
&\quad - \left[(m_1+m_2)^2 + 2(m_1+m_2)\Delta W_n + (\Delta W_n)^2\right](m_1+m_2)^2 \\
&= -4m_1m_2(m_1+m_2)^2 + (m_1+m_2)^4 \\
&\quad + 4W_n^2 m_1 m_2 - W_n^2(m_1+m_2)^2 + 2W_n^2(m_1+m_2)\Delta W_n + W_n^2(\Delta W_n)^2 \\
&= (m_1^2+m_2^2)^2 - W_n^2(m_1-m_2)^2 + 2W_n^2(m_1+m_2)\Delta W_n + W_n^2(\Delta W_n)^2.
\end{aligned}
\tag{B.13}
$$

Dividing Eq. (B.13) by W_n^2, we have

$$
4k_n^2 = \frac{(m_1^2+m_2^2)^2}{W_n^2} - (m_1-m_2)^2 + 2(m_1+m_2)\Delta W_n + (\Delta W_n)^2. \tag{B.14}
$$

Here, we assume that ΔW_n is sufficiently small and we consider the following expansion for the first term of right-hand side in Eq. (B.14).

$$
\begin{aligned}
\frac{(m_1^2+m_2^2)^2}{W_n^2} &= \frac{(m_1^2+m_2^2)^2}{(\Delta W_n + (m_1+m_2))^2} \\
&= \frac{(m_1^2+m_2^2)^2}{(m_1+m_2)^2}\left[1+\frac{\Delta W_n}{m_1+m_2}\right]^{-2} \\
&= (m_1-m_2)^2 \sum_{n=0}^{\infty}(n+1)\left[-\frac{\Delta W_n}{m_1+m_2}\right]^n \\
&= (m_1-m_2)^2 - 2\frac{(m_1-m_2)^2}{m_1+m_2}\Delta W_n + 3\left(\frac{m_1-m_2}{m_1+m_2}\right)^2(\Delta W_n)^2 \\
&\quad + (m_1-m_2)^2 \sum_{n=3}^{\infty}(n+1)\left[-\frac{\Delta W_n}{m_1+m_2}\right]^n.
\end{aligned}
\tag{B.15}
$$

Using Eq. (B.15), we can evaluate Eq. (B.14) as

$$\begin{aligned} 4k_n^2 &= \left(2(m_1+m_2) - 2\frac{(m_1-m_2)^2}{m_1+m_2}\right)\Delta W_n + \left(1+3\left(\frac{m_1-m_2}{m_1+m_2}\right)^2\right)(\Delta W_n)^2 \\ &\quad + (m_1-m_2)^2\sum_{n=3}^{\infty}(n+1)\left[-\frac{\Delta W_n}{m_1+m_2}\right]^n \\ &= 8\mu\Delta W_n + \left(1+3\delta^2\right)(\Delta W_n)^2 + (m_1-m_2)^2\sum_{n=3}^{\infty}(n+1)\left[-\frac{\Delta W_n}{m_1+m_2}\right]^n. \end{aligned} \tag{B.16}$$

Finally, we obtain Eq. (B.1) as follows.

$$\begin{aligned} \frac{k_n^2}{2\mu} &= \Delta W_n + \frac{1+3\delta^2}{8\mu}(\Delta W_n)^2 + \frac{(m_1-m_2)^2}{8\mu}\sum_{n=3}^{\infty}(n+1)\left[-\frac{\Delta W_n}{m_1+m_2}\right]^n \\ &= \Delta W_n + \frac{1+3\delta^2}{8\mu}(\Delta W_n)^2 + \mathcal{O}\left((\Delta W_n)^3\right) \end{aligned} \tag{B.17}$$

Appendix C

Extraction of the Z-factor

As we expressed in Chapter 3, the NBS wave function is defined as a correlation function for local interpolating operators with their renormalization factor $\sqrt{Z}$, namely Z-factor. Here the Z-factor for the baryon operator $B(x)$[1] is defined by

$$\sqrt{Z_B} \equiv \langle 0|B(0)|B\rangle, \tag{C.1}$$

where $|B\rangle$ stands for the grand state of baryon B. In the HAL QCD method for a single channel system, we have not to estimate the Z-factors because they are common to the numerator and denominator in the equation for the potential (e.g. see Eq. (3.13)) so that they are reduced. In the coupled channel system, however, the Z-factors give a correction in the off-diagonal potentials as Eq. (3.67). In this appendix, we present how to extract the Z-factors from the correlation functions and show the numerical results which have been employed to construct the coupled channel potentials in this thesis.

C.1 Z-factor extraction from 2pt-correlation functions

The Z-factor for the baryon B can be extracted from the 2pt-correlation function on the lattice. In our numerical setup, the source operator is defined as "Wall-type smearing operator" which is one of the smearing operators defined in just after Eq. (3.16), while we don't take any smearing in the sink operator (we here call it "Point-type operator").

[1] We omit the spin index in the baryon operator for simplicity.

In this case, the 2pt-correlation function is defined as

$$\begin{aligned} C_B^{PW}(t-t_0) &= \sum_{\vec{x}} \langle 0|B^P(\vec{x},t)\overline{B^W(t_0)}|0\rangle \\ &= \langle 0|B^P(0)|B\rangle\langle B|\overline{B^W(0)}|0\rangle \frac{e^{-m_B(t-t_0)}}{2m_B} + \cdots \\ &= \sqrt{Z_B^P}\sqrt{Z_B^W}\frac{e^{-m_B(t-t_0)}}{2m_B} + \cdots , \end{aligned} \tag{C.2}$$

where $B^P(\vec{x},t)$ ($B^W(t_0)$) corresponds to the point-type (wall-type smearing) operator for the baryon B, m_B is the mass of baryon B, and the ellipses represent contributions from excited states. $\sqrt{Z_B^P}$ and $\sqrt{Z_B^W}$ stand for the Z-factors for the point-type operator and the wall-type smearing operator, respectively. In order to extract each Z-factor, we also calculate the 2pt-correlation function with the wall-type smearing operator in both sink and source defined as

$$\begin{aligned} C_B^{WW}(t-t_0) &= \sum_{\vec{x}} \langle 0|B^W(\vec{x},t)\overline{B^W(t_0)}|0\rangle \\ &= \sqrt{Z_B^W}\sqrt{Z_B^W}\frac{e^{-m_B(t-t_0)}}{2m_B} + \cdots . \end{aligned} \tag{C.3}$$

Using these 2pt-correlation functions and given m_B[2], the Z-factors are calculated from

$$\sqrt{Z_B^P} = \frac{C_B^{PW}(t-t_0)}{\sqrt{C_B^{WW}(t-t_0)}}\sqrt{\frac{2m_B}{e^{-m_B(t-t_0)}}} \tag{C.4}$$

$$\sqrt{Z_B^W} = \sqrt{C_B^{WW}(t-t_0)}\sqrt{\frac{2m_B}{e^{-m_B(t-t_0)}}}, \tag{C.5}$$

at $t-t_0 \to \infty$. In the practical calculation, these Z-factors are estimated by plotting the right-hand side in Eqs. (C.4) and (C.5) against the $t-t_0$ in the same manner as the effective mass plot. We note that it is useful to see the following relation for the consistency check of extracted Z-factors:

$$\frac{C_B^{PW}(t-t_0)}{C_B^{WW}(t-t_0)} = \frac{\sqrt{Z_B^P}}{\sqrt{Z_B^W}}, \tag{C.6}$$

[2]The baryon mass m_B is also extracted from the 2pt-correlation function on the lattice as we shown in Sec. 2.4.1.

which are realized at $t - t_0 \to \infty$.

C.2 Numerical results of Z-factor extraction

In this section, we show three figures for each baryon. The first figure of them is a plot of the right-hand side in Eqs. (C.4) against the $t - t_0$ and the result of fitting for $\sqrt{Z_B^P}$ with its fit-range. The second one is a plot of the right-hand side in Eqs. (C.5) against the $t - t_0$ and the fitting results for $\sqrt{Z_B^W}$ with its fit-range. The third one is a plot of the left-hand side in Eqs. (C.6) against the $t - t_0$ with the ratio of extracted Z-factors, $\sqrt{Z_B^P}/\sqrt{Z_B^W}$. The summary of the Z-factors is given in Table C.1. Note that we employ values of the baryon masses m_B shown in Sec. 5.1 for extracting the Z-factors.

Table C.1: The summary of the Z-factors for each hadron and the fit-range.

		$\sqrt{Z_B^P}$	$\sqrt{Z_B^W}$	$t_{\rm fit}$
Ensemble 1 ($m_\pi \simeq 700$ MeV case)	N	0.06310 (83)	0.0000852 (15)	12-17
	Λ	0.06697 (78)	0.0000856 (14)	12-17
	Λ_c	0.11395 (95)	0.0000890 (13)	12-17
	Σ	0.06640 (83)	0.0000855 (14)	12-17
	Σ_c	0.10018 (112)	0.0000871 (14)	12-17
	Ξ	0.07071 (77)	0.0000857 (13)	12-17
	Ξ_{cc}	0.20195 (341)	0.0000760 (14)	15-20
Ensemble 2 ($m_\pi \simeq 570$ MeV case)	N	0.04817 (79)	0.0000866 (14)	12-17
	Λ	0.05346 (94)	0.0000882 (17)	12-17
	Λ_c	0.09237 (116)	0.0000954 (4)	12-17
	Σ	0.05317 (127)	0.0000877 (20)	12-17
	Σ_c	0.08320 (103)	0.0000934 (11)	12-17
	Ξ	0.05888 (89)	0.0000886 (14)	12-17
	Ξ_{cc}	0.17206 (266)	0.0000821 (9)	15-20
Ensemble 3 ($m_\pi \simeq 410$ MeV case)	N	0.03769 (139)	0.0000889 (21)	12-17
	Λ	0.04257 (113)	0.0000906 (15)	12-17
	Λ_c	0.07713 (145)	0.0001049 (16)	12-17
	Σ	0.04298 (165)	0.0000910 (28)	12-17
	Σ_c	0.06683 (231)	0.0001032 (25)	12-17
	Ξ	0.04953 (108)	0.0000924 (14)	12-17
	Ξ_{cc}	0.15713 (168)	0.0000914 (14)	15-20

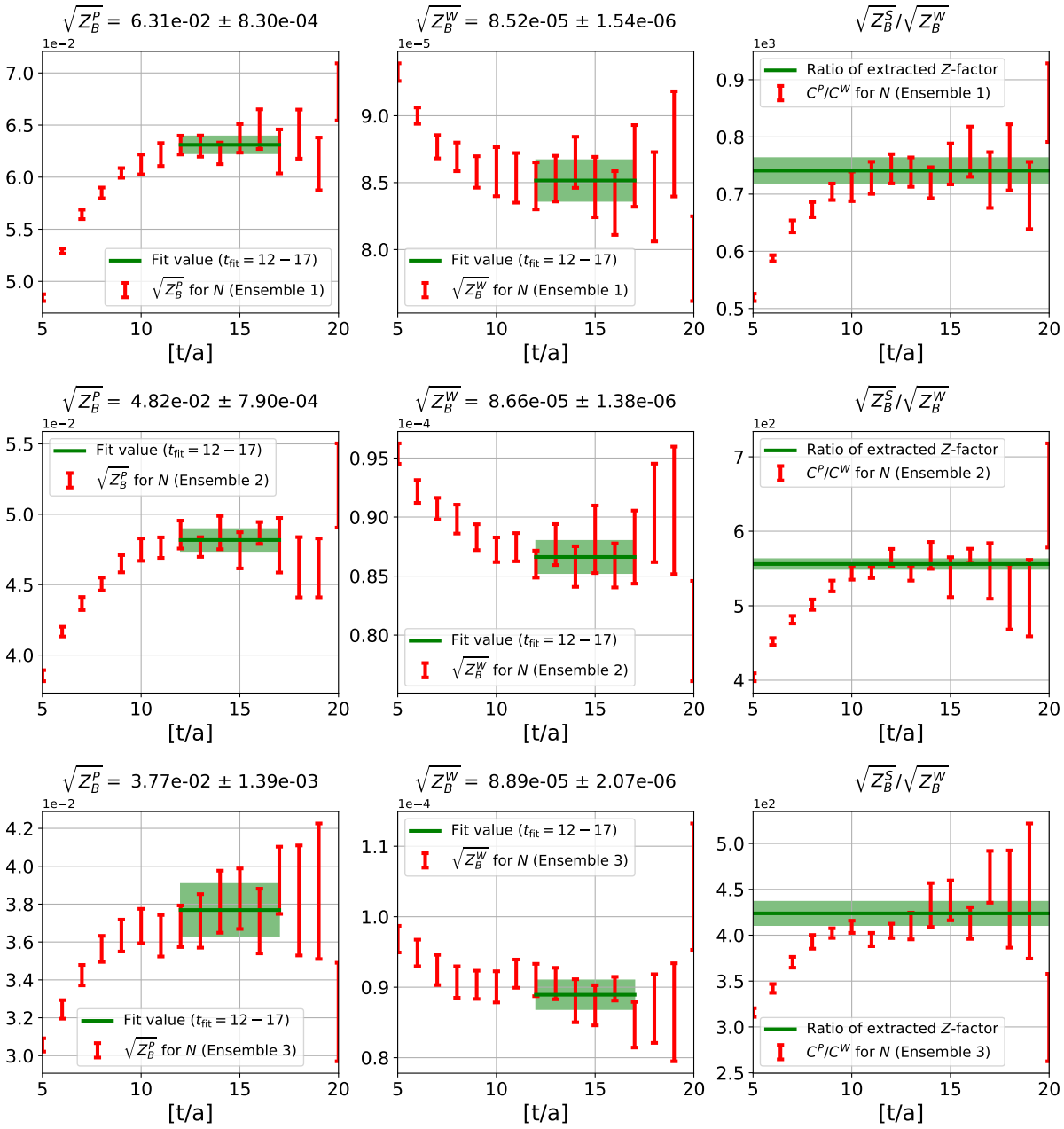

Figure C.1: The fitting results of the Z-factors for a nucleon. Upper three figures correspond to the results for the ensemble 1 ($m_\pi \simeq 700$ MeV case). Middle three figures correspond to the results for the ensemble 2 ($m_\pi \simeq 570$ MeV case). Lower three figures correspond to the results for the ensemble 3 ($m_\pi \simeq 410$ MeV case).

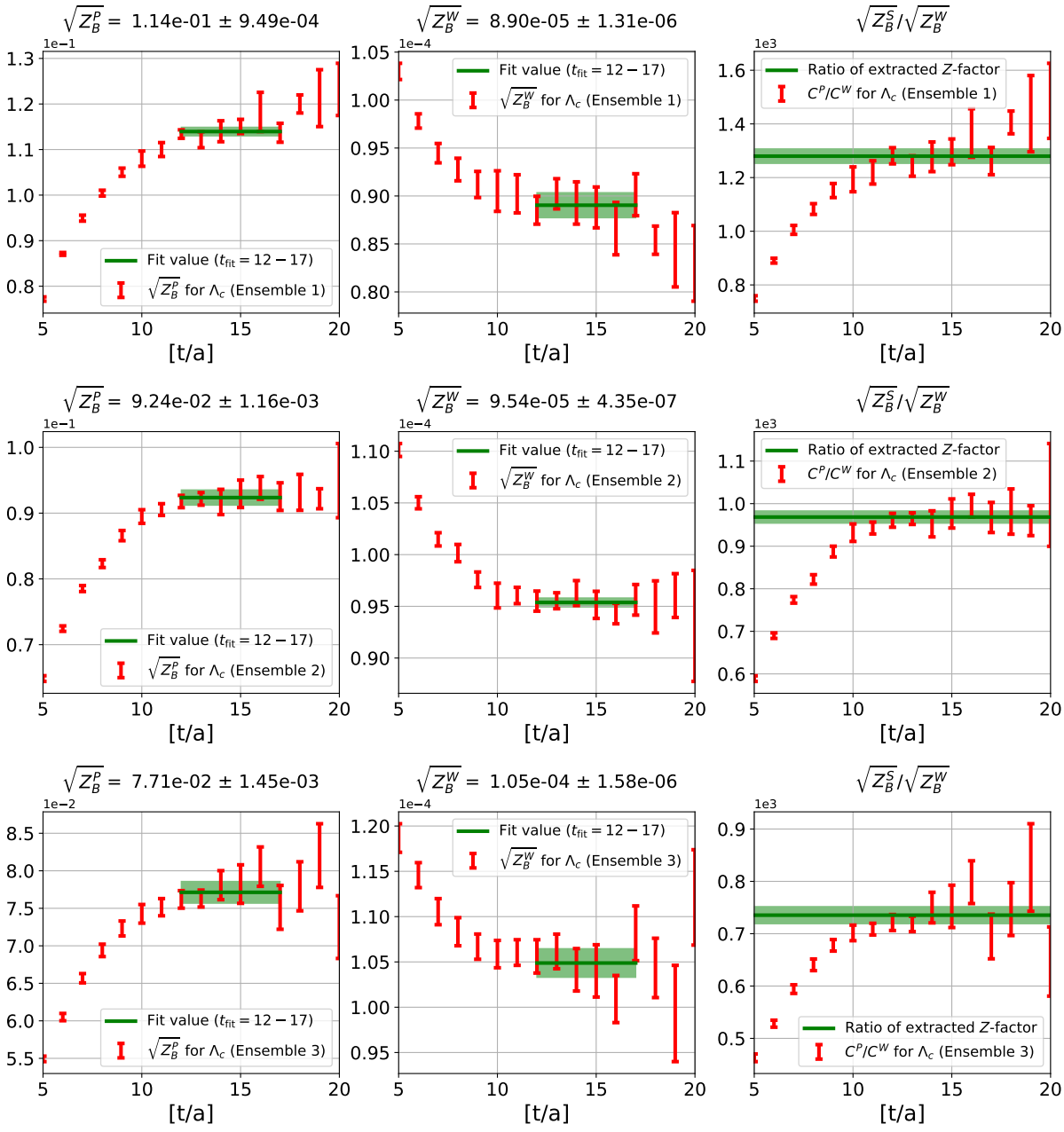

Figure C.2: The fitting results of the Z-factors for Λ_c. Upper three figures correspond to the results for the ensemble 1 ($m_\pi \simeq 700$ MeV case). Middle three figures correspond to the results for the ensemble 2 ($m_\pi \simeq 570$ MeV case). Lower three figures correspond to the results for the ensemble 3 ($m_\pi \simeq 410$ MeV case).

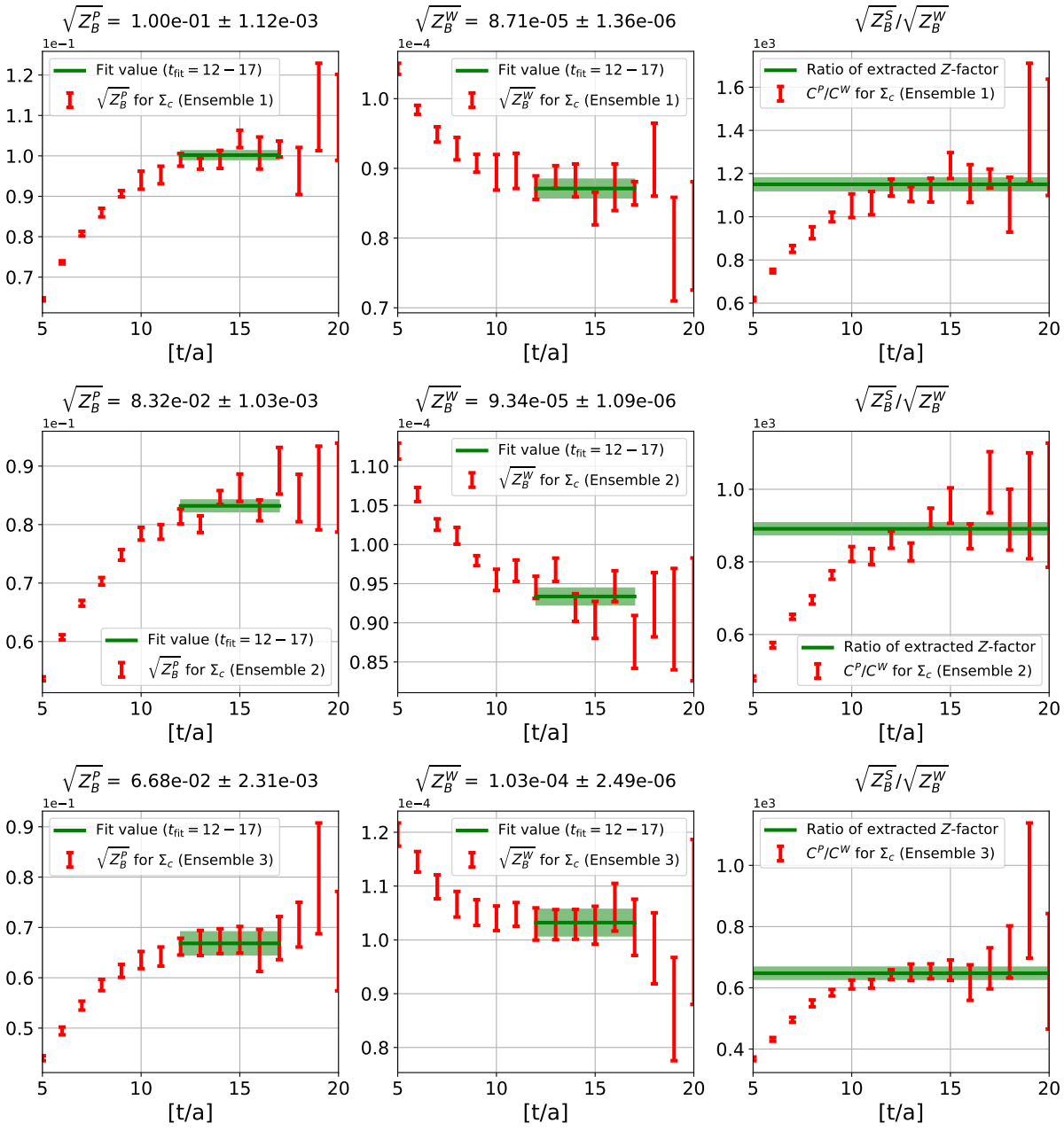

Figure C.3: The fitting results of the Z-factors for Σ_c. Upper three figures correspond to the results for the ensemble 1 ($m_\pi \simeq 700$ MeV case). Middle three figures correspond to the results for the ensemble 2 ($m_\pi \simeq 570$ MeV case). Lower three figures correspond to the results for the ensemble 3 ($m_\pi \simeq 410$ MeV case).

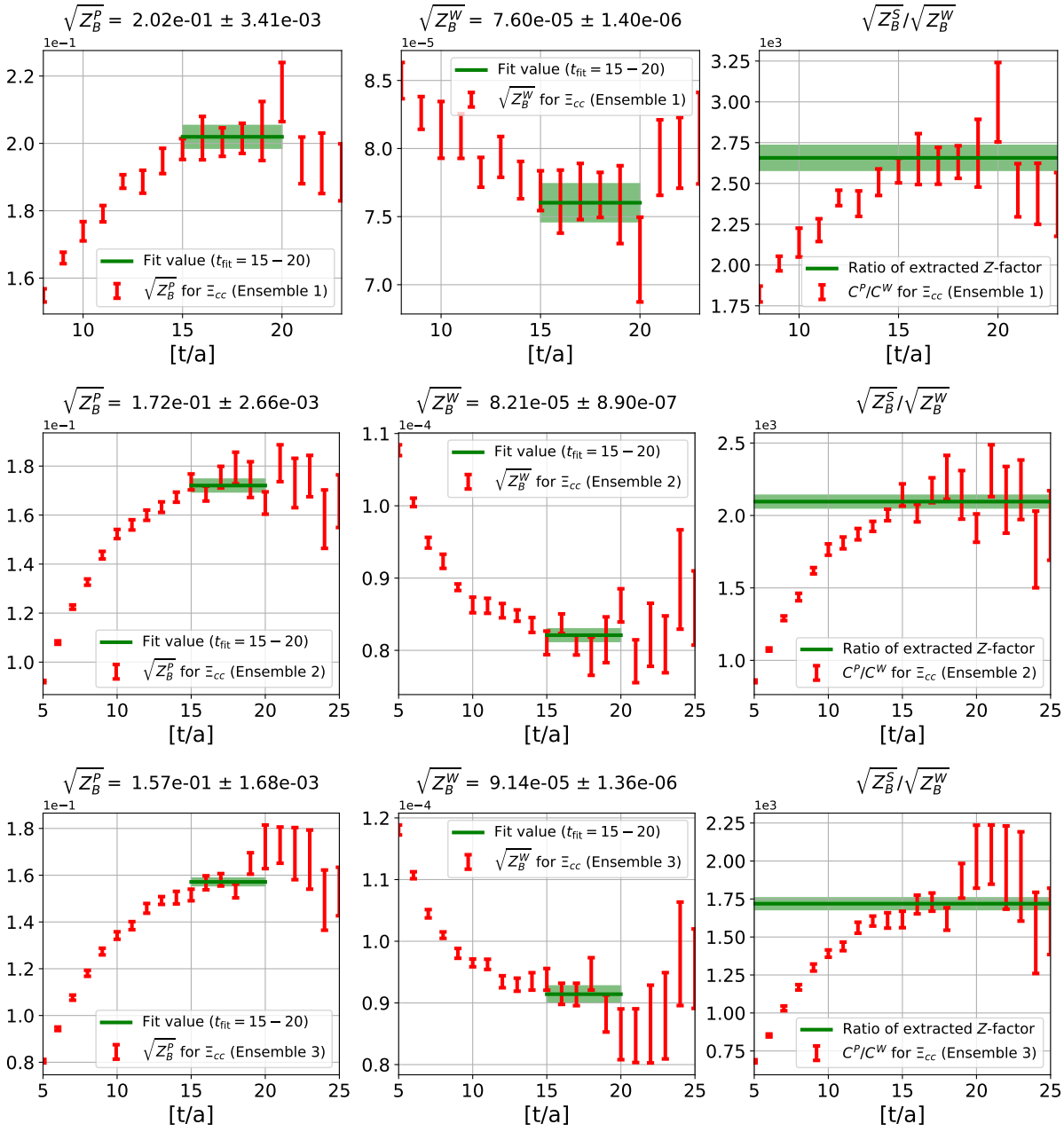

Figure C.4: The fitting results of the Z-factors for Ξ_{cc}. Upper three figures correspond to the results for the ensemble 1 ($m_\pi \simeq 700$ MeV case). Middle three figures correspond to the results for the ensemble 2 ($m_\pi \simeq 570$ MeV case). Lower three figures correspond to the results for the ensemble 3 ($m_\pi \simeq 410$ MeV case).

Bibliography

[1] R. Machleidt and I. Slaus, "*The Nucleon-nucleon interaction: Topical review*", *J. Phys. G* **27** (2001) R69 [arXiv:nucl-th/0101056].

[2] E. Hiyama, T. Motoba, T. A. Rijken and Y. Yamamoto, "*Baryon-baryon interactions and hypernuclei*", *Prog. Theor. Phys. Suppl.* **185** (2010) 1.

[3] C. B. Dover and S. H. Kahana, "*Possibility of Charmed Hypernuclei*", *Phys. Rev. Lett.* **39** (1977) 1506.

[4] C. B. Dover, S. H. Kahana, and T. L. Trueman, "*Bound states of charmed baryons and antibaryons*", *Phys. Rev. D* **16** (1977) 799.

[5] H. Bando and M. Bando, "$^{5}_{\Lambda_c}$*He and* $^{9}_{\Lambda_c}$*Be charmed nuclei versus* $^{5}_{\Lambda}$*He and* $^{9}_{\Lambda}$*Be hypernuclei*", *Phys. Lett. B* **109** (1982) 164.

[6] H. Bando and S. Nagata, "*Flavor Nuclei One Boson Exchange Potentials*", *Prog. Theor. Phys.* **69** (1983) 557.

[7] H. Bando, "*Chapter VII. Flavor Nuclei*", *Prog. Theor. Phys. Suppl.* **81** (1985) 197.

[8] Y. R. Liu and M. Oka, "$\Lambda_c N$ *bound states revisited*", *Phys. Rev. D* **85** (2012) 014015 [arXiv:1103.4624 [hep-ph]].

[9] A. Gal, H. Garcilazo, A. Valcarce, and T. F. Caramés, "*Pion-assisted charmed dibaryon candidate*", *Phys. Rev. D* **90** (2014) 014019, [arXiv:1405.5094 [nucl-th]].

[10] H. Garcilazo, A. Valcarce and T. F. Caramés, "$J = 3/2$ *charmed hypertriton*", *Phys. Rev. C* **92** (2015) 024006 [arXiv:1508.03535 [nucl-th]].

[11] S. Maeda, M. Oka, A. Yokota, E. Hiyama and Y. R. Liu, "*A model of charmed baryon-nucleon potential and two- and three-body bound states with charmed*

baryon", *Prog. Theor. Exp. Phys.* **2016** (2016) no.2, 023D02 [arXiv:1509.02445 [nucl-th]].

[12] K. Tsushima and F. C. Khanna, "Λ_c^+ *and* Λ_b *hypernuclei*", *Phys. Rev. C* **67** (2003) 015211 [arXiv:nucl-th/0207077].

[13] K. Tsushima and F. C. Khanna, "Λ_c^+, Σ_c, Ξ_c *and* Λ_b *hypernuclei in the quark-meson coupling model*", *J. Phys. G: Nucl. Part. Phys.* **30** (2004) 1765 [arXiv:nucl-th/0303073].

[14] H. Huang, J. Ping, and F. Wang, "$N\Sigma_c$ *and* $N\Sigma_b$ *resonances in the quark-delocalization color-screening model*", *Phys. Rev. C* **87** (2013) 034002.

[15] S. Dürr, *et al.*, "*Ab Initio Determination of Light Hadron Masses*", *Science* **322** (2008) 1224 [arXiv:0906.3599 [hep-lat]].

[16] PACS-CS Collaboration: S. Aoki, *et al.*, "$2+1$ *Flavor Lattice QCD toward the Physical Point*", *Phys. Rev. D* **79** (2009) 034503 [arXiv:0807.1661 [hep-lat]].

[17] Sz. Borsanyi, *et al.*, "*Ab initio calculation of the neutron-proton mass difference*", *Science* **347** (2015) 1452 [arXiv:1406.4088 [hep-lat]].

[18] Y. Namekawa, *et al.* (PACS-CS Collaboration), "*Charmed baryons at the physical point in* $2+1$ *flavor lattice QCD*", *Phys. Rev. D* **87** (2013) 094512 [arXiv:1301.4743 [hep-lat]].

[19] LHCb Collaboration, "*Observation of the doubly charmed baryon* Ξ_{cc}^{++}", *Phys. Rev. Lett.* **119** (2017) 112001.

[20] M. Lüscher, "*Two particle states on a torus and their relation to the scattering matrix*", *Nucl. Phys. B* **354** (1991) 531.

[21] N. Ishii, S. Aoki and T. Hatsuda, "*Nuclear Force from Lattice QCD*", *Phys. Rev. Lett.* **99** (2007) 022001 [nucl-th/0611096].

[22] T. Miyamoto for HAL QCD Collaboration, "$\Lambda_c - N$ *interaction from lattice QCD*", *PoS LATTICE* **2015** (2016) 090, [arXiv:1602.07797 [hep-lat]].

[23] T. Miyamoto, *et al.* [HAL QCD Collaboration], "$\Lambda_c N$ *interaction from lattice QCD and its application to* Λ_c *hypernuclei*", *Nucl. Phys. A* **971** (2018) 113, [arXiv:1710.05545 [hep-lat]].

[24] T. Miyamoto for HAL QCD Collaboration, "*The coupled channel approach to the* $\Lambda_c N - \Sigma_c N$ *system in lattice QCD*", *PoS LATTICE* **2016** (2017) 117.

[25] T. Miyamoto for HAL QCD Collaboration, "*Coupled-channel* $\Lambda_c N - \Sigma_c N$ *interaction from lattice QCD*", *PoS Hadron* **2017** (2018) 146.

[26] T. Miyamoto, *et al.*, In preparation.

[27] K. G. Wilson, "*Confinement of Quarks*", *Phys. Rev. D* **10** (1974) 2445.

[28] H. B. Nielsen and M. Ninomiya, "*Absence of Neutrinos on a Lattice. 1. Proof by Homotopy Theory*", *Nucl. Phys. B* **185** (1981) 20.

[29] K. Symanzik, "*in Mathematical Problems In Theoretical Physics*", eds. R. Schrader et al., Lecture Notes in Physics, Vol. 153, (Springer, New York 1982).

[30] K. Symanzik, "*Continuum Limit and Improved Action in Lattice Theories*", *Nucl. Phys. B* **226** (1983) 187.

[31] B. Sheikholeslami and R. Wohlert, "*Improved continuum limit lattice action for QCD with wilson fermions*", *Nucl. Phys. B* **259** (1985) 572.

[32] K. Jansen and R. Sommer, "*O(a) improvement of lattice QCD with two flavors of Wilson quarks*", *Nucl. Phys. B* **530** (1998) 185 [arXiv:hep-lat/9803017].

[33] Y. Iwasaki, preprint, UTHEP-118 (Dec. 1983), unpublished.

[34] S. Aoki *et al.* [JLQCD Collaboration], "*Non-trivial phase structure of* $N_f = 3$ *QCD with* $\mathcal{O}(a)$*-improved Wilson fermion at zero temperature*", *Nucl. Phys. Proc. Suppl.* **106** (2002) 263 [arXiv:hep-lat/0110088].

[35] S. Aoki *et al.* [JLQCD Collaboration], "*Bulk first-order phase transition in three-flavor lattice QCD with* $\mathcal{O}(a)$*-improved Wilson fermion action at zero temperature*", *Phys. Rev. D* **72** (2005) 054510 [arXiv:hep-lat/0409016].

[36] S. Aoki, Y. Kuramashi and S. Tominaga, "*Relativistic Heavy Quarks on the Lattice*", *Prog. Theor. Phys* **109** (2003) 383. [arXiv:hep-lat/0107009].

[37] Y. Kayaba, S. Aoki, M. Fukugita, Y. Iwasaki, K. Kanaya, Y. Kuramashi, M. Okawa, A. Ukawa and T. Yoshié, "*First nonperturbative test of a relativistic heavy quark action in quenched lattice QCD*", *JHEP* **0702** (2007) 019 [arXiv:hep-lat/0611033].

[38] S. Aoki, T. Hatsuda and N. Ishii, "*Nuclear Force from Monte Carlo Simulations of Lattice Quantum Chromodynamics*", *Comput. Sci. Dis.* **1** (2008) 015009 [arXiv:0805.2462 [hep-ph]].

[39] S. Aoki, T. Hatsuda and N. Ishii, "*Theoretical Foundation of the Nuclear Force in QCD and its applications to Central and Tensor Forces in Quenched Lattice QCD Simulations*", *Prog. Theor. Phys.* **123** (2010) 89 [arXiv:0909.5585 [hep-lat]].

[40] S. Aoki *et al.* [HAL QCD Collaboration], "*Lattice QCD approach to Nuclear Physics*", *Prog. Theor. Exp. Phys.* **2012** (2012) 01A105 [arXiv:1206.5088 [hep-lat]].

[41] J. Balog, M. Niedermaier, F. Niedermayer, A. Patrascioiu, E. Seiler and P. Weisz, "*Does the XY Model have an integrable continuum limit?*", *Nucl. Phys. B* **618** (2001) 315 [hep-lat/0106015].

[42] S. Aoki *et al.* [CP-PACS Collaboration], "$I = 2$ *pion scattering length from two-pion wave functions*", *Phys. Rev. D* **71** (2005) 094504 [hep-lat/0503025].

[43] S. Aoki, "*Lattice QCD and Nuclear Physics*", [arXiv:1008.4427 [hep-lat]].

[44] S. Aoki *et al.* [HAL QCD Collaboration], "*Extraction of Hadron Interactions above Inelastic Threshold in Lattice QCD*", *Proc. Japan Acad. B* **87** (2011) 509 [arXiv:1106.2281 [hep-lat]].

[45] S. Aoki, N. Ishii, T. Doi, Y. Ikeda and T. Inoue, "*Asymptotic behavior of Nambu-Bethe-Salpeter wave functions for multiparticles in quantum field theories*", *Phys. Rev. D* **88** (2013) 014036 [arXiv:1303.2210 [hep-lat]].

[46] S. Gongyo, S. Aoki, "*Asymptotic behavior of Nambu-Bethe-Salpeter wave functions for scalar systems with a bound state*", *Prog. Theor. Exp. Phys.* **2018** (2018) no.9, 093B03 [arXiv:1807.02967 [hep-lat]].

[47] S. Okubo and R. E. Marshak, "*Velocity dependence of the two-nucleon interaction*", *Ann. Phys.* **4** (1958) 166.

[48] K. Murano, N. Ishii, S. Aoki and T. Hatsuda, "*Nucleon-Nucleon Potential and its Non-locality in Lattice QCD*", *Prog. Theor. Phys.* **125** (2011) 1225 [arXiv:1103.0619 [hep-lat]].

[49] T. Iritani *et al.* [HAL QCD Collaboration], "*Mirage in Temporal Correlation functions for Baryon-Baryon Interactions in Lattice QCD*", *JHEP* **1610** (2016) 101 [arXiv:1607.06371 [hep-lat]].

[50] T. Iritani *et al.* [HAL QCD Collaboration], "*Are two nucleons bound in lattice QCD for heavy quark masses? Consistency check with Lüscher 's finite volume formula*", *Phys. Rev. D* **96** (2017) no.3, 034521 [arXiv:1703.07210 [hep-lat]].

[51] N. Ishii *et al.* [HAL QCD Collaboration], "*Hadron-Hadron Interactions from Imaginary-time Nambu-Bethe-Salpeter Wave Function on the Lattice*", *Phys. Lett. B* **712** (2012) 437 [arXiv:1203.3642 [hep-lat]].

[52] S. Aoki, B. Charron, T. Doi, T. Hatsuda, T. Inoue and N. Ishii, "*Construction of energy-independent potentials above inelastic thresholds in quantum field theories*", *Phys. Rev. D* **87** (2013) 034512 [arXiv:1212.4896 [hep-lat]].

[53] T. Inoue *et al.* [HAL QCD Collaboration], "*Baryon-Baryon Interactions in the Flavor SU(3) Limit from Full QCD Simulations on the Lattice*", *Prog. Theor. Phys.* **124** (2010) 591 [arXiv:1007.3559 [hep-lat]].

[54] Charles W. Misner, "*Spherical harmonic decomposition on a cubic grid*", *Class. Quant. Grav.* **21** (2004) S243-S248, [arXiv:gr-qc/9910044].

[55] Mark E. Rupright, "*Spherical Harmonic Amplitudes From Grid Data*", [arXiv:gr-qc/0606127].

[56] CP-PACS, JLQCD Collaborations: S. Aoki, *et al.*, "*Nonperturbative $\mathcal{O}(a)$ improvement of the Wilson quark action with the RG-improved gauge action using the Schrödinger functional method*", *Phys. Rev. D* **73** (2006) 034501 [arXiv:hep-lat/0508031].

[57] `http://www.jldg.org/ildg-data/index.html`.

[58] M. Bruno, J. Finkenrath, F. Knechtli, B. Leder, and R. Sommer (ALPHA Collaboration), "*On the effects of heavy sea quarks at low energies*", *Phys. Rev. Lett.* **114** (2015) 102001 [arXiv:1410.8374 [hep-lat]].

[59] F. Knechtli, A. Athenodorou, M. Bruno, J. Finkenrath, B. Leder, M. Marinkovic and R. Sommer, "*Physical and cut-off effects of heavy sea quarks*", *PoS LATTICE* **2014** (2014) 288 [arXiv:1411.1239 [hep-lat]].

[60] T. Doi and M. G. Endres, "*Unified contraction algorithm for multi-baryon correlators on the lattice*", *Comput. Phys. Commun.* **184** (2013) 117 [arXiv:1205.0585 [hep-lat]].

[61] M. Oka, K. Shimizu, and K. Yazaki, "*Hyperon - Nucleon and Hyperon-hyperon Interaction in a Quark Model*", *Nucl. Phys. A* **464** (1987) 700.

[62] M. Neubert, "*Heavy quark symmetry*", *Phys. Rept.* **245** (1994) 259, [arXiv:hep-ph/9306320].

[63] Y. Yamaguchi, S. Ohkoda, A. Hosaka, T. Hyodo and S. Yasui, "*Heavy quark symmetry in multihadron systems*", *Phys. Rev. D* **91** (2015) 034034 [arXiv:1402.5222 [hep-ph]].

[64] R. L. Jaffe, "*Perhaps a Stable Dihyperon*", *Phys. Rev. Lett.* **38** (1977) 195 [Erratum-ibid. **38** (1977) 617].

[65] K. Sasaki, *et al.* [HAL QCD Collaboration], "*Lattice QCD studies on baryon interactions in the strangeness -2 sector with physical quark masses*", *EPJ Web Conf.* **175** (2018) 05010.

[66] H. P. Stapp, T. J. Ypsilantis and N. Metropolis, "*Phase-Shift Analysis of 310-MeV Proton-Proton Scattering Experiments*", *Phys. Rev.* **105** (1957) 302.

[67] M. El-Azab Farid and M. A. Hassanain, "*Density-independent folding analysis of the ^{6,7}Li elastic scattering at intermediate energies*", *Nucl. Phys. A* **678** (2000) 39.

[68] E. Hiyama, Y. Kino and M. Kamimura, "*Gaussian expansion method for few-body systems*", *Prog. Part. Nucl. Phys.* **51** (2003) 223.

[69] H. De Vries, C. W. De Jager, and C. De Vries, "*NUCLEAR CHARGE-DENSITY-DISTRIBUTION PARAMETERS FROM ELASTIC ELECTRON SCATTERING*", *Atomic Data and Nuclear Data Tables* **36** (1987) 495.

[70] K.-I. Ishikawa, *et al.* [PACS Collaboration], "$2+1$ *flavor QCD simulation on a* 96^4 *lattice*", *PoS LATTICE* **2015** (2016) 075 [arXiv:1511.09222 [hep-lat]].

[71] T. Iritani, *et al.* [HAL QCD Collaboration], "$N\Omega$ *dibaryon from lattice QCD near the physical point*", [arXiv:1810.03416 [hep-lat]].

[72] S. Gongyo, *et al.* [HAL QCD Collaboration], "*Most Strange Dibaryon from Lattice QCD*", *Phys. Rev. Lett.* **120** (2018) no.21, 212001 [arXiv:1709.00654 [hep-lat]].

[73] H. Nemura, *et al.* [HAL QCD Collaboration], "Baryon interactions from lattice QCD with physical masses — strangeness $S = -1$ sector —," *EPJ Web Conf.* **175** (2018) 05030 [arXiv:1711.07003 [hep-lat]].

[74] K. Sasaki, *et al.* [HAL QCD Collaboration], "Lattice QCD studies on baryon interactions in the strangeness -2 sector with physical quark masses," *EPJ Web Conf.* **175** (2018) 05010.

[75] N. Ishii, *et al.* [HAL QCD Collaboration], "Baryon interactions from lattice QCD with physical masses — $S = -3$ sector: $\Xi\Sigma$ and $\Xi\Sigma$-$\Lambda\Sigma$ —," *EPJ Web Conf.* **175** (2018) 05013.

[76] `http://bridge.kek.jp/Lattice-code/`.